

UNIVERSITÀ DEGLI STUDI DI VERONA

DEPARTMENT OF

*Computer Sciences
(Diagnostic and Public Health)*

GRADUATE SCHOOL OF

Natural Sciences and Engineering

DOCTORAL PROGRAM IN

Nanoscience and Advanced Technologies

Cycle XXXIII

TITLE OF THE DOCTORAL THESIS

FROM THE VIBRATIONAL DYNAMICS OF GLASSES TO THE MELT VISCOSITY AND BACKWARD TO GLASSES

S.S.D. FIS/01

Coordinator: Prof. Adolfo Speghini

Signature _____

Tutor: Prof. Gino Mariotto

Signature 

Doctoral Student: Dott. Michele Cassetta

Signature 

CONTENTS

<i>Acknowledgements</i>	I
NOTATIONS	II
ABBREVIATIONS	IV
INTRODUCTION	1
1. GLASSY STATE	3
1.1. LIQUID AND SUPER-COOLED LIQUID	3
<i>Thermodynamic description of relaxation</i>	6
<i>Elastic description of relaxation</i>	8
1.2. GLASS DYNAMICS	12
<i>Glass structure</i>	12
<i>Vibrational dynamics of glasses</i>	14
<i>The Vibrational Density of States</i>	15
<i>The Debye Model</i>	15
<i>The Boson Peak</i>	17
<i>Models for the Boson Peak</i>	19
1.3. VISCOSITY	23
<i>Fragility</i>	23
<i>Overview of the main models</i>	25
<i>Viscosity measurement techniques</i>	28
1.4. VOLCANOLOGICAL IMPLICATIONS	30
<i>Importance of viscosity</i>	30
<i>Backward to glasses</i>	33
2. METHODS	35
2.1. RAMAN CLASSICAL THEORY	35
2.2. RAMAN SCATTERING IN GLASSES	38
<i>Breaking the selection rules</i>	38
<i>Raman density of states</i>	39
2.3. EXPERIMENTAL SETUP	43
<i>Raman</i>	43
<i>Brillouin</i>	46
3. SAMPLE SELECTION	48
3.1. MATERIALS	48
3.2. LITERATURE DATA	48
4. RESULTS	50
5. DISCUSSION	55
6. CONCLUSION	66

APPENDIX I: Effect of $\text{Fe}^{3+}/\text{Fe}_{(\text{tot})}$ in Pantelleritic glasses	67
<i>Starting materials</i>	68
<i>Results</i>	69
<i>Discussion and conclusions</i>	70
APPENDIX II: Effect of Na-K mixing in Basaltic glasses	74
<i>Glass synthesis</i>	75
<i>Glass transition measurements</i>	77
<i>Raman measurements</i>	78
<i>Results, discussion and conclusions</i>	78
APPENDIX III: The case of SiO_2 - Na_2O join	88
REFERENCES	94

to D. Braconi

“when the going gets weird, the weird turn pro”

H. S. Thompson

Acknowledgements

I am deeply grateful for all that concerns my professional growth to Dr. M. Zanatta, Dr. D. Di Genova, Dr. F. P. Vetere, Dr. M. Giarola, Dr. S. Nazzareni, Prof. N. Daldosso, Prof. H. Behrens, Prof. F. Holtz, Dr. M. Dietrich, Prof. G. Wörner, Prof. A. Kronz, Dr. M. Biesuz, Dr. B. Rossi, Prof. M. Bettinelli, Prof. A. Speghini, Prof. D. Perugini, Dr. D. Morgavi, Dr. M. Petrelli, Dr. A. Kumar, Dr. E. Chistè, Dr. C. Nardon, E. Viviani and Prof. M. Scarpa. Thanks to colleagues Dr. G. Marchioro, A. Sambugaro, Dr. S. Rossi and S. Mazzocato for the support. To Dr. L. Bastianelli for the artistic contribution. Special thanks go to my family and to my brotherly friends, while the lovely one goes to Dr. M. Galasso. Finally, I am more than grateful to my supervisor Prof. G. Mariotto, who gave me the opportunity to develop autonomously my doctoral project, especially for conveying to me the values of the independence.

NOTATIONS

SYMBOL	DEFINITION	UNIT
T	Temperature	K <i>or</i> °C
T_m	Melting temperature	K <i>or</i> °C
T_g	Glass transition temperature	K <i>or</i> °C
T_g^{peak}	Glass transition temperature peak	K <i>or</i> °C
T_f	Fictive temperature	K <i>or</i> °C
T_c	Crossover temperature	K <i>or</i> °C
T_K	Kauzmann's entropy crisis temperature	K <i>or</i> °C
T_0	Absolute zero	K <i>or</i> °C
T_D	Debye Temperature	K <i>or</i> °C
η_s	Shear viscosity	Pa s
q	Cooling rate	K s ⁻¹
c_p	Specific heat capacity	J K ⁻¹ kg ⁻¹
C_p	Heat capacity	J K ⁻¹
M	Longitudinal modulus	Pa
G	Shear modulus	Pa
K	Bulk modulus	Pa
G_∞	Shear modulus at infinite frequency	Pa
K_∞	Bulk modulus at infinite frequency	Pa
$\dot{\gamma}$	Elongational strain rate	s ⁻¹
u	Velocity	m s ⁻¹
g	Gravity	m s ⁻²
m	Fragility	dimensionless
E_a	Activation energy	J mol ⁻¹
E_η	Activation energy of the viscous flow	J mol ⁻¹
R	Gas constant	J mol ⁻¹ K ⁻¹
S	Entropy	J K ⁻¹
H	Enthalpy	J
U	Internal energy	J
V	Volume	m ³
k_B	Boltzmann constant	J K ⁻¹
h	Planck constant	J s
\hbar	Reduced Planck constant	J s

\vec{P}	Dipole moment	C m
$\vec{\alpha}$	Polarizability tensor	C m ² V ⁻¹
ε	Dielectric constant	C m ⁻¹ V ⁻¹
χ	Electric susceptibility	dimensionless
E	Electric field	V m ⁻¹
ν	Frequency	Hz
ω	Frequency shift	cm ⁻¹
ϖ	Angular frequency	rad s
Γ	Width	cm ⁻¹
ξ	Dynamical variable	relative
q_k	Displacement amplitude	kg ^{1/2} m
c	Speed of light	m s ⁻¹
I	Intensity	counts
λ	Wavelength	m
\vec{k}	Wavevector	m ⁻¹
\vec{q}	Phonon wavevector	m ⁻¹
v_L	Longitudinal sound velocity	m s ⁻¹
v_T	Transversal sound velocity	m s ⁻¹
ϕ	Tilting	°
θ	Scattering angle	°
v_D	Debye velocity	m s ⁻¹
ρ	Density	kg m ³
N_A	Avogadro number	mol ⁻¹
X	Molar fraction	relative
M	Molar weight	kg mol ⁻¹
ρ_n	Number density	m ⁻³
$R(\omega)$	Correlation length	m
$g(\omega)$	Density of states	J m ⁻³
u_i	Displacement vector	m
σ	Stress	Pa
n_c	Number of constraints	relative
χ	Composition	relative
τ_R	Structural relaxation time	s
t	Time	s

ABBREVIATIONS

- NF** – Network Former
NM – Network Modifier
BO – Bridging Oxygen
NBO – Non-Bridging Oxygen
A – Cation
T – Tetrahedra
MRO – Medium-Range Order
CCR – Cooperatively Rearrangement Regions
LRO – Long-Range Order
SCL – Super-Cooled Liquid
G – Glass
L – Liquid
C – Crystal
GFL – Glass Forming Liquid
VFT – Vogel-Fulcher-Tamman
AG – Adam-Gibbs
KWW – Kohlrausch-Williams-Watts
MYEGA – Mauro-Yue-Ellison-Gupta-Allan
CCD – Coupled Charge Device
NA – Numerical Aperture
HH – Horizontal Horizontal
HV – Horizontal Vertical
UV – Ultra Violet
DOS – Density Of States
VDOS – Vibrational Density Of States
BP – Boson Peak
HRM – Harmonic Random Matrix
ERM – Euclidean Random Matrix
SPM – Soft Potential Model
QLV – Quasi-Local Vibrations
TLS – Two-Level System
TCT – Topological Constraint Theory
BB – Bond Bending
BS – Bond Stretching
FWHM – Full-Width at Half Maximum

QES – Quasi-Elastic Scattering
RMSE – Root-Mean-Square-Error
BLS – Brillouin Light Scattering
RS – Raman Scattering
DSC – Differential Scanning Calorimetry
TEM – Transmission Electron Microscopy
XANES – X-ray Absorption Near Edge Structure
EXAFS – Extended X-ray Absorption Fine Structure
CBF – Continuous Basalt Fiber
EMPA – Electron Micro-Probe Analyzer

INTRODUCTION

The human-glass interaction has always existed^{1,2}. Therefore, there is not a deep knowledge on the mechanisms governing the transition from liquid to glass, representing a challenging task for both glass- and geoscience²⁻⁴. Indeed, magmas and industrial melts are the results of the Nature will and of the Human design respectively. Despite the strong difference regarding the nature of their complexities, they are investigated through the same methods and modelled by the same laws^{5,6}. In particular, viscosity represents a first order parameter in the micro- and macro-scale processes characterizing both melting or heat treatments of glass production-processing, and the magmatic behavior deeply hidden below an active volcano, directly impacting on its eruptive style⁷⁻¹⁶. However, recent studies are leading to the conclusion that viscous properties are strongly altered by the incursion of fast nano-scale modification, therefore our understanding of viscosity on volcanic melts remains elusive¹⁷⁻²¹.

This aspect will be treated in the first chapter, reviewing the main aspect of the theoretical description behind the liquid, supercooled liquid and glassy state. Following, the viscosity will be overviewed including a description of its models and measurements techniques toward a volcanological context, whilst some crucial concept of glasses will be concomitantly recalled.

The very central aspect here is that some of the melt properties are embedded in the vibrational properties of glass²²⁻²⁶.

This study deals with the vibrational dynamics of silicate glasses having different compositions and applications, extending up to complex multicomponent systems of volcanological interest. In particular, we examine the possibility of correlating the characteristic band of the low-frequency Raman spectrum of glasses namely the Boson Peak (BP, deepened in chapter 2), to a key-property of the glass-forming liquids, the fragility. Moreover, exploiting the cooperation with the Bavarian Geoinstitute of Bayreuth (Germany), where the Brillouin experiments were carried out, we demonstrate that the measurement of the sound wave propagating in glasses allows also to estimate the fragility and so derive the melt viscosity.

The viscosity determination of a melt requires complex protocols, combined techniques and suitable apparatus operating at very high temperatures resulting in costly

and time-consuming operations. Thus, the possibility of being able to directly estimate the viscosity bypassing the intrinsic complexity of the viscosity measurements, represents a mutual benefit for both geosciences and glass sciences and this is the thrust of this study. Here we propose an accurate crossed Brillouin-Raman spectroscopic strategy that allows an accurate estimation of volcanic melts viscosity at eruptive conditions, from the vibrational properties of their parental glasses. To concretely develop our model, we based our theoretical background on the MYEGA formalism (recently proposed by Mauro and co-workers⁷), in which the fragility is one of the key-parameter to estimate viscosity, and exploiting the correlation between fragility and both the elastic properties and the inverse amplitude of the BP of glasses proposed by Novikov and Sokolov²⁴. Part of the results are published in Cassetta et al.²⁷. Additionally, both new measurements and the extensive review of the literature data, suggests a direct link between the acoustic modes and BP. In particular, it emerges a direct relation between the ratio of the bulk and shear moduli and the BP position in frequency going beyond the Novikov's prediction²³. Thus, given the enduring debate about the BP phenomenon (see ref.²⁸), we take the opportunity to show new evidence which could be insightful for its theoretical description.

Last but not least, the enclosed appendixes support our main results representing other case-study of sectorial interests such as: peralkaline rhyolites named Pantellerite which is a low-viscous and silica-rich magmatic liquid and basalts for manufacture glasses and ceramics. Finally, we have collected and processed literature data of a simple binary system (sodium-silicate) to firstly test our conclusions and possibly provide an additional open topic on which to develop future investigations.

1. GLASSY STATE

Glass is a particular state of the matter having a solid-like behavior in a short time-scale. However, by changing the observation time-scale (for instance by moving from the human time-scale to a geological one) the glass flow away under the action of gravity and the structure is continuously driven toward an equilibrium state, culminating with the crystalline phase. Thus, glass is defined as *a nonequilibrium, non-crystalline state of matter that appears solid on a short time scale but continuously relaxes towards the liquid state and its ultimate fate is to crystallize* (see ref.²⁹ and literature therein).

1.1. LIQUID AND SUPER-COOLED LIQUID

In this section we provide a description of the glass transition adopting the relaxation point of view, which will be furtherly framed by the thermodynamic and elastic characterization.

The transition of a liquid to a solid-like state is a gradual and reversible transition that usually occur with the cooling of a liquid below its melting temperature (T_m). Above T_m , the liquid (L) is thermodynamically stable and is characterized by a very high atomic mobility as well as its high ability to flow. If the liquid is cooled slowly (in equilibrium), crystallization may take place through concatenated processes of nucleation and growth around T_m . However, if the cooling is particularly fast (out of equilibrium), the crystallization can be avoided and the liquid enters in a metastable state and is termed super-cooled liquid (SCL). Further cooling of the system, brings the liquid in the *glass transition interval*, which is the temperature interval separating the liquid from the glassy state. Lastly, the glass will tend irreversibly to an ideal equilibrium state by changing continuously its thermodynamic state with energy dissipation at infinite time. This is called relaxation process²⁹.

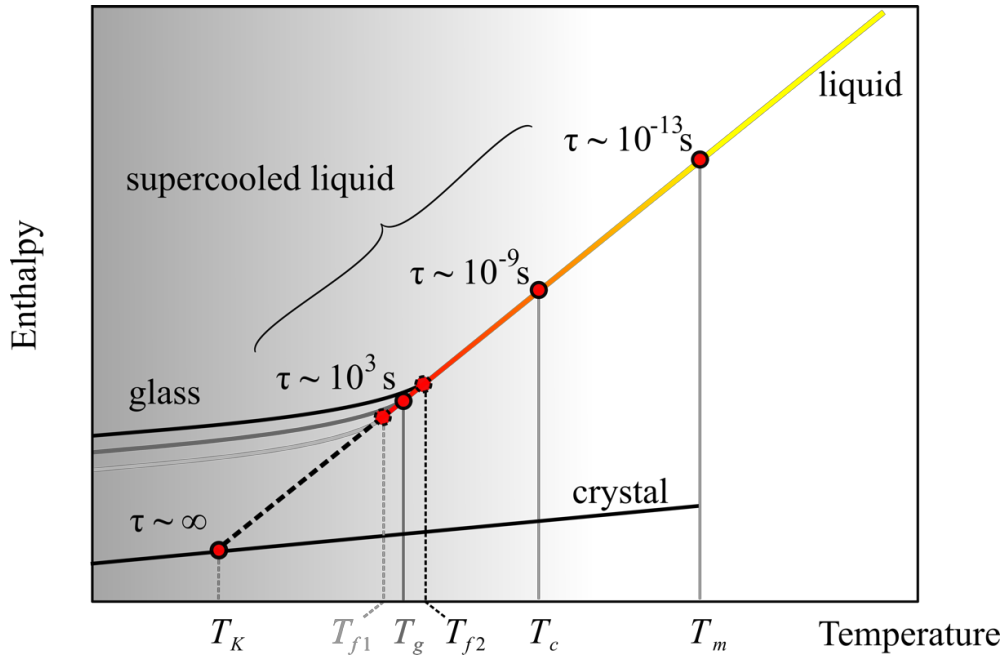


Figure 1.1 Schematic representation of the enthalpy as a function of temperature in a liquid, from the high-T phase, down to the deeply supercooled phase. All the relevant temperatures introduced in these notes are marked: T_m (the melting point), T_c (crossover temperature from a high-T nonactivated dynamics to a low-T activated one), T_f (fictive temperatures), T_g (glass transition temperature), T_K (is Kauzmann's entropy crisis temperature, where the extrapolated liquid entropy hits the crystal entropy, and where according to some theories there is a thermodynamic phase transition) and T_θ (the temperature where the Vogel–Fulcher–Tamman fit locates a divergence of the relaxation time). Above each temperature is reported the approximate value (in seconds) of the relaxation time (see ref.³⁰).

In Figure 1.1 is reported the phase-transition diagram which can be described as it follows:

- I. In equilibrium conditions, L only exists above liquidus temperature or T_m and it never crystallizes.
- II. SCL exists between T_m and the glass transition interval. It is metastable, i.e., a thermodynamic barrier must be overcome for crystal nucleation to take place at the so-called crossover temperature T_c , and it eventually crystallizes after a certain time;
- III. Glass (G) exists below the glass transition temperature, T_g . It is thermodynamically unstable and spontaneously relaxes toward the

supercooled liquid state at any non-zero temperature (dotted line in Figure 1). The glass transition takes place at T_g , $[\tau_R(T_g) = 10^2 - 10^3 \text{ s}]$ and $[\eta(T_g) = 10^{12} \text{ Pa s}]^{31}$. On the heating path, a glass changes to a SCL at T_g . At any positive temperature, above or below T_g , for sufficiently long times ($t_{\text{obs}} \gg \tau_R$), any SCL or glass (different gray tonality in Figure 1.) relaxes and then eventually crystallizes.

- IV. Crystal (C) is a true solid with a well-organized atomic structure at short, medium and long range, which is thermodynamically stable below T_m .

By lowering the temperature with a certain cooling rate q (K s^{-1}), the viscosity increases of many orders of magnitude, from a typical high temperature liquid value of about 10^{-4} Pa s to 10^{12} Pa s . Here the viscosity is too high to appreciate any atomic or molecular motion (except vibrations) in a typical t_{obs} and the material experiences a dramatic departure from equilibrium³². A further key to read the relaxation process is that going off-equilibrium, the system does not have enough time to explore the phase-space (a space in which all possible states of a system are represented, with each possible state corresponding to one unique point in the phase space) and in these conditions the system is unable to find new configurations causing a drop of the thermodynamic equilibrium and the system is named non-ergodic. Thus, a dynamic system can be described by the nonergodicity factor, which is defined as the long time limit of the density-density correlator and increases from zero in the liquid to a finite positive value when the system enters into the glassy state and atoms are frozen into a disordered liquid-like structure^{30,33}.

Thus, the configuration of the SCL is frozen in the glassy state and the temperature at which this transition takes place, in function of q , is defined as fictive temperature T_f . Here, the glass is perfectly nonergodic (or “isostructural”), and the viscosity is described well by an Arrhenius behavior.

A fundamental aspect in describing the system, with particular focus on relaxation, involves the link between viscosity and entropy. This is also crucial in the thermochemical and thermomechanical modelling of the melt viscosity that will be deepens in section 1.3.

The well-known Arrhenius law expressed as: $\log \eta (T) = \log \eta_{\infty} + (E_a/RT)$, where E_a , is the activation energy, R the gas constant and η_{∞} is the viscosity at infinite temperature; provides the basis on which most of the viscosity-predictive models were built^{34,35}. However many evidence³⁶⁻³⁸ highlighted strong deviations of the Arrhenius law-based models in describing the viscosity of melts over the whole temperature interval.

In 1984 Richet³⁸ proposed a solid way to describe the relaxation of silicate melts, introducing the configurational entropy S^{conf} as control-parameter for the dynamic of the system describing viscosity. By moving from T_m to the absolute zero temperature, S^{conf} can be written in function of both T and T_f as:

$$S^{conf}(T, T_f) = S_{vit}(0) + \int_{T_f}^T \frac{C_{p,SCL}(T) - C_{p,vit}(T_f)}{T} dT \quad (1.1)$$

$$S_{vit}(0) = \Delta S_m + \int_0^{T_m} \frac{C_{p,c}(T)}{T} dT + \int_{T_m}^{T_f} \frac{C_{p,l}(T)}{T} dT + \int_{T_f}^0 \frac{C_{p,vit}(T)}{T} dT \quad (1.2)$$

Here S_{vit} and ΔS_m are the vitreous and the fusion of the crystal entropies whilst $C_{p,c}$, $C_{p,l}$, $C_{p,SCL}$ and $C_{p,vit}$ are the heat capacities of the crystalline, liquid, SCL and glassy phases. In this case the quantity S_{vit} is the crucial parameter since represent the frozen in configuration entropy of the glass at $S^{conf}(T_f)$, in particular it determines the size of cooperatively rearrangement regions (CRR). However, the vibrational contribution of the glass must be removed assuming $\Delta C_p = C_{p,l} - C_{p,vit}$ as the configurational heat capacity of the liquid (C_p^{conf}) and S^{conf} in function of temperature reads:

$$S^{conf}(T) = S^{conf}(T_f) + \int_{T_f}^T \frac{\Delta C_p(T)}{T} dT \quad (1.3)$$

Thus, through the relaxation theory of the Adam-Gibbs (AG) model³⁹ the silicate melts viscosity can be estimated as:

$$\log \eta (T) = \log \eta_{\infty} + \frac{B}{T S^{conf}(T)} \quad (1.1)$$

here B has constant value and is related to the free energy barrier per molecule in CRR. At very high temperatures, viscosity displays an Arrhenius-type dependence on temperature in the form of $\ln \eta \propto E_{\eta}/T$ where E_{η} represents the activation energy of the viscous flow. However, anomalies arise when the $\tau_R \rightarrow \infty$ and the SCL's $T_f \rightarrow 0$ (namely ideal glass transition, when the entropy or enthalpy lines of the crystal and that of the liquid intercept, see Figure 1.1). Here, the excess entropy defined as $S_{ex} = S_{SCL} - S_c$ would be zero, but extrapolating $S_{ex}(T) = 0$ it is found to exist at $T > 0$ K thus, violating the third law of thermodynamic. This behavior is called Kauzmann's paradox⁴⁰, and the temperature at which the so-called entropy crisis takes place is termed Kauzmann's temperature (T_K) and corresponds to $S^{conf}(T) = 0$ in the Adam-Gibbs theory. Here, the prediction of a second-order transition tentatively describes the relaxation at τ_{∞} , by introducing⁴¹ T_2 which is the temperature at which S^{conf} would vanish, thus $S^{conf}(T) = \Delta C_p \ln(T/T_2)$ is commonly integrated in the theoretical description of relaxation in the AG-based models^{38,42}. However, an ideal second order transition being experimentally unobservable, makes the model unsuitable for practical purpose. The absence of known in this temperature interval has been bridged by the landscape energy analysis proposed by Stillinger^{43,44}, in which the liquid entropy smoothly converge to zero avoiding the problem of the entropy crisis. Even though the Kauzmann's paradox remains an emblematic pending issue in condensed matter physics⁴⁵, some theoretical^{29,46} and experimental^{45,47} study highlight an ideal temperature at which the glass finally crystallizes (T_{KS}) and found to be $T_{KS} > T_K$ ⁴⁸.

The response of a given material to a mechanical perturbation of its equilibrium (stress σ), is to equilibrate the system with a specific relaxation timescale according to the Hooke's law, and its viscoelastic description reads:

$$\frac{\varepsilon(t)}{\sigma} = \left(\frac{1}{M} + \frac{t}{\eta} \right) \quad (1.5)$$

Here M is the longitudinal or Young modulus ($M = K + 4G/3$) where K and G are the bulk and shear moduli, η the Newtonian viscosity and $\varepsilon(t)$ is the strain in function of time (t).

Deformations are time-dependent thus, the equilibrium of the material can be also perturbed with different timescale by sinusoidal stress $\sigma(\varpi)$ with a frequency $\varpi = 2\pi f$. Dingwell, in 1989⁴⁹ showed that silicate melts, have their own behavior in function of the strain rate with a $\tau_R = (2\pi f)^{-1}$. Thus, they react with a viscous response if $\log \varpi \tau_R \ll 1$ and with an elastic one if $\log \varpi \tau_R \gg 1$ to the applied stress. Then, through the Maxwell⁵⁰ relation $\eta = G_\infty \tau_R$, is possible to unravel the viscoelastic response of a melt, by using an appropriate timescale. As a matter of fact, by probing a liquid with a $\varpi > \tau_R$, its behavior is completely unrelaxed and if liquid viscosity is known at a certain temperature $\eta(T)$, G_∞ (as well as K_∞) can be measured and they are named clamped properties⁵¹. In these particular conditions the liquid does not have enough time to flow, having a solid-like behavior while its elastic moduli are defined as "instantaneous". They can be related quite generally to frequency-dependent viscosity coefficients by⁵²:

$$K_\varpi = K + i\varpi \eta_K(\varpi) \quad (1.6)$$

$$G_\varpi = i\varpi \eta_G(\varpi) \quad (1.7)$$

where, η_G , η_K are coefficients of shear and bulk viscosities, respectively. At zero frequency, the shear modulus vanishes for liquids, while the bulk modulus does not. At

very high frequency ($\omega \rightarrow \infty$), $\lim_{\omega \rightarrow \infty} G(\omega) = G_\infty$, even the liquids become solid like and $G_\infty > 0$.

In ref.⁴⁹ has been calculated several τ_R curves in function of temperature, in which $\eta(T)$ is known for a wide range of silicate melts and considering $\log G_\infty = 10 \pm 0.5$ (i.e. $3.2 < G_\infty < 32$ GPa).

The high-frequency limits of the elastic moduli (instantaneous elastic constants) are determined by the high-frequency limits of the viscosity coefficients. The barrier transition for a “flow event” or a molecular rearrangement occur on a very short time scale, so the height of the energy barrier could be determined by liquid properties which can be probed on this time scale. During freezing or vitrification (polymerization) of glass-forming liquids, the clamped moduli behave in a strongly nonlinear fashion as temperature decreases and the energy barrier broadens and becomes more and more suppressed.

The first kinetic theories for viscous flow in liquids are based on the assumption of homogeneous flow⁵³, in which the shear modulus is vanishing. However, as for any theory (soon or later) has been refuted by assuming a non-vanishing shear modulus as the fluid has a comparable atomic packing density of a solid⁵¹. Considering the case of a monoatomic liquid is possible to define the moduli K_∞ and G_∞ as:

$$G_\infty = \rho_n k_B T + \frac{2\pi\rho_n^2}{15} \int_0^\infty \frac{d}{dr} \left[r^4 \frac{dU}{dr} \right] g(r) dr \quad (1.8)$$

$$K_\infty = \frac{5}{3} G - \frac{4\pi\rho_n^2}{12} \int_0^\infty [r^3 U(r)] g(r) dr \quad (1.9)$$

Where ρ_n is the number density, $U(r)$ is the potential energy of the interaction pair potential (function that describes the potential energy of two interacting objects), $g(r)$ is the pair distribution function having interatomic spacing r , and k_B is the Boltzmann constant.

Moving from high temperatures to the glass transition interval, the infinite frequency response of the equilibrium liquid changes through the phase transition. Thus, at a given fictive temperature (T_f), the elastic constants of the glass and those of the liquid,

will have the same value. Conversely, at any $\varpi\tau_R \sim 1$ (where viscous and elastic behavior coexist), corresponds a glass transition T_f , at any temperature in function of τ_R Figure 1.2.

Assuming K and G similar to $G_\infty(T_f)$ and $K_\infty(T_f)$, we can observe a decreasing trend of the ratio K/G as T_f decreases, thus revealing a peculiar behavior for (at least) each class of glass.

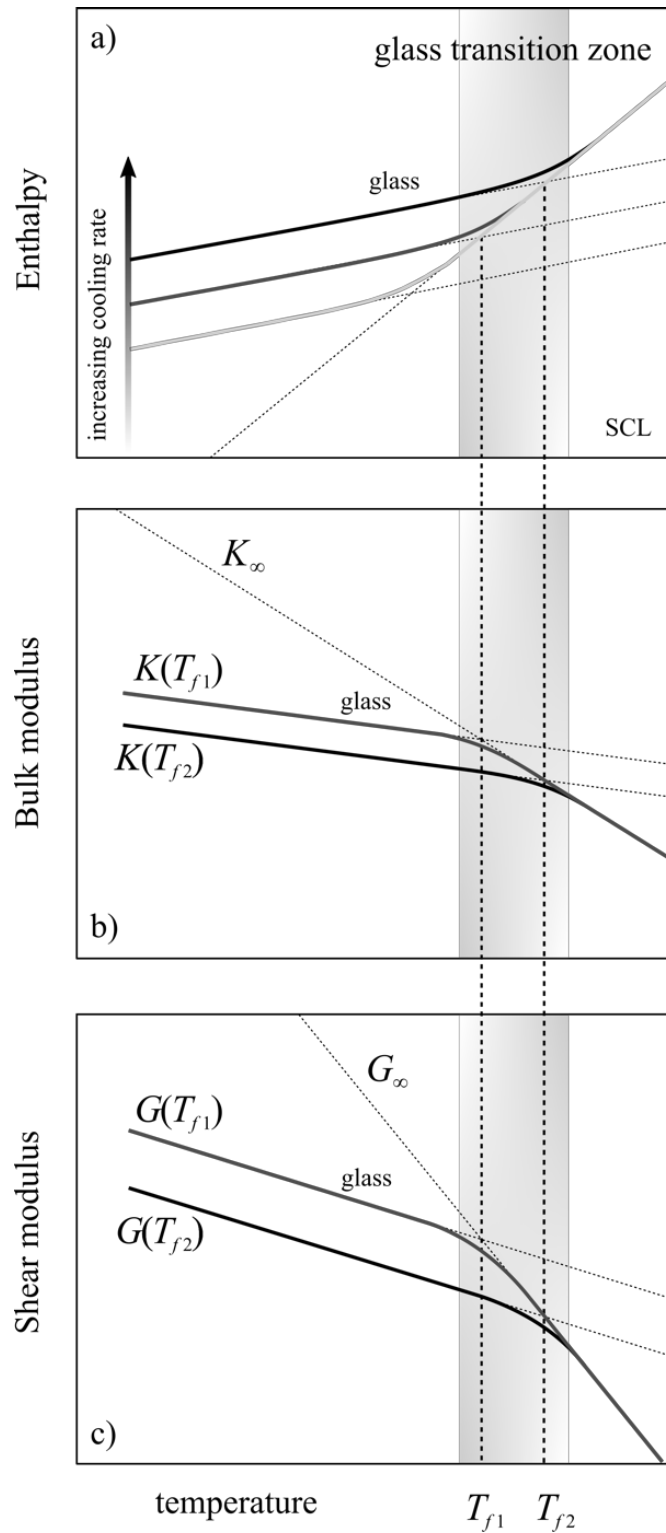


Figure 1.2 Typical behavior of the elastic constants (G and K) throughout the glass transition: a) The relative change of K ; b) the relative change of the G . The reference value is K or G and room temperature. The infinite frequency bulk and shear moduli of the liquid become frozen at T_f .

1.2. GLASS DYNAMICS

In this section glass will be described firstly, according to its structure and its role in glass relaxation. Secondly, a vibrational dynamic background will be also provided focusing on the link between the microscopic vibrations and macroscopic properties of glasses (i.e. sound propagation, heat transfer and the other thermodynamic entities in solids).

Glass structure

The first definition of glass structure has been postulated in the pioneering work of Zachariasen in 1932³ where was observed a lack in long range order (LRO), periodic atomic structure and any translational symmetry. Thus, glasses exhibit only a limited short-range order, and unlike crystal (shaped by lattice with infinite periodicity, see Figure 1.3 a) and b)), remain completely random in the long-range scale⁵⁴. Based on these observations, he infers that the glass lattice can be assimilated to a unique molecule or to a system of a unique giant elementary cell, giving origin to the random-network theory. In the case of a silicate oxide glasses, the structure consists on cations tetrahedrally coordinated (T) and surrounded by a certain number of oxygens. By shearing their corners through the bridging oxygen (BO) they form the network-structure of randomly oriented units according to the following rules:

- I. The number of oxygens surrounding the cation T must be small.
- II. No oxygen is bonded to more than two cations T.
- III. The tetrahedra can have only common summits (neither edges nor faces)
- IV. At least three summits of each tetrahedron must be put in common with other tetrahedra.

The firsts 3 rules describes if the glass is flexible enough to form a random network, whilst the rule 4 describes if the connectivity is high enough to allow a continuous network which is rigid enough to avoid crystallization. In turn, flexibility and rigidity are closely linked to composition, in particular to the ratio between tetrahedrally coordinated atoms namely network former (NF) and the non-bridging oxygen (NBO) which is an

oxygen connecting a T to a non-tetrahedral polyhedron. Thus, the ratio NBO/T represent the polymerization degree and increases with the non-tetrahedral cations in the network namely network modifier (NM).

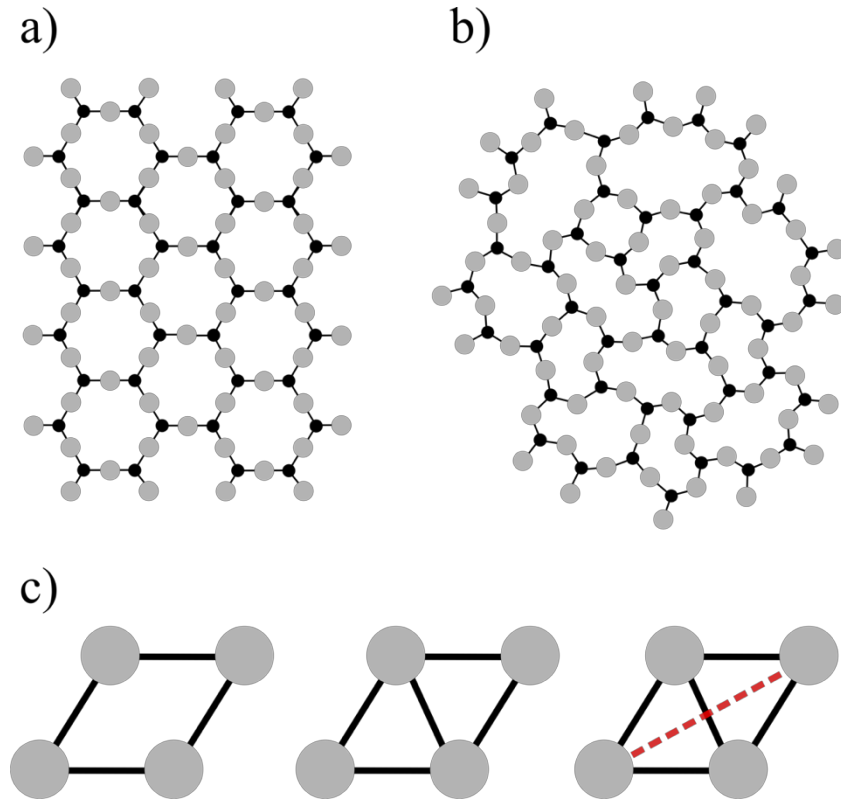


Figure 1.3 Bi-dimensional sketch of the structure of both crystalline α -quartz (a) and vitreous SiO_2 (b). Grey dots are oxygen atoms while black dots refer to silicon ones. Redrawn after Zachariasen 1932³. The three states of rigidity of a mechanical truss (c) from left: flexible, isostatic and stressed rigid trusses. The dashed red line represents a redundant constraint that is here under tension.

An efficient theoretical tool linking the microscopic physics governing composition and the atomic structure to macroscopic properties (i.e. thermal, mechanical and rheological) is the topological constraint theory (TCT)^{55,56}. Here, the glass networks are represented by mechanical trusses, which can be stressed rigid or flexible in function of the ratio between the number of atomic degrees of freedom (3 in the 3-D network) and the number of chemical constraints (n_c). Thus, if $n_c < 3$, then the network is considered “flexible”. In this case the glass is deformed without external energy input and exhibit floppy modes (*modes that can propagate with little energy cost*)⁵⁷, whilst the atoms easily

reorganize toward lower energy states and fostering crystallization. Conversely, if the number of constraints is greater than the available degrees of freedom ($n_c > 3$), the network becomes “over-constrained” or “stressed rigid”, the excess constraints are termed redundant Figure 1.3 c). In this case, the sum of the yields of the weakest constraints is higher than that of the strongest ones. Thus, the glass network is locally unstable and continuously relax toward lower energy states (driven by internal stress) providing suitable thermodynamic conditions for crystallization. Accordingly, a glass without floppy modes and internal stress is defined isostatic and represent the most stable thermodynamic and dynamic form of glass with a given composition in terms of relaxation and crystallization.

TCT has been successful in predicting the composition dependence of glass properties providing a solid theoretical tool to quantitatively characterize and design new glass compositions for a given application^{58,59}.

Vibrational dynamics of glasses

Atoms in solids vibrates around their equilibrium positions from the absolute zero, as a result of zero-point motion, to very high temperature, as a result of thermal fluctuations.

The vibrations in crystals occur in a periodic and ordered medium thus, vibrational modes in nominally plane waves (called phonons), are described by the wave vectors \vec{q} defined as $\vec{q} = 2\pi/\lambda$, (for visible light $\lambda = 400\text{-}700$ nm we have a corresponding \vec{q} ranging in 10^4\AA^{-1}). This restriction strongly limits the interaction of visible light with vibrations having the wavevector lying near the center of the first Brillouin zone. In glasses the periodicity is completely lost and the additionally absence of reciprocity excludes \vec{q} as a proper quantum parameter to label the modes of glasses.

At low frequency, as $\vec{q} \rightarrow 0$, the vibrational excitations propagate linearly in form of acoustic waves of speeds v_L and v_T . Conversely, increasing ω acoustic phonon-like are detectable only with λ proportional to the interparticle distance.

However, increasing \vec{q} the excitation wavelength become shorter and the local structure dominates. In this case sound waves transform into a complex pattern of atomic motions that mirrors the structural disorder. Thus, the phonon dispersion cannot be properly characterized by the $\omega(q)$ curve⁶⁰.

The Vibrational Density of States

The vibrational density of states (VDOS) is largely used in solid state physics in describing the vibrational properties of general and represents a more suitable quantity in describing those of glasses. In particular, it represents the alternative to the $\omega(q)$ representing the distribution of the number of vibrational modes in function of frequency:

$$g(\omega) = \sum_k \delta(\omega - \omega_k) \quad (1.10)$$

Where $g(\omega)d\omega$ is the density of states (DOS) and is defined as the number of normal modes between ω and $\omega + d\omega$. Additionally, once known $g(\omega)$ is possible to retrieve the isochoric heat capacity and thermal conductivity.

As a matter of fact, the macroscopic properties of solids are intrinsically described by VDOS in a microscopic length-scale.

The Debye Model

The model roots on the concept that thermally excited modes (at low temperature) have a wavelength greater than the interparticle distance and, mostly, have energies comparable with the acoustic excitations. Thus, solids can be described as an elastic continuum in which the acoustic waves propagate.

In particular, it treats all three branches of the vibrational spectrum, nominally $k = (k_x, k_y, k_z)$ with the same linear dispersion relation $\omega = v_D k$.

The Debye velocity v_D results from the average of the longitudinal and transverse sound velocity v_L and v_T respectively as it follows:

$$\frac{3}{v_D^3} = \left(\frac{1}{v_L^3} + \frac{2}{v_T^3} \right) \quad (1.11)$$

and if the wave vectors of the normal modes are assumed to lie within a sphere of radius k_D rather than the first Brillouin zone, then the density of states can be written as:

$$\begin{aligned} g(\omega) &= 3 \int_{k < k_D} \frac{dk}{(2\pi)^3} \delta(\omega - v_D k) \\ &= \frac{3}{2\pi^2} \int_0^{k_D} k^2 dk \delta(\omega - v_D k) \\ &= \begin{cases} \frac{3}{2\pi^2} \frac{\omega^2}{v_D^3}, & \omega < \omega_D = v_D k_D \\ 0, & \omega > \omega_D \end{cases} \end{aligned} \quad (1.12)$$

Here ω_D is the Debye frequency and constrain on the VDOS a limiting frequency for the acoustic waves and below this value for an elastic isotropic medium, the density of states increases quadratically with frequency⁶¹.

The total number of vibrational modes in the Debye model is $3N$, with N the number of atoms in the system. Thus, the Debye frequency is defined as $\omega_D^3 = (6\pi^2 \rho N_A X_A / M) v_D^3$ (M is the average molar weight, N_A the Avogadro number, ρ the density and X_A the total atom fraction). Here the product $\rho N_A X_A / M$ can be also represented by the more suitable parameter termed number density (ρ_n), which can be used to define the Debye wave-vector as: $k_D = (2\pi^2 \rho_n)^{1/3}$.

Thus, the Debye frequency reads:

$$\omega_D = k_D v_D \quad (1.13)$$

Debye's law gives the density of states in the crystals, which can be used to calculate the specific heat c_p and the thermal conductivity. The Debye model for an elastic continuum predicts that the low-temperature heat capacity has a cubic temperature dependence, $C \propto T^3$ which is a consequence of the quadratic frequency dependence of VDOS.

$$c_p = \frac{12\pi^4}{5} N_A k_B \left(\frac{T}{T_D} \right)^3 \quad (1.14)$$

Here T_D is the Debye temperature and is defined as $T_D = \hbar\omega_D/k_B$ and represents the necessary temperature to excite all the acoustic modes. In this frame, for $T < T_D$ all the crystalline and glassy thermodynamic properties should be the same, which is not the real case.

The Boson Peak

The Debye model for an elastic medium, claims that the VDOS is a quadratic function of frequency $g(\omega) \propto \omega^2$ and the associated vibrational excitations are acoustic phonons. The Debye law span over a range of few THz for crystals. In the case of glasses can be observed a strong deviation of the prediction. In Figure 1.4 is depicted the typical frequency range of few terahertz, in which the ratio between the density of states and the Debye law shows the emergences of the peak termed "boson peak" (BP).

The first observation of the BP dates from 1942 by R. Berman⁶² when he was measuring the thermal conductivity of vitreous SiO₂.

He observed that the glass heat capacity (C) exceeds the crystalline one deviating from the Debye prediction of an averagely linear ΔT and then showing a plateau of the

thermal conductivity at about ~ 10 K with a magnitude of several orders smaller than that of crystals.

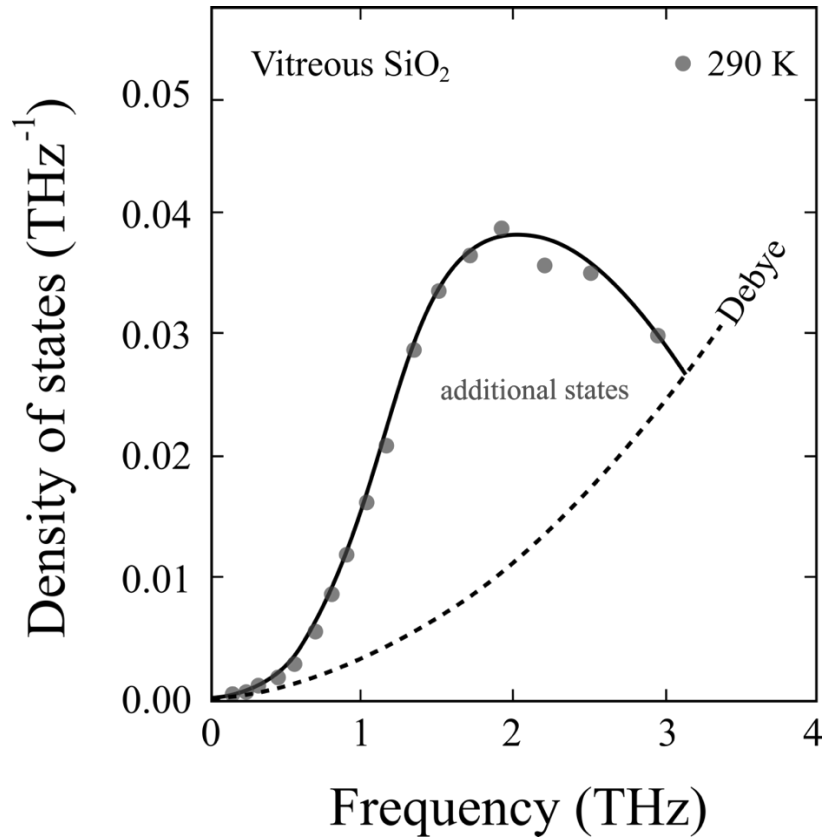


Figure 1.4 Density of states of additional modes in vitreous silica at ambient temperature, compared to the ones predicted by the Debye law. Readapted after Dianoux et al.⁶³.

This plateau if plotted in the C/T^3 becomes a bump mirroring an excess of modes in the vibrational density of states, even crystals do, but it is usually related to the transverse acoustic vibrational excitations near the boundary of the first Brillouin zone, originating harmonic phenomenon⁶⁴.

Sokolov and coworkers observed that the ratio between the specific heat and the Debye expectation at the temperature of the BP maximum, correlates well with the fragility of the glass, with a higher value for stronger glasses⁶⁵ because of the direct relationship between specific heat and $g(\omega)$ ⁶⁶, retrieving an inverse correlation between the amplitude of the BP (over the Debye level) and the fragility of the glass-forming

liquid. Recently, it has been overviewed²⁸ that the number of vibrational states is not strongly correlated with the glass fragility, which is instead probably correlated with the Debye level, at least for the systems considered in ref.⁶⁵.

Assuming the $\omega(q)$ as the necessary range addressed by the experimental scattering techniques to probe the DOS, Raman scattering (RS), inelastic neutron scattering (INS) and inelastic X-ray scattering (IXS) provide the correct conditions of measurements. There are also non-scattering techniques like infra-red (IR) spectroscopy which give information on the vibrational density of states in a q region related to the incoming radiation. Of particular interest here is that the acoustic linear dispersion curves merge with the low frequency optic vibrations in the Ioffe–Regel crossover region (defined as the energy region where the mean free path of the phonons approaches their wavelength)⁶⁷ and is located at around 1 THz, in which is the BP arises. This explains why the low-frequency part of the VDOS of disordered materials is largely investigated concomitantly to the study of the acoustic excitations. There is some evidence that the total number of vibrational modes at low frequencies, below the BP region, is not markedly different in different glasses. There is, on the contrary, a stronger variation in the BP position which can range from 1 to 10 meV⁶⁸ (10 meV = 80.65 cm⁻¹ = 2.42 THz). However, at present there is no clear microscopic explanation of the value of ω_{BP} , we only know that it is typically higher in systems with a higher value of the elastic modulus and there is some indication that the local structure plays a role^{69,70}.

Models for the Boson Peak

The nature of BP is still highly debated, however it is largely accepted as universal signature of intrinsic disorder in amorphous material. In this section will be treated the different point of view in explaining the nature and the origin of the BP⁶⁰.

- I. *Dynamical disorder*: A first class of models that describes the boson peak is based on the presence of dynamical disorder in the glass. In the model proposed by Taraskin and co-worker atoms occupy crystalline sites and the system is described as formed by coupled harmonic oscillators interacting

through random independent elastic force constants whose strength fluctuates according a probability distribution⁷¹. On increasing the width of the distribution, the system becomes unstable, thus with negative force constants, and this instability gives rise to the excess of modes in the vibrational density of state. Wider is the distribution, stronger the BP will be. In this approach the excess in the reduced VDOS is associated with the lowest van Hove singularity in the spectrum of the reference crystalline system, although the disorder causes its broadening and a downwards shift in energy. The vibrational modes originating the lowest van Hove singularity in the crystals are also those responsible for the boson-peak in the corresponding glass. In general, they seem to be related to transverse branches. A more recent model proposed by Schirmacher and co-workers^{64,72-74} is based on a macroscopic tensorial elastic and lattice-independent approach. The model assumption is that the disorder leads to microscopic random spatial fluctuations of the transverse elastic constant (shear modulus) whose variance is proportional to a disordered parameter g . The DOS excess arises from a band of disorder induced irregular vibrational states, the onset of which approaches lower frequencies as the disorder is increased. The model predicts also a strict correlation between the excess in the vibrational density of states and the sound damping of the acoustic waves present in the corresponding energy range.

- II. *Euclidean random matrix*: Euclidean Random Matrix models should not be included in the HRM class, even if they are developed in the harmonic approximation. As a matter of fact, the model deals directly with a topological disordered solid. The Euclidean random matrix provides a theoretical framework to treat the problem of the topological disorder, where the interactions cannot be split in an ordered part plus a disorder dependent contribution⁷⁵. This model supports the idea that the boson peak marks the transition between acoustic like excitations and a disorder dominated regime for the vibrational spectrum.

III. *Soft potential model:* The Soft Potential Model (SPM) assumes the existence of additional quasi-local vibrations (QLV) that interact with the sound waves, giving rise to the boson peak^{76–78}. This model can be considered as an extension at higher temperature of the two level system model (TLS), describing the thermal anomalies of glasses below 1 K. QLV are additional non acoustic modes characterized by a large vibrational amplitude of some group of atoms. The physical origin of these modes can be traced to local irregularities of the amorphous structure, or to low-lying optical modes in parental crystals. The disorder destroys the long-range coherence of these optical modes so they are indistinguishable from quasi-local modes. The vibrational density of states of QLV's cannot be arbitrary, depending only on the particulars of the glass. QLV's can be described as low frequency harmonic oscillators which weakly couple to the sound waves of the elastic continuum medium. This coupling leads to a dipole-dipole interaction between different harmonic oscillators. The interaction between harmonic oscillators give rise to a $g(\omega)$ which is a universal function at low frequency⁷⁸. This universality derives from the vibrational instability of the spectrum due to the interacting harmonic oscillators. For $\omega_c < \omega_D$, anharmonicity stabilizes the system in a new minimum thus it reconstructs the VDOS in a new spectrum. As a final result $g(\omega)/\omega^2$ shows a maximum without a peak in the density of states. In the SPM, the boson peak energy depends on the interaction strength among the different HO's. The stronger the interaction, the higher is the energy of the boson peak maximum. The weak coupling between QLV's and acoustic modes and the continuum medium avoids any influence of the localized modes on the acoustic properties of the system. In this way the model is able to explain both boson peak and acoustic features. Moreover, a recent work pointed out a direct link between boson peak and two-level systems: the raising of a peak in the reduced vibrational density of states seems to inevitably lead to the creation of two-level systems and vice versa⁷⁷.

-
- IV. *Inhomogeneous cohesion*: Another approach consists on ascribing the BP to the inhomogeneous cohesion of glasses at the nanometric scale⁷⁹. In this case the system is assumed to consist of an aggregate of "regions" with different elastic constants. The material is characterized by more cohesive domains separated by softer interdomain zones on the nanometric spatial range. The boson peak arises from vibrational modes spatially localized in such regions. In particular, the excess of modes in the VDOS is viewed as the signature of the hybridization of acoustic modes with localized ones, inherent to the elastic heterogeneities. The heterogeneous elastic response at the nano-scale can possibly be related to the existence of dynamical heterogeneities observed in supercooled liquids above the glass transition zone⁸⁰. Cohesion heterogeneities in glasses would originate from the mobility heterogeneities in the supercooled state conserved during the glass transition. Spatially correlated dynamics of the molecules in the melt is somehow "frozen in" at the glass transition, and leads to the creation of softer and harder zones in the glassy phase. Conversely the existence of elastic inhomogeneities in the mesoscopic spatial range does not imply automatically the existence of visible static density inhomogeneities. As a matter of fact, elasticity fluctuation can correspond to a negligible density fluctuation⁷⁹.
- V. *Spatially correlated modes*: The boson peak has been suggested to reflect a crossover from long wavelength vibrations propagating in the continuous media to localized vibrations on a characteristic length scale of $R \sim 10 \text{ \AA}$. This length has been interpreted as the correlation length for the disordered structure of the system^{81,82}. The energy of the peak result to be inversely proportional to the size of these spatial correlated regions, $\omega_{BP} \sim 1/R$. This correlation length $R(\omega)$ has been connected to the medium range order (MRO) extension as obtained considering the width or the position of the first sharp diffraction peak of the glass⁸¹.

1.3. VISCOSITY

Viscosity is the measure of the resistance to deformation of a liquid at a given rate. In this section we provide a description of the key-concepts fulfilling this work. Starting with fragility and what it represents we briefly overview the main models historically adopted to describe viscosity. Finally, we contextualize the role of viscosity in the volcanological context and its role in influencing the melt toward the glass transition, as well as the final product of the last melt fraction quenched during eruptions, backward to glasses.

Fragility

For practical applications the fragility plot of glass forming liquids (GFL)⁸³, roots on two intersection point:

- I. At $T_g/T \rightarrow 1$, $\log \eta (T_g) = 12$, $\log \tau_R (T_g) = 3$
- II. At $T_g/T \rightarrow 0$, $\log \eta_\infty \sim -4$ (or -2.93 in ref.⁸⁴), $\log \tau_\alpha \sim \log \tau_0 \sim -14$.

Thus, the rate of viscosity-change with temperature near T_g namely fragility index or “steepness index” (m), is quantified as it follows:

$$m = \left. \frac{\partial \log_{10} \eta}{\partial T_g/T} \right|_{T=T_g} \quad (1.15)$$

Thus, different GFLs can be classified according to their fragility. In particular “strong” or “fragile” melts are respectively classified by a quasi-/purely- or a non-Arrhenius dependence in the so-called Angell plot^{83,85,86}, as shown in Figure 1.5. Moreover, the fragility parameter m can be related to the microscopic interactions driving the dynamics of the system²². Strong liquids are characterized by covalent directional bonds and they typically form three-dimensional network structures. Emblematic example of this class of materials is SiO_2 , (with m between 20 and 25)^{87,88} that exhibits

slow decrease of the viscosity or structural relaxation time τ_R with T_g/T . On the contrary, fragile liquids show a steeper temperature dependence near T_g and typically consist of molecules interacting through non-directional, non-covalent bonding and with larger anharmonicity⁸⁹. The typical fragile glass-former is the aromatic hydrocarbon o-terphenyl (OTP), $m = 81$ ⁸⁷.

A different approach of data interpretation was also suggested by Nemilov⁹⁰ in 1964. It is based on the entropy of activation of viscous flow near glass transition, which essentially reflects the same property of viscosity. One important technical limit in determining m is the access to the high temperature regimes. This is also reported in Figure 1.3 in as much experiments are rarely performed below $T_g/T = 0.2$, which corresponds to inaccessible high temperatures in most cases.

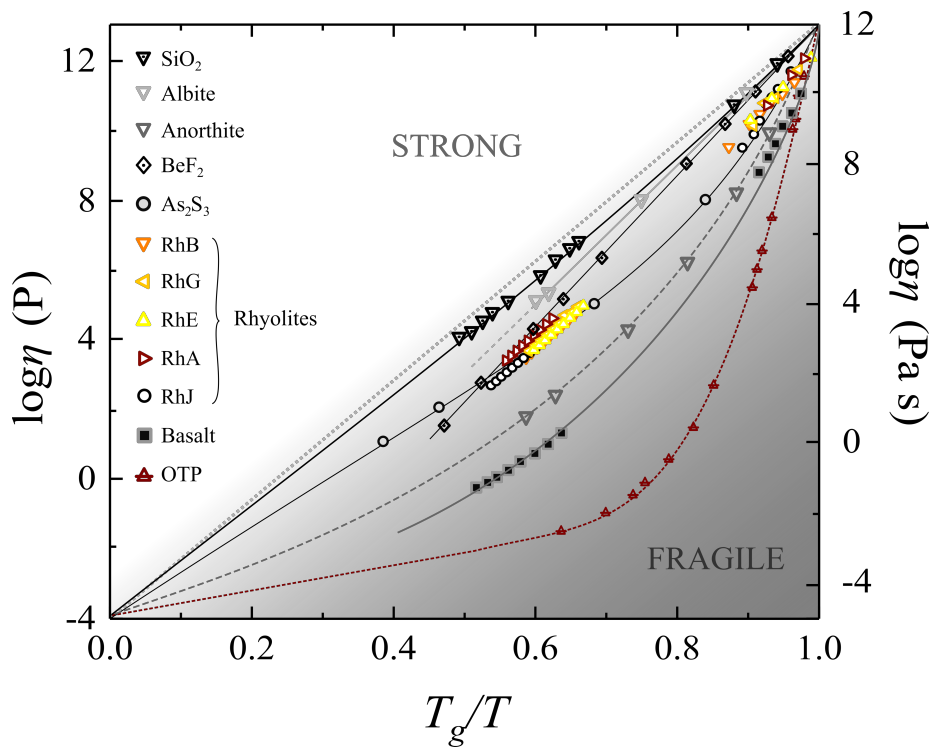


Figure 1.5 Angell's plot (log viscosity versus reduced temperature T_g/T) for different glass-forming systems including rhyolites group which is also object of this study (viscosity data from Di Genova et al.⁹¹), SiO_2 , albite, anorthite, BeF_2 , As_2O_3 and OTP data are after Angell^{32,92}. Basalt data are from Yue⁹³. The dotted grey line represent the fragility limit which is 17 according to the Novikov's prediction²³ and 14.97 to the Zheng's one⁹⁴. (Redrawn by M. Cassetta 2020).

This section deals with the derivations of the models describing viscosity and a brief overview of their prevision efficiency will be also shown.

In order to describe and comparing the differences among the models, is taken $\tau_R \propto \eta$ and defined (through $\tau_R = \tau$): $\tau_g = \tau(T_g)$; $\tau_0 = \tau(T \rightarrow \infty)$ and $y = T_g/T$. Then τ is written as:

$$\ln \tau = \ln \tau_0 + (\ln \tau_g - \ln \tau_0) f(y) \quad (1.16)$$

Here the $f(y)$ represent the type of function that fulfill each individual model⁶. In Table 1.1 are summarized the four models.

model	$f(y)$	a	$\pm \delta \log \eta^\dagger$	$\pm \delta T^\ddagger$
VFT (Vogel-Fulcher-Tamman) ⁹⁵⁻⁹⁷	$\frac{(1 - a_{VFT})y}{1 - a_{VFT}y}$	$a_{VFT} = T_0/T_g$	0.016	3
AG (Adam-Gibbs) ⁹⁸	$\frac{y}{1 - a_{AG} \ln y}$	$a_{AG} = C_p^{conf}/S_{vit}$	0.016	3
KWW (Avramov-Milchev) ⁹⁹	$y^{a_{KWW}}$	$a_{KWW} = 1.2 + 6X_{MOD}$	0.082	11
MYEGA (Mauro-Yue-Ellison-Gupta-Allan) ⁸⁴	$y \exp[a_{MYEGA}(y - 1)]$	$a_{MYEGA} = a_{AG}$	0.029	6

S_{vit} is the entropy of vitrification which is linked to the melting entropy S_m as $S_{vit}/S_m \approx 1 + (C_p^{conf}/S_m) \ln(T_g/T_m)$, X_{MOD} is the molar fraction of the network-modifiers, \dagger is the η standard deviation [Pa s], \ddagger is the T mean error [K].

Table 1.1 Brief resume of the main viscosity models from 1921 to 2009. The errors refer to the viscosity of standard float glass DGG-1 as measured by the National Metrology Institute (PTB) of Germany (46 data points between $538 < T_g < 1400$ °C) were fitted by a least square fit to the four models. Data from Musgraves et al. 2019⁶ and literature therein.

The VFT-type model is the one most widely used in glass technology. It is expressed in the form of $\log \eta = A + B/(T - C)$ where the three empirical parameters A , B

and C are deduced from a free volume model approach with a free volume $V_0(T)$ proportional to $T - C$, thus $C = T_0$ as in ref.¹⁰⁰. This often induce an overestimation of viscosity below T_g mainly due to the divergence of $\log \eta$ at $T = C$ representing the main weakness of the model. However, for $T > T_g$ it yields a highly accurate representation of viscosity in function of temperature.

It has been a matter of discussion whether or not the high- T limit in (1.16) and hence, the high temperature intercept $\log \eta_\infty$ is a universal feature of liquids. In fact, the numerical fits of experimental data by above models yield systematically different intercepts $\log \eta_\infty$ with the KWW (Kohlrausch-Williams-Watts) model typically giving the highest value while the VFT model gives the lowest one. The models also differ with respect to the slopes (i.e., the activation energies of viscous flow E_η) at which they approach the limit $T_g/T \rightarrow 0$. For both AG and KWW models, $E_\eta \rightarrow E_{\eta,\infty} = 0$ (as for a gas-like fluid), while either VFT or MYEGA models keep a finite value of $E_{\eta,\infty} > 0$. On the other hand, approaching the limit $T_g/T \rightarrow 1$, both KWW and VFT exhibit systematic errors while MYEGA, increases the efficiency of the low T viscosity description, giving a better fit⁸⁴.

The equation, presented by Mauro, Yue, Ellison ,Gupta and Allan⁸⁴ in 2009, is based on the AG model and S^{conf} is defined conformingly to the TCT⁵⁵ $S^{conf} = f(T,\chi) N_a k_B \ln \Omega$, where k_B is the Boltzmann's constant, Ω is the number of degenerate configurations per floppy mode and χ the composition. $f(T,\chi)$ is defined as controlling parameter for the enthalpy difference $H(\chi)$ for coexistent broken-intact network constraint and it is exponential. Unlike the AG model, the T_0 in $f(0,\chi) = 0$, means absence of thermal energy to break the bonds and the network is completely rigid. Thus, the three parameters equation is:

$$\log \eta (T,\chi) = \log \eta_\infty (\chi) + \frac{K(\chi)}{T} \exp \left(\frac{C(\chi)}{T} \right) \quad (1.17)$$

Where $K(\chi) = B(\chi)/(3N_a k_B \ln \Omega)$, and $C(\chi) = H(\chi)/k_B$ (here $B(\chi)$ has the same meaning of that in (1.4)).

The transformation in terms of physically meaningful quantities, namely T_g , m and η_∞ , the equation (1.17) reads:

$$\log \eta_s(T) = \log \eta_\infty + (12 - \log \eta_\infty) \frac{T_g}{T} \exp \left[\left(\frac{m}{12 - \log \eta_\infty} - 1 \right) \left(\frac{T_g}{T} - 1 \right) \right] \quad (1.18)$$

To summarize:

- I. VFT continues to be a fine model for the temperature range above T_g . However, it provides an $S^{conf}(T_0) = 0$ where $T_0 = T_K$.
- II. Both AG and MYEGA models provide the chances to get one fit constant by the quantity C_p^{conf}/S_{vit} as derived by independent thermodynamic experiments. Thus, once T_g is known, only the high- T intercept $\log \eta_\infty$ remains as the fit constant. The AG provides an $S^{conf}(T_0) = T_2$ which is a finite value of T .
- III. MYEGA model provides the possibility for a quantitative treatment of relaxation processes well-below T_g .

In the light of the above discussions, it emerges that an appropriate selection of these models enables a precise control of annealing and cooling processes, of thermal and chemical strengthening, a precise adjustment of refractive indices of optical glasses, and an approach to the properties of hyper-quenched glasses like reinforcement fibers and finally, allowing thorough implications concerning the rheological evolution of melts of magmatic origin.

This section sums up the different methods used to measure the viscosity in different reference points, defining the different viscosity-temperature range. In Table 1.2 are reported the different viscosity measurement techniques for different viscosity ranges, according to ref.¹⁰¹.

Range	Method	Viscosity range (Pa s)
Melting	Falling spheres or bubble rise	$< 10^5$
	Concentric cylinder	$< 10^5$
Softening and annealing	Parallel plate	$10^5 < \eta < 10^9$
	Micropenetration	$10^5 < \eta < 10^9$
	Fiber elongation	$10^5 < \eta < 10^{15.5}$
	Beam bending	$10^7 < \eta < 10^{13}$
	DSC	$10^{10} < \eta < 10^{12}$

Table 1.2 Summary of viscosity measurements techniques for different viscosity range.

Concentric cylinder viscosimetry and falling sphere technique operate from the melting to the working point and are central to measure the low viscosities of anhydrous (i.e. volatile-free) and volatile-bearing (mainly H₂O, CO₂ and S) melts at eruptive temperatures (from ~ 800 °C for rhyolites to ~ 1200 °C for basalts). However, concentric cylinder viscosimetry requires large quantities of material (~ 100 g) and can only measure the anhydrous viscosity because it operates at ambient pressure, whereas falling-sphere measurements of volatile-bearing samples are experimentally challenging, time consuming and require expensive high-pressure and high-temperature equipment. In contrast, micropenetration and parallel plate measurements, which operate from the softening point to the annealing point ($\eta = 10^{12.2}$) at ambient pressure and require a few mg of doubly polished glass with a thickness of ideally ~ 3 mm, are routinely applied to measure the high viscosities of volatile-free and -bearing melts. These measurements are carried around and slightly above the T_g where crystallization or volatile exsolution is

substantially prevented since the stress can be retrieved in few minutes. However, SCL may undergoes micro- and nano-crystallization or phase separation, which may occur within minutes or seconds¹⁷⁻²¹. An alternative experimental approach to estimate the viscosity of anhydrous and hydrous melts is based on differential scanning calorimetry (DSC) measurements (ref.¹⁰² and references therein). In this measurements, the relaxed liquid is first cooled into the SCL region at 10 K min⁻¹ and the following DSC heating scan is performed at the same rate. With the adoption of this protocol, the onset of the glass transition corresponds to T_g (see ref.^{20,102} and references therein). This procedure excludes the need to measure the viscosity to obtain T_g . This method effectively minimizes or even avoids the impact of melt heat treatment and requires small (~ 10 mg) quantities of material. However, DSC-derived viscosities are limited to viscosity intervals around T_g ²⁷. Fiber elongation and the beam bending are cost-effective methods too, give access to ranges up to 10¹³ or 10^{15.5} Pa s, covering a wider range of viscosity data which is crucial to understand the relaxation process in non-equilibrium condition and in the glassy state¹⁰¹.

1.4. VOLCANOLOGICAL IMPLICATIONS

Importance of viscosity

Volcanism and its associated magmatic processes provide a remarkably wide range of conditions for the behavior of silicate melts thus, investigations on rheology and mechanical properties of melts and magmas (melts plus crystals plus bubbles), are ubiquitous in deciphering the stresses and strains driving the eruptive behavior of volcanoes. Indeed, the study of these mechanisms is central for the assessment of natural hazards and the risk mitigation^{103,104}.

The reciprocal interaction between the intrinsic properties of the melt phase and external environment processes, determines the ascent of magmas to surface^{105,106}, see Figure 1.6. In particular shallowest process, may dramatically alter the stress field over the magmatic system (i.e. dome collapse, earthquakes, ice melting or land-slides Figure 1.6). The shallow processes (10 km) may influence the ascending magma for instance through crystallization, nano-crystallization and bubble growth, affecting permeability, rheology extent of outgassing and fragmentation depth thus, the magmatic thermo-mechanics in the plumbing system. As a matter of fact, recent studies^{17–21,107} report evidence of micro- and nanoscale modifications (i.e. crystallization and/or phase separation). In particular, nucleation of iron bearing nano-crystals is responsible for a significant viscosity increases trough complex interactions (i.e. chemical modification of the melt, formation of high-viscosity shells around crystals, and crystalline aggregates that increases the solid fraction in the melt)^{15,17,19}. Additionally, it is worth noting that these processes may occur within minutes when glasses are heated above their T_g in the SCL region, or even within seconds when melts experience undercooling and/or fast cooling rate¹⁵.

Processes that root from the lower crust up to and beyond the mid crust (lower than 10 km) continuously alter the intrinsic magmatic properties or parameters (temperature, rheology, volatile solubility, magmatic overpressure, dissolved and exsolved gas content, bubble and crystal content, and magma ascent rate) through process acting from storage

to ascent (i.e. magma crystallization and differentiation, mixing/mingling, crustal assimilation acting at different length-scale Figure 1.6). Again, the shear viscosity affects microscale processes such as the kinetics of nucleation and growth of crystals and gas phases concurring both in the dynamic of magmatic transport as well as their separation from the carrying liquid phase^{108–110}. Last but not least, evidences of small changes in composition χ in specific chemical domains can affect η_s of several orders of magnitude^{111–117}.

Macroscopically, the flow of volcanic melts and their viscoelastic response to deformation are dominantly controlled by the shear viscosity η_s ^{49,50}.

The interaction and timescale of these processes ultimately impact the magma ascent pathway, thus concurring in determining the dynamics, fate and style of volcanic eruptions. For instance, the mechanism behind the acceleration of a magma in a conduit associated (associated to a large elongational strain of magma), may be Figured out as a fiber of viscous melt, undergoing to an increasing strain rate. After the onset of a pseudo-plastic behaviour, the fiber breaks when its viscous flow is unable to compensate the accumulation of stress, at least until T_g . Following the Maxwell relation, the magma breakage criterion has been proposed by Papale et al.¹¹⁸, as:

$$\dot{\gamma} = k \frac{G_\infty}{\eta_s} \quad (1.2)$$

Where $\dot{\gamma}$ is the elongational strain rate, $k = 0.01$ is a constant, η_s is the shear viscosity and G_∞ is the shear modulus at infinite frequency. At slow strain rates, magma generally behaves as a liquid¹¹⁹ Figure 1.6 a). Thus, faster the strain rates (i.e., high decompression rates) the higher the probability of brittle fragmentation as it passes the glass transition for a given viscosity. Consequently, accurate knowledge of η_s is pivotal to simulate expected eruptive scenarios at a given volcano and assess the associated risks¹²⁰.

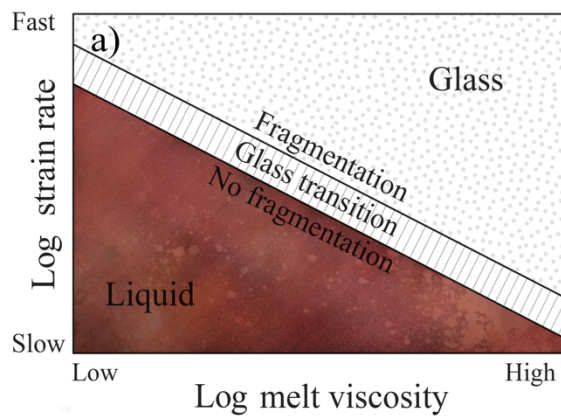
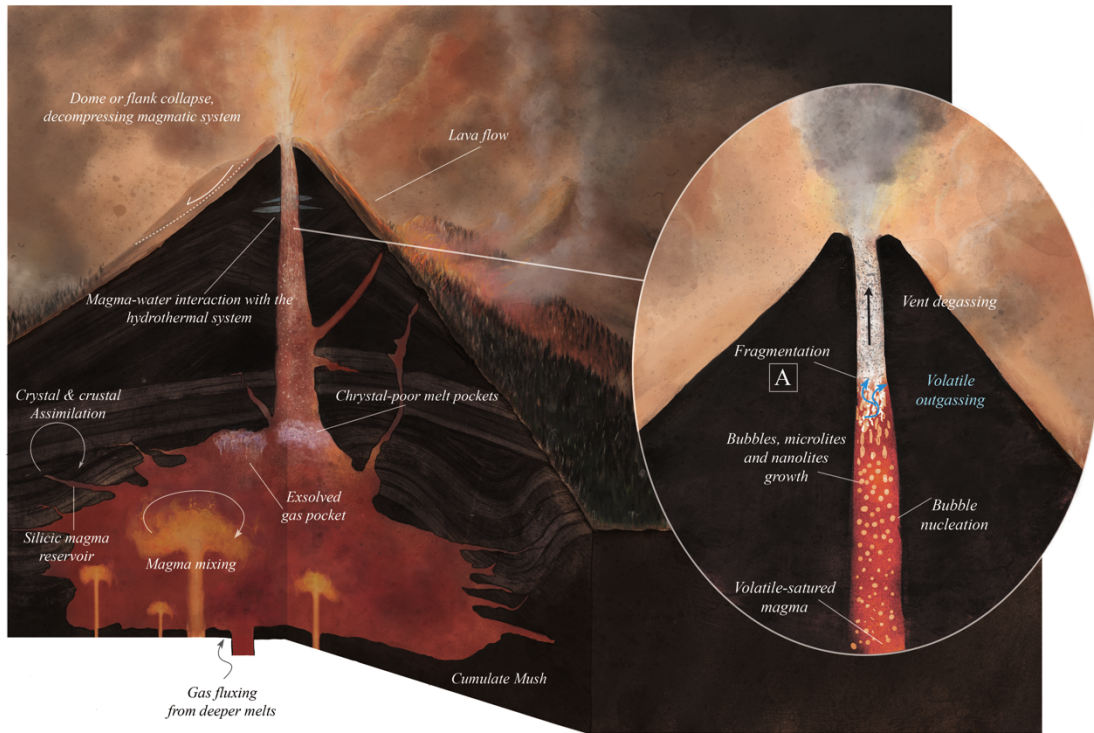


Figure 1.6 Artistic illustration of a schematic volcano depicting the different processes that can drive the eruptive style, from the magmatic chamber to the surface as discussed in the text. a) Shows how melt viscosity and strain rate control the fragmentation during the glass transition. Figure readapted and drawn by Luca Bastianelli after Cassidy et al.¹⁰⁵.

The last melt fraction, quenched and vitrified perhaps after the eruption, probably shows a very similar composition and structure of its parental melt^{121,122}. Nevertheless, the glass structure can be probed to retrieve fundamental information regarding the melt properties. This seems counterintuitive because glass properties should depend by the cooling rate.

However, the observations made by Scopigno et al.²² point out that vibrational properties of glass (well below T_g), correlate with m . In particular, they observed a correlation between the melt fragility and temperature behavior of the nonergodicity factor obtained through inelastic X-ray scattering experiments. The only possible decorrelation is given by the vibrations, which become progressively suppressed upon further temperature reduction and the nonergodicity factor increases. The parameter that controls this temperature behavior is proportional to m , thus suggesting that the melt fragility m is embedded in the vibrational properties of the resulting glass. Then, Novikov and Sokolov²⁴ explored the relationship between m and instantaneous bulk (K_∞) and shear (G_∞) elastic moduli of various non-metallic glasses. The elastic moduli were obtained from the longitudinal (v_L) and transvers (v_T) sound velocities measured by Brillouin light scattering (BLS) and the results showed a linear correlation between K_∞/G_∞ and m . However, the correlation fails if extended to a larger data-set of glasses (i.e. metallic, polymeric, chalcogenide and organic systems) resulting in a not-universal law²⁵. It has been proposed that the free-electron contribution to the bulk modulus of metals and a specific intramolecular contribution to the fragility in the case of polymers for some long molecules are the main reasons for the failure of the correlation²⁶. Furthermore, Novikov and Sokolov²⁴ showed that m linearly correlates with the inverse amplitude of the boson peak (BP). Experimentally, has been found a direct relation between the BP position and m in a $B_2O_3 - PbO$ system and were found to be connected to their common origin in the MRO structures¹²³.

These captivating observations suggest that the vibrational properties of glasses can be potentially exploited to derive $m(\chi)$ allowing the parameterization of melt viscosity at any temperature bypassing the challenging viscosity measurements^{122,124,125}. As a

matter of fact, volcanic glass can be part of the rock matrix or micrometric inclusions in minerals, in which direct liquid viscosity measurements is impossible. Here, we exploit the hypotheses in ref.^{22,24} by exploring a compositional domain of dry and hydrous glasses encompassing virtually the whole magmatism on Earth. We subjected these glasses to Brillouin and Raman spectroscopy and the results show that the fragility m correlates with both the K/G determined by BLS and boson peak position obtained by RS. The results from our study demonstrate that the viscosity of volcanic melts at eruptive temperatures can be accurately predicted from the spectroscopic analysis of glass. The proposed approach was carefully validated using external samples from the literature for which the viscosity is known and Brillouin and Raman data are available. This opens a new scenario for modelling the chemical contribution to the viscosity of glass-forming melts on a physically substantiated basis using their parental glasses.

2. METHODS

In this chapter we will briefly recall the basic principles of Raman scattering by the classical model overviewing the Raman scattering phenomenon in glasses. This last part is treated with particular focus on the low-frequency region and how the BP is reconciled to the VODS. Finally, will be provided a description of the instruments and the measurement conditions used in this work-thesis: Raman, carried out at UniVr and Brilluoin provided by BGI.

2.1. RAMAN CLASSICAL THEORY

When a molecule is within an electrical field \vec{E} , a dipole moment \vec{P} will be induced by the electric field through the relation: $\vec{P} = \vec{\alpha} \vec{E}$ where $\vec{\alpha}$ is the polarizability tensor. Without considering any supplementary excitation in the scattered volume, the polarizability of a molecule is the molecule response to the incoming electro-magnetic wave. If we consider a diatomic molecule, the induced electric dipole moment by an incoming electrical field E can be written as:

$$P = \epsilon_0 \chi E \quad (2.1)$$

where ϵ_0 is the vacuum dielectric constant, χ indicates the electric *response of the molecule to stimulus* E . E is the electrical field at a given time t and is represented by:

$$E = E_0 \cos(\omega_0 t) \quad (2.2)$$

In this case E_0 is the amplitude and ω_0 the frequency of radiation (laser beam). Here, $\nu = c/\lambda$ where c is the speed of light and λ the waveleght. Thus, the molecule emits an

electromagnetic radiation of frequency ν_0 , which is nothing other than the origin of Rayleigh scattering.

Further molecular excitations in the scattering volume, however, may modulate the electric susceptibility and then the induced polarization, which can be ascribed to the fluctuations of dynamical variables, ξ . Indeed, they induce vibrational displacement for phonons, magnetization for spin waves and spin fluctuations, and electron (quasiparticle) density for electronic (superconducting) excitations etc. By introducing ξ term to the polarization relation in (2.1), the polarization is induced:

$$P = \epsilon_0(\chi E + \chi' \xi E) \quad (2.3)$$

Where $\chi' = d\chi/d\xi$ is the susceptibility derivative with respect to ξ . The first term in equation (2.3) drives the polarization at the incident field frequency, contributing to the elastic scattering. Being ξ time dependent the second term modulates the induced polarization at different frequencies respect to the incident field frequency. In other words, it accounts for the inelastic response of the system. By the point of view of the vibrational dynamics, the dynamical variable becomes the displacement q from the equilibrium configuration (vibration's amplitude). Thus, the induced electric dipole moment of a diatomic molecule can be simply written as:

$$P = \alpha E = \alpha E_0 \cos(\nu_0 t) \quad (2.4)$$

where α is a proportionality constant namely *molecular electronic polarizability*. In general, for a multi-atomic molecule, the induced dipole moment \vec{P} will be induced by the electric field through the relation: $\vec{P} = \vec{\alpha} \vec{E}$ where $\vec{\alpha}$ is the polarizability tensor. Using k to indicate different normal coordinates of the molecule, the polarizability α can be expanded as a Taylor series:

$$\alpha = \alpha_0 + \left(\frac{\partial \alpha}{\partial q_k} \right)_0 q_k + \left(\frac{\partial^2 \alpha}{\partial q_k^2} \right) \frac{q_k^2}{2} + \dots \quad (2.5)$$

Where q_k is the displacement amplitude of the k_{th} normal mode, α_0 is the polarizability at the equilibrium position, $\left(\frac{\partial\alpha}{\partial q_k}\right)_0$ and $\left(\frac{\partial^2\alpha}{\partial q_k^2}\right)_0$ are the first and the second derivatives of the polarizability α at the equilibrium position. On the other hand, for a molecule vibrating with frequency ν_k the nuclear displacement q_k is:

$$q_k = q_k^0 \cos(\nu_k t) \quad (2.6)$$

From equations (2.5) and (2.6) we get:

$$P = \alpha_0 E_0 \cos(\nu_0 t) + \left(\frac{\partial\alpha}{\partial q_k}\right)_0 E_0 q_k \cos(\nu_0 t) \quad (2.7)$$

$$P = \alpha_0 E_0 \cos(\nu_0 t) + \left(\frac{\partial\alpha}{\partial q_k}\right)_0 E_0 q_k^0 \cos(\nu_0 t) \cos(\nu_k t) \quad (2.8)$$

$$P = \alpha_0 E_0 \cos(\nu_0 t) + \left(\frac{\partial\alpha}{\partial q_k}\right)_0 E_0 q_k^0 \frac{1}{2} [\cos(\nu_0 + \nu_k)t + \cos(\nu_0 - \nu_k)t] \quad (2.9)$$

The first of the terms in (2.9) accounts for the Rayleigh scattering, while the second term concerns Stokes, and their anti-Stokes Raman scattering¹²⁶.

One of the key-parameter in Raman spectroscopy is the wavenumber which is defined as $\omega = \nu/c = 1/\lambda$, having the typical dimension of cm^{-1} . This concept is crucial since molecule interacting with an electromagnetic field, the transfer of energy can occur if and only if the Bohr's frequency condition is satisfied according to $\Delta E = h\nu = (hc)/\lambda = hc\omega$. Thus, ω is directly proportional to the transition energy. However, since the expression frequency shift is conventionally used in Raman spectroscopy¹²⁶, we refer to the wavenumber as frequency shift (ω) in cm^{-1} .

2.2. RAMAN SCATTERING IN GLASSES

Breaking the selection rules

Considering the conservation energy law, the incoming laser beam with frequency ω_i , the propagation vector \vec{k}_i , and the scattered \vec{k}_o , will have a scattered frequency called ω_o . The scattering process can be represented by the relation $\omega = \omega_i - \omega_o$ and the wave vector is $\vec{k} = \vec{k}_i - \vec{k}_o$. Moreover, due to momentum conservation, in the first-order processes, the scattering wave vector will be equal to the excitation wave vector: $\vec{k} = \vec{q}$. Thus, in the first-order processes, only a single elementary excitation participates and represents the selection rule for the Raman spectroscopy of crystals. It is worth to note that Raman spectroscopy of crystal only probe the optical phonon branches, as stated in section 1.2.

In glasses the periodicity is completely lost and the additionally absence of reciprocity excludes \vec{k} as a proper parameter to label the Raman modes of glasses. Thus, the selection rule for the first-order Raman scattering breaks down for amorphous systems. For a perfect plane-wave phonon mode with finite wave vector \vec{q} , the disorder of the atomic coupling allows inelastic scattering of light from this mode. With the \vec{q} component of the random spatial distribution of atomic couplings, the phonon \vec{q} is flooded back to yield a $\vec{k} = 0$ component of the fluctuating dielectric polarizability which can be measured by light scattering¹²⁷. This leads to a continuous first-order vibrational spectrum of glasses instead of the discrete Raman spectrum of crystals. Here the disorder controls:

- I. coupling between the atomic displacement and the fluctuation of the dielectric function, and is referred as to “electrical disorder”
- II. the vibrational modes of the glass are not plane waves inducing distortion of the wavefront of the vibrational modes and is referred as to “mechanical disorder”.

The effect of the mechanical disorder on the Raman scattering was first explained by Shuker and Gamon in 1970¹²⁸ opening different picturing of the problem^{129,130}. They define a correlation length $R(\omega)$ over which a vibrational mode of frequency $\omega/2\pi$ represents a plane wave and argue that the wave-vector selection rule is annulled as soon as $R(\omega)$ is as short as the wavelength of the mode.

Raman density of states

In this section will be briefly treated the typical Raman spectra of a silicate glass, with particular focus on the polarization effect on the low-frequency region, as well as its treatment and analytical procedure adopted as standard protocol all over this study. The sample used as test-example (Figure 2.2) for this section is a SiO₂ suprasil® with a typical impurity of 100-300 ppm of OH.

The HH spectrum reported in Figure 2.2 a) shows a broad polarized band at ~ 440 cm⁻¹, namely the R band, which is peculiar of highly polymerized silicate glasses and is usually related to the rocking and symmetric bending motions of bridging oxygen along the T-O-T inter-tetrahedral bonds^{131,132}. The sharp components at ~ 490 cm⁻¹ and at 600 cm⁻¹, D1 and D2 band respectively, are due to symmetric bending vibrations of bridging oxygen in 4- and 3-membered rings¹³³. However these bands, being strongly polarized, turn out inactive in the crossed polarized (HV) spectra¹³⁴, Figure 2.2 b). The band at ~ 800 cm⁻¹ arises from the three-fold degenerate “rigid cage” vibrational mode of SiO₂ units¹³⁵. The high-frequency region between 850 and 1250 cm⁻¹ is dominated by the stretching vibrations of tetrahedral SiO₄ units. A common nomenclature used to unravel the effect of chemistry effect on the polymerization of the system is known as Q^n notation^{131,133,136}, where n is the number of bridging oxygens (BOs) per tetrahedron T. A tetrahedron fully linked into the network via four bridging oxygens is designated as a Q^4 unit (the term unit will be used for structural elements having only one silicon atom, for example the SiO₄ tetrahedron), while an isolated tetrahedron with no bridging oxygens is designated as a Q^0 units. The vibrational units with the number of bridging oxygens of one, two and three is designated as Q^1 , Q^2 and Q^3 respectively. The main advantage of the Q^n notation is that it is applicable to all silicate compositions.

Some studies^{137,138} introduced the T^{2s} band, which corresponds to the Si-O asymmetric stretching mode of SiO₂ tetrahedra. Others^{102,139,140} adopted the analysis of the Q^4 band (arising from the stretching mode involving Si or Al) separating the component at ~ 1140 cm⁻¹ (smaller T-O-T angles) namely $Q^{4,II}$ and one at ~ 1190 cm⁻¹ (wider T-O-T angles) namely $Q^{4,I}$.

However, this procedure will be applied only to the case discussed in Appendix II.

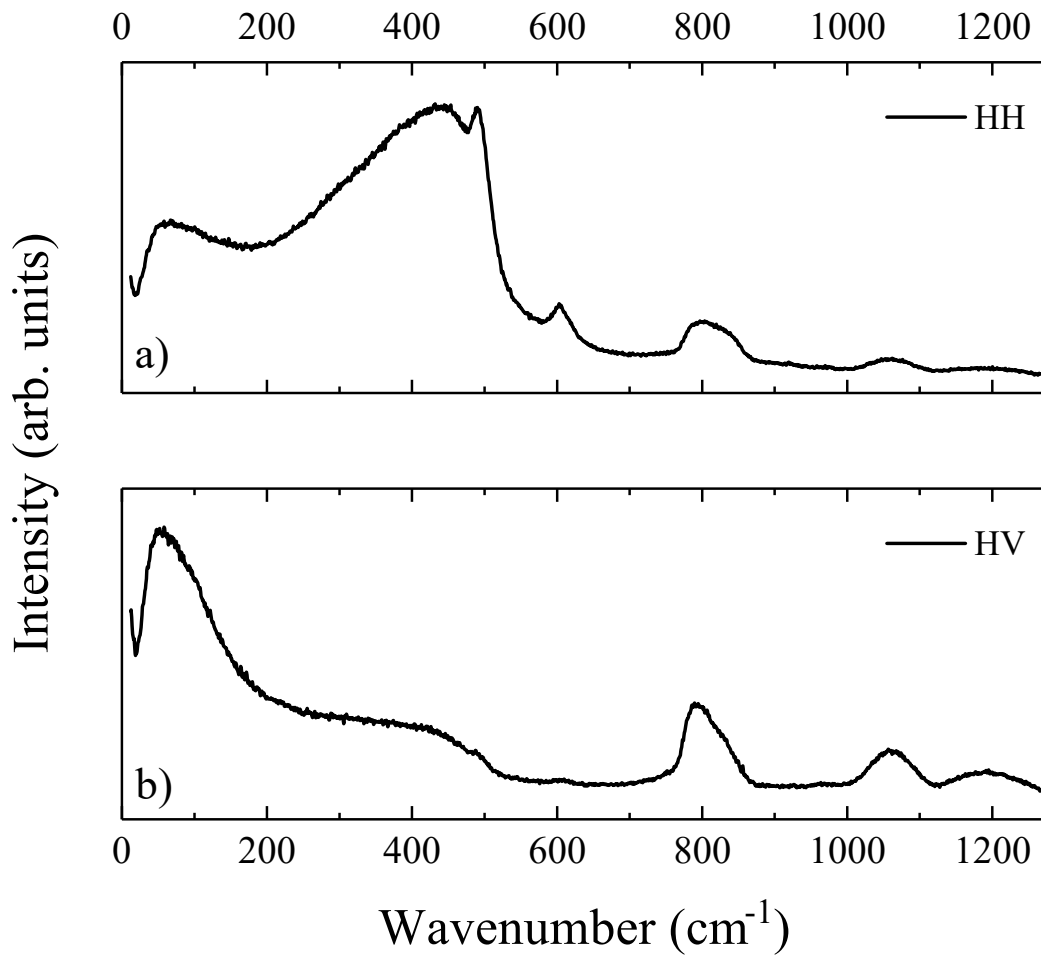


Figure 2.2 Raman spectrum of SiO₂ (suprasil®) in a) HH parallel polarization and b) HV crossed polarization. See text for the measurement conditions.

The low-frequency region of the HV spectra Figure 2.2 b) is characterized by the strong appearance of the BP between 20 and 200 cm⁻¹. Below this spectral region, i.e.:

for frequencies $\omega \lesssim 20 \text{ cm}^{-1}$, the spectrum generally shows an increase in intensity due to the quasi-elastic scattering (QES), which does not overlap with the BP, even if in some cases is very shortly extended below its low-frequency tail. Following these observations, in order to minimize the effect of the 460 cm^{-1} band superimposition^{133,141}, the whole evaluation of the BP is based on the HV spectra¹⁴².

The main aspect in treating electromagnetic waves in the Raman scattering experiment (as well as neutrons) is linking the intensity at the BP frequency to the Bose-Einstein statistics. Following, scattered light depends not only on the vibrational density of states, but also on the coupling between photons and vibrations. Thus, for a first-order Raman scattering experiment, the experimental intensity I^{obs} is proportional to the vibrational density of states (VDOS) $g(\omega)$.¹²⁸ and the relationship between Raman intensity and density of states reads:

$$I^{obs}(\omega) = C(\omega)g(\omega) \frac{[n(\omega, T) + 1]}{\omega} \quad (2.10)$$

Where $C(\omega)$ is the light-vibrations coupling function, $n(\omega, T) = [\exp(\hbar\omega/k_B T) - 1]^{-1}$ is the Bose-Einstein population factor, while k_B and \hbar are the Boltzmann and the reduced Planck constants, respectively. Dividing the Raman intensity by $[n(\omega, T) + 1]$ and ω , we obtain the reduced Raman intensity $I^{red}(\omega)$, which is proportional to the reduced density of vibrational states $g(\omega)/\omega^2$:

$$I^{red}(\omega) = C(\omega) \frac{g(\omega)}{\omega^2} \quad (2.11)$$

Thus, the peak of $I^{red}(\omega)$ is essentially the peak in $g(\omega)/\omega^2$ unlike in $C(\omega)$ which is assumed to be $C(\omega) \sim \omega$, thus found to depend approximately linearly on frequency in the region of the BP, for a wide number of glasses^{143–145}. The result of the treatment is reported in Figure 2.3.

In this study, we consider only the BP position defined as the maximum in the reduced intensity and obtained from a fit with a log-normal function following the procedure proposed by Malinovsky and co-workers¹⁴⁶:

$$I(\omega) = \exp -\{[\ln(\omega/\omega_{BP})]^2/2\Gamma^2\} \quad (2.12)$$

where Γ is the width of the BP.

In the inset of Figure 2.3 is reported the boson peak plotted in the reduced intensity and fitted to the log-normal. It is worth noting that after the treatment the BP is much more pronounced respect to the other spectral components. Another effect of the treatment produces also a small shift to lower frequencies.

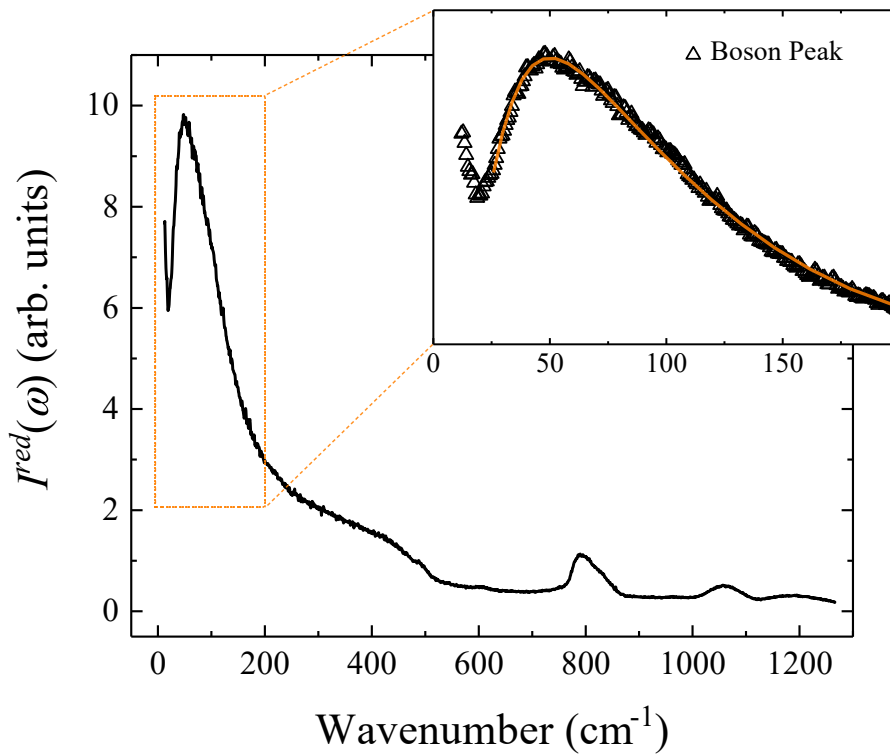


Figure 2.3 Reduce spectra of SiO₂ suprasil® obtained as discussed in the text. The inset shows the boson peak together with the fit to a log-normal (2.12) represented by the orange solid-line.

2.3. EXPERIMENTAL SETUP

Raman

In order to get the best possible resolution of data and avoid unwanted effect on data reliability, each component must be properly selected and designed to fit into the experimental setup.

The optical layout of a typical setup for micro-Raman spectroscopy, which is schematically drawn in Figure 2.4 and is composed by:

1. Excitation source
2. Optical system exploited for laser beam focusing onto the samples and for collecting the scattered radiation from them
3. Filter system for the Rayleigh component cut-off.
4. Spectrograph as dispersive element.
5. Photon detector.

In this study, all the Raman spectra has been acquired with a confocal approach and in back-scattering geometry using a triple-axis monochromator set in a double subtractive single configuration (Horiba-Jobin Yvon, model T-64000). The scattered radiation was filtered by three holographic gratings (1800 lines/mm) and detected by a CCD detector (1024x256 pixels) cooled by liquid nitrogen. The exciting radiation was provided by a mixed Ar-Kr ion gas laser (Spectra Physics Satellite 2018 RM) set at 514.5 nm. The laser beam was focused onto a spot of about 2 μm by using a 50x objective with NA = 0.50. The power on the sample surface was fixed at about 10mW. Measurements were done at room temperature in air. Samples were polished and optically inspected before and after the measurements without observing appreciable alteration on the μm -length scale. Measurements of the Stokes-shifted spectra, in the frequency region between 10 and 1300 cm^{-1} , with an average spectral resolution of about 0.6 cm^{-1} /pixel, were acquired in parallel (HH) and crossed (HV) polarization. Each spectrum was corrected by subtracting the

rotational Raman spectrum of air, occurring in the low-frequency region below 180 cm^{-1} , and a linear baseline, extending over the full spectral range, to account for the weak luminescence background.

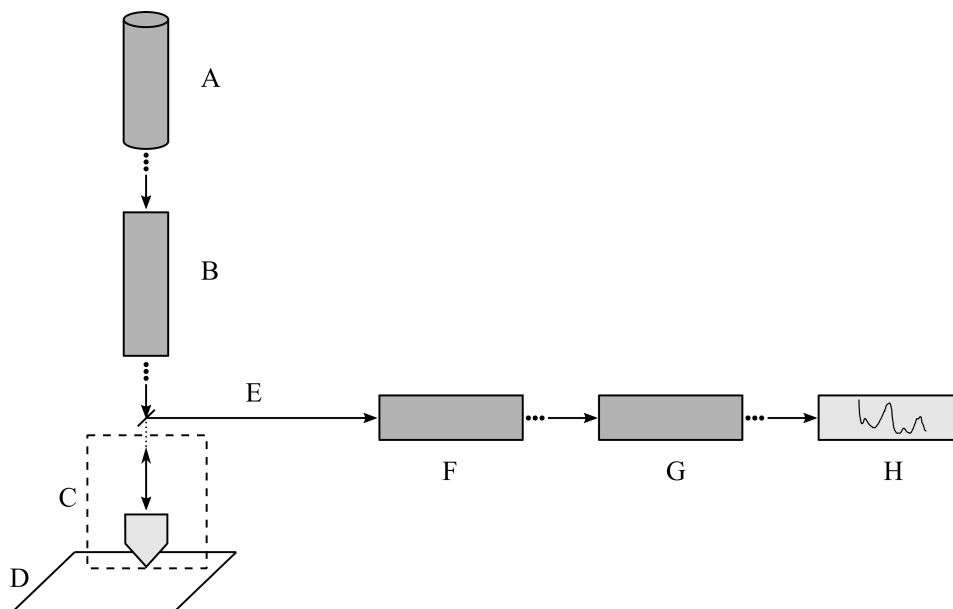


Figure 2.4 Schematic representation of the experimental setup for micro-Raman spectroscopy, showing the path of light during spectra excitation and detection. A: laser source, B: pre-monochromator, C: microscope, D: sample stage, E: scattered light, F: Raman spectrometer (fore monochromator and spectrograph), G: detector (charge coupled detector), and H: signal processing units.

A mixed Ar-Kr ion gas-laser (Spectra-Physics; Model: 2018RM03) operated in the visible range of the spectrum between Infrared and UV region has been used as the excitation sources for exciting the Raman spectra in this study. Inside the laser assembly, there is a prism that we can turn to choose the line of laser used for our analysis.

The output of the mixed Ar-Kr ion gas-laser is passed through the pre-monochromator toward the sample. Plasma lines (extraneous lines) from the gas laser i.e. spontaneous decay of Ar^+/Kr^+ ions between various transition lines which are not resonant with the optical cavity is filtered out by the pre-monochromator before to reach to the sample.

In this study, an OLYMPUS BX41 microscope (equipped with a manually operated sample stage facilitating X, Y and Z translations, microscope objective lens and camera

which is interfaced to the objective of the microscope) coupled with monochromator has been used to excite the sample as well as collect the scattering light. One beam splitter is used to send the backscattered light coming from the objective to the camera interfaced to the system. The in-built microscope has four objectives: 10X with numerical aperture (NA=0.25), 50X (NA = 0.7), 80X (NA = 0.75) and 100X (NA = 0.9), of which only 50X, 80X and 100X objectives were used to carry out Raman spectra.

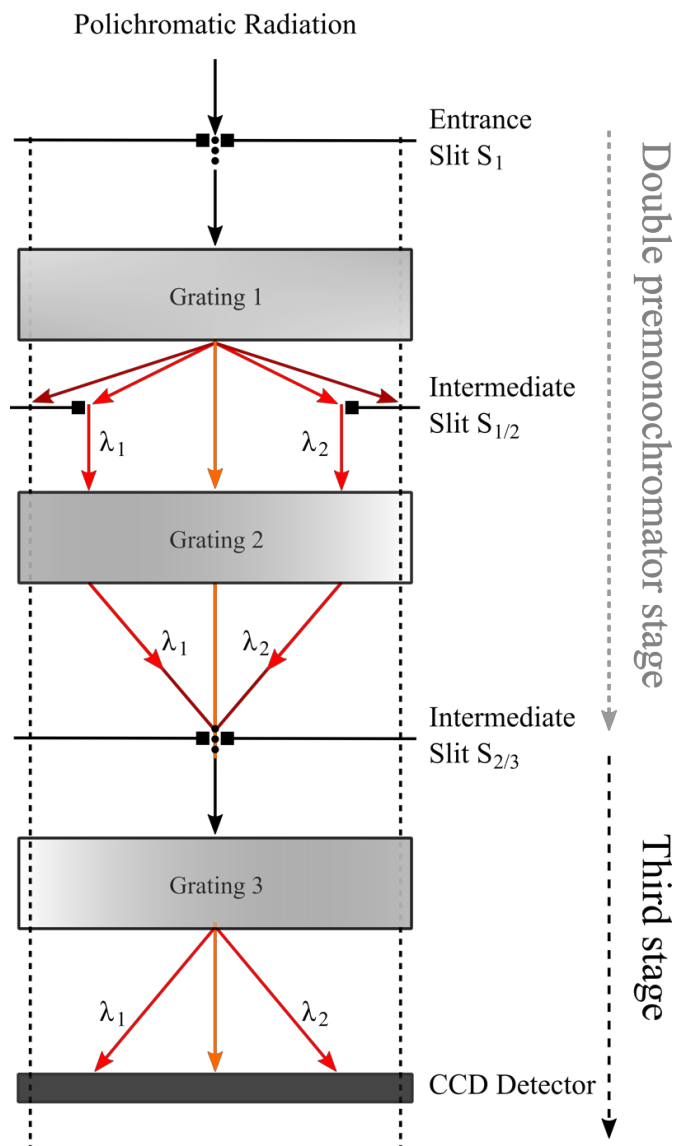


Figure 2.5 Conceptual scheme of configuration of double subtractive ferromonochromator and spectrograph in T-64000 micro-Raman spectrometer. Readapted after Adar et al. 2003¹⁴⁷

In this study, micro-Raman spectra were collected in backscattering geometry using a triple-axis monochromator (Horiba-Jobin Yvon, model T-64000), set in double-subtractive/single configuration, and equipped with a set of mirrors and holographic gratings having 1800 lines/mm. The optical diagram of the optical system used in T-64000 micro-Raman spectrometer is shown in Figure 2.5. The double subtractive foremonochromator is used as a tunable filter in the spectral range defined by the scanning mechanism and the gratings. A polychromatic radiation enters the first monochromator through the entrance slit S_1 and is dispersed by the Grating 1. The exit slit of the first monochromator (entrance slit of the 2nd monochromator) $S_{1/2}$ selects a bandpass between λ_1 and λ_2 . The Grating 2 in the 2nd monochromator recombines all the dispersed radiations on the exit slit $S_{2/3}$ giving again a polychromatic radiation, but limited to only the spectral range between λ_1 and λ_2 . Spectrometers (which include monochromators and polychromators) can be classified as dispersive and non-dispersive. Dispersive spectrometers deliver light to a position that varies continuously with wavelength. A dispersive polychromator is called spectrograph. The spectrograph is used in our system as a disperser. The polychromatic radiation selected by the foremonochromator between λ_1 and λ_2 is dispersed by the Grating 3 of the spectrograph (see Figure 2.5) and send to the detector.

The spectrum is finally acquired with a multichannel detector which is mounted in the plane of the exit image. In our T64000 system, multichannel LN₂ CCD detectors (1024×256 pixels and pixel size 26 μm × 26 μm), cooled by liquid nitrogen down to 140K is used to get the highest performance of the system.

Brillouin

Brillouin spectroscopy (BLS) analysis were carried out at ambient condition using a solid-state Nd:YVO₄ laser source with a wavelength of $\lambda = 532$ nm and a nominal power of 50 mW. Samples were treated in order to obtain the suitable size for the measurements typically of 50 μm thick and double-sided polished glasses. The Brillouin frequency shift was quantified using a six-pass Fabry-Perot interferometer¹⁴⁸ combined

with a single-pixel photon counter detector. The measurements were conducted using a symmetric forward scattering geometry^{149,150} with a scattering angle $\theta = 79.8^\circ$. The scattering angle was calibrated using a silica reference glass. Experimentally determined frequency shifts ($\Delta\omega$) were converted to longitudinal (v_L) and transverse (v_T) sound velocities according to the equation:

$$v = \frac{\Delta\omega\lambda}{2 \sin(\theta/2)} \quad (2.13)$$

where λ is the laser wavelength in air. We explored the potential effect of sample tilting on the measured velocities by collecting between 8 and 9 spectra for each sample at different rotation angle ϕ (from -180 to $+180^\circ$). Longitudinal and shear sound velocities have an average difference of 11 ± 5 m/s and 12 ± 3 m/s, respectively, which are within the 2σ uncertainties of the measurements.

3. SAMPLE SELECTION

3.1. MATERIALS

We subjected 16 anhydrous glasses to Raman and Brillouin spectroscopic analyses. Table 4.1 lists the chemistry of samples used for spectroscopic analyses. Eight samples consist of synthetic iron-bearing calcalkaline rhyolitic glasses (Rh series) used for viscometry by Di Genova et al.¹¹¹. Furthermore, we used 4 natural and iron-bearing glasses obtained by melting volcanic rocks: a dacite¹⁵¹ (HO) from Mt. Fuji volcano (Japan), an andesite¹⁵² (MSA) from Montserrat, a trachybasalt²⁰ (Etn) from Mt. Etna volcano (Italy) and a basalt from Stromboli volcano (Str). Finally, 4 iron-free glasses from Di Genova et al.²⁰ were selected; two fully polymerized glasses (anorthite An and cordierite Crd) and two depolymerized glasses (the standard glass DGG-1 and diopside Di).

3.2. LITERATURE DATA

Viscosity data of the iron-bearing calcalkaline rhyolitic samples are provided by Di Genova et al.¹¹¹, whilst for the MSA we used data from Neuville et al.¹⁵³ who measured the viscosity of an andesite melt (SiO₂ 61.2 wt.%) chemically equivalent with our MSA sample (Table 4.2). Giordano et al.¹⁵⁴ and Misiti et al.¹⁵⁵ measured the viscosity for the Str basalt. The glass transition temperature of the Etn trachybasalt glass was measured by Di Genova et al.²⁰. Low-temperature viscosity data of the standard glass DDG-1, diopside (Di), anorthite (An), cordierite (Crd) are provided by Di Genova et al.²⁰ and Al-Mukadam et al.¹⁵⁶. High-temperature viscosity data for these systems are listed elsewhere^{9,157–162}. No viscosity data of nanocrystal-free melts are available for Etn²⁰ and dacite (HO) melts.

The viscosity data for SiO₂ are those from Urbain et al.¹⁶¹ and Bucaro and Dardy¹⁶³, whilst for GeO₂ were provided by Napolitano and Macedo¹⁶⁴ for the high-viscosity regime and by Sharma et al.¹⁶⁵ for the low-viscosity regime.

We drew on the Brillouin spectroscopy literature of multicomponent systems of volcanological interest. Table 4.2 lists Brillouin data for those glasses whose $\eta_s(T)$ of the corresponding liquid is known. Brillouin and viscosity data of anhydrous peralkaline haplogranitic glasses (HPG8_Li05, HPG8_Na05, HPG8_K05) were provided by Hushur et al.¹⁶⁶ and Hess et al.¹⁶⁷, respectively. Richet and Polian¹⁶⁸ and Richet et al.¹⁷ measured respectively Brillouin velocities and $\eta_s(T)$ for anhydrous and hydrous iron-free andesitic glasses (And). Richet and Polian¹⁶⁸ measured Brillouin velocities from compacted and relaxed glasses. We use the data obtained from the relaxed samples since a complete dataset for both dry and hydrous glasses is provided. Whittington et al.^{112,169}, Robert et al.¹⁷⁰ and Robert¹⁷¹ reported Brillouin and viscosity data for anhydrous and hydrous iron-free phonolite (Phon), basalt (Bas), and foidite (Foid) systems. We calculated the average velocities for each sample when more measurements on the same sample were performed. Furthermore, we included Brillouin velocities (Novikov et al.²³ and references therein) of fully-polymerized glass-forming systems such as SiO₂ and GeO₂. Furthermore, we constrained the relationship between the melt fragility m and Brillouin-derived elastic moduli, bulk (K) and shear (G), over the largest landscape possible by introducing a synthetic and perfectly strong sample (Synth) characterized by $m = 14.97$ and a ratio of $K/G = 1^{23}$. The value of fragility was derived by previous studies^{84,172} that used the MYEGA formulation η_s (1.18) and the assumption of $\eta_\infty = 10^{-2.93}$ Pa s (see ref.¹⁷²) on which our study is based. Yet simultaneously the K/G ratio for strong glasses is not expected to be lower than 1^{23} . Finally, the boson peak position ω_{BP} of SiO₂ and GeO₂ glasses is given by Zanatta et al.^{70,173}.

4. RESULTS

Table 4.1 lists the chemical composition of glasses considered in this study. We measured the vibrational properties of 16 anhydrous samples (from RhA to Di) using BLS and RS (the low-frequency Raman spectra are reported in Figure 4.1), whereas data of 11 anhydrous samples (from SiO₂ to HPG8_Li05) were collected from the literature (see references in Table 4.1).

	SiO ₂	TiO ₂	Al ₂ O ₃	FeO _{tot.}	MnO	MgO	CaO	Na ₂ O	K ₂ O	Fe ₂ O ₃ /GeO ₂ /Li ₂ O/P ₂ O/S O ₃	Ref.
RhA	77.63	0.11	12.73	3.03	0.03	0.06	0.92	4.44	1.62	-	111
RhB	77.28	0.14	13.39	2.94	0.02	0.06	0.75	2.71	3.61	0.03 (P ₂ O ₅)	111
RhD	76.83	0.11	12.43	2.96	0.05	0.07	0.9	2.93	4.29	0.04 (P ₂ O ₅)	111
RhE	75.33	0.12	13.61	2.93	0.03	0.07	0.88	1.41	6.80	0.06 (P ₂ O ₅)	111
RhG	77.86	0.12	11.69	2.99	0.04	0.07	0.85	1.05	5.34	-	111
RhH	77.25	0.10	11.95	2.62	0.06	0.22	1.08	3.23	4.35	0.05 (P ₂ O ₅)	111
RhI	76.24	0.06	11.46	2.85	0.03	0.44	1.31	2.99	3.83	0.04 (P ₂ O ₅)	111
RhJ	73.75	0.31	11.99	3.31	0.07	1.64	2.98	3.16	3.56	0.02 (P ₂ O ₅)	111
MSA	59.58	0.58	17.94	6.28	0.20	2.86	7.71	3.75	0.84	-	152
HO	66.17	0.77	15.96	5.02	0.12	1.70	4.65	3.70	2.23	0.1 (P ₂ O ₅)	151
Str	49.30	0.86	16.90	8.09	0.16	6.12	12.00	2.74	2.14	0.5 (P ₂ O ₅)	*
Etn	48.09	1.70	17.05	10.11	0.25	5.57	10.22	3.75	1.87	-	20
DGG-1	71.72	0.14	1.23	-	-	4.18	6.73	14.95	0.38	0.19 (Fe ₂ O ₃); 0.44 (SO ₃)	20
An	43.19	-	36.65	-	-	-	20.16	-	-	-	20
CrD	52.26	-	34.66	-	-	12.90	0.17	-	-	-	20
Di	55.35	-	-	-	-	18.46	26.19	-	-	-	20
SiO ₂	100	-	-	-	-	-	-	-	-	-	161,173
GeO ₂	-	-	-	-	-	-	-	-	-	100 (GeO ₂)	70,164,165
And	62.40	0.55	20.01	-	0.02	3.22	9.08	3.52	0.93	-	17
Bas	50.22	2.63	18.91	-	-	11.15	12.46	3.19	1.40	-	169
Phon	58.82	0.79	19.42	-	-	1.87	2.35	9.31	7.44	-	169
Trach	64.45	0.50	16.71	-	-	2.92	5.36	6.70	3.37	-	169
Teph	50.56	2.35	14.03	-	-	8.79	15.00	7.04	3.01	-	169
Foid	43.57	2.97	10.18	-	-	9.17	26.07	7.59	0.96	-	169
HPG8_Na05	74.10	-	11.70	-	-	-	-	9.00	4.40	-	166
HPG8_K05	74.60	-	11.80	-	-	-	-	4.40	9.20	-	166
HPG8_Li05	73.20	-	12.90	-	-	-	-	4.3	4.40	4.9 (Li ₂ O)	166

*This study

Table 4.1 Chemical composition (wt.%) of samples used and considered in this study.

Moreover, an additional set of 21 anhydrous and hydrous samples (Table 4.1) was included in the dataset for the external validation of our approach.

The measured sound velocities are listed Table 4.2, together with those provided by the literature. The longitudinal sound velocity increases with decreasing the SiO₂ content (Table 4.2), namely the calcalkaline rhyolites exhibit the lowest v_L (between 5773 and 5870 m s⁻¹), whereas the highest velocity (6727 m s⁻¹) was measured for the diopside (Di). The shear velocity does not show a significant dependence on the chemical composition and ranges between 3550 m s⁻¹ for the calcalkaline rhyolite RhE and 3753 m s⁻¹ (anorthite, An). Our results are in line with those from Wittington et. al.¹⁶⁹ who studied similar multicomponent and FeO-free melts and found that the SiO₂-rich albite exhibited the lowest v_L (5533 m s⁻¹), whereas the SiO₂-poor basalt was characterized by the highest longitudinal velocity (6505 m s⁻¹).

The K/G ratio is calculated from the measured v_L and v_T as following²³:

$$K/G = (v_L/v_T)^2 - 4/3 \quad (4.2)$$

Because the Brillouin spectroscopy probes the elastic properties at frequencies much higher than the structural relaxation time, here we assume that the derived K/G approaches the ratio of the instantaneous values K_∞ and G_∞ ^{23,24}. Table 4.2 lists the calculated K/G for samples subjected to BLS measurements here^{20,111,151,152} and elsewhere^{23,166,168,169,173} which are reported in Figure 4.2 a) as a function of SiO₂ in mol.%. We use the SiO₂ content (mol.%) as a chemical proxy to plot K/G in Figure 4.2 a) because the samples considered in this study are silicate systems. However, in the discussion section, we also include the GeO₂ glass for which both Brillouin and Raman spectroscopic data are available. This allows the incursion into an exotic chemical space of glass-forming melts and thus further test our findings. The derived ratio of elastic moduli K/G ranges between 1.08 for the pure SiO₂ provided by Novikov et al.²³ and 1.90 for diopside (Di, SiO₂ ~50 mol.%) measured here. We obtained a linear correlation (R-squared = 0.94) between the K/G ratio and the SiO₂ content x (mol.%) when all samples are considered:

$$K/G = -0.0146 x + 2.50 \quad (4.3)$$

The errors associated respectively to the two constants are 8 and 6. It is worth noting that the inspection of Figure 4.2 a) reveals that the SiO₂ from Zanatta et al.¹⁷³ exhibits a

$K/G = 1.18$ that slightly deviates from the linear relationship. We argue that such variability of K/G may stem from the dramatic structural effect of impurities (e.g., ppm of OH⁻) on the measured properties of nominally fully polymerized SiO₂ glass^{93,174}. Here we consider the K/G from Zanatta et al.¹⁷³ since they provide Brillouin velocities and Boson peak position measured from the same sample (Spectrosil®).

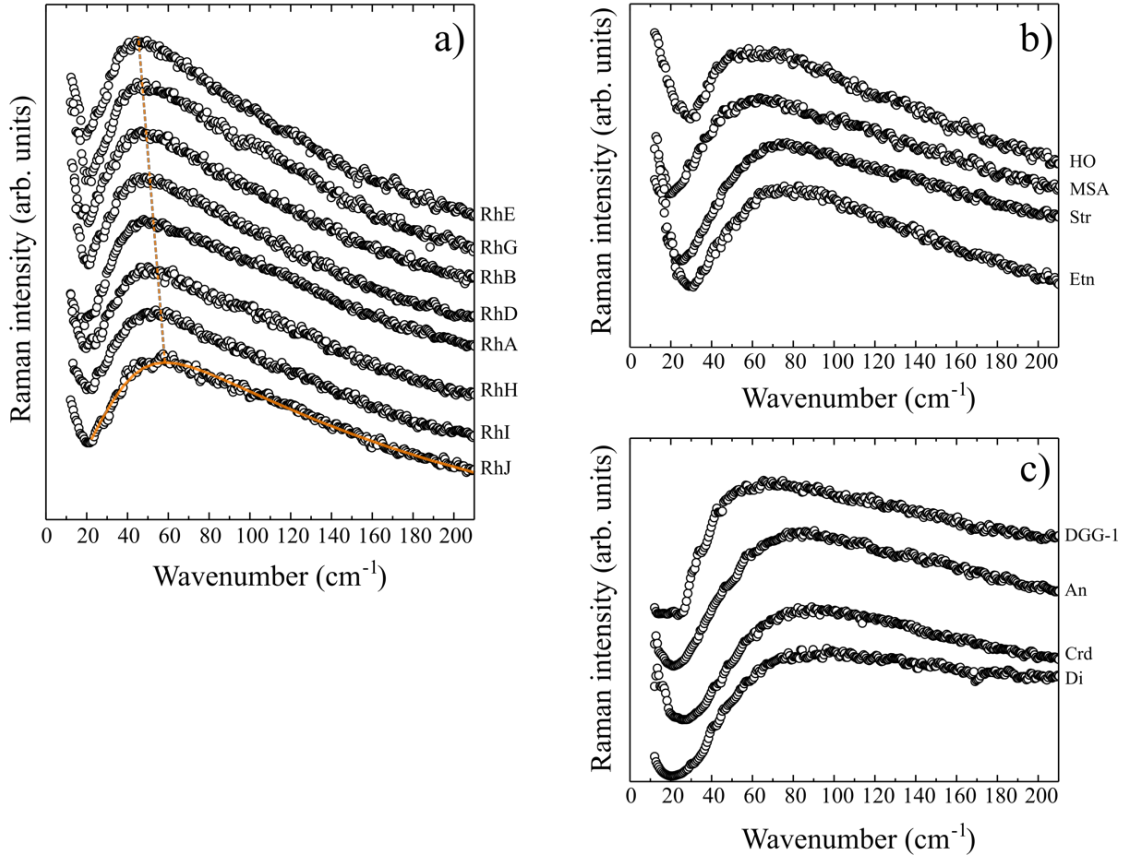


Figure 4.1 Low-frequency region of Raman spectra collected from SiO₂-rich calcalkaline rhyolites a), SiO₂-intermediate multicomponent volcanic samples b), and iron-free samples c). Spectra are shown after the subtraction of both rotational Raman spectra of the air and a linear weak luminescence background (see section 2.3). The sample chemical composition is reported in Table 4.1, whereas the boson peak position is listed in Table 4.2. Orange dashed line in a) is a line for the eye. The solid orange curve represents the log-normal fit to the BO of the sample RhJ.

The BP dominates the low-frequency region of the Raman spectra of glasses and the peak position ω_{BP} can be retrieved by fitting the low-frequency part of the cross-polarized Raman spectra with a Log-normal function¹⁴⁶ (see Figure 4.1 a), b) and c) and

section 2.2 for the low-frequency treatment). Both the derived and literature BP position ω_{BP} are listed in Table 4.2. Figure 4.2 a) shows the ω_{BP} as a function of the SiO₂ content (mol.%). With decreasing the SiO₂ content from pure silica to 50 mol.%, the ω_{BP} increases from 47.8 cm⁻¹ (RhE) to 90.0 cm⁻¹ (Di). Although data are scattered, the peak position appears to follow a linear trend with x mol.% of SiO₂ (R-squared = 0.88) given by the relation:

$$\omega_{BP} = -1.0 x + 133 \quad (4.4)$$

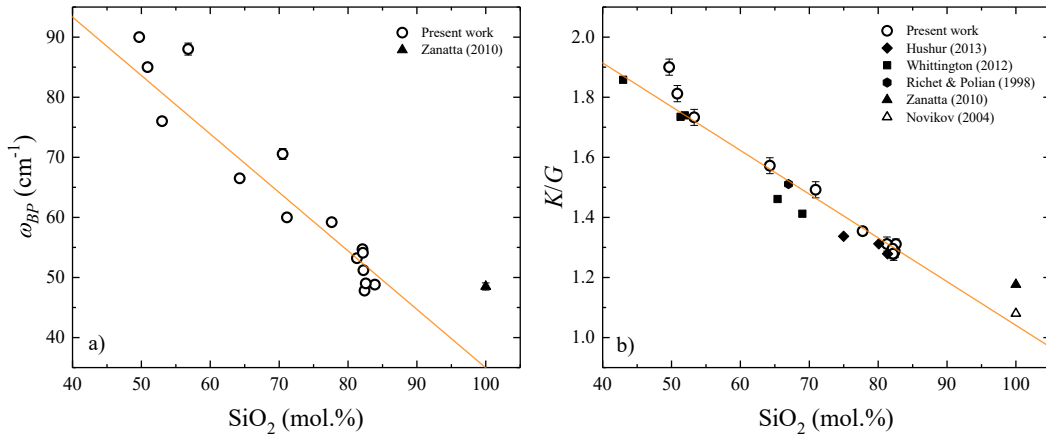


Figure 4.3 Raman a) and Brillouin b) data of samples from this study (empty circles) and the literature (filled symbols) as a function the SiO₂ (mol. %) content of glasses. The ratio of the bulk (K) and shear (G) elastic moduli is calculated (4.2) from Brillouin velocities (Table 4.2), whereas the Boson peak position ω_{BP} was retrieved by fitting the low-frequency Raman spectra of glasses using a Log-normal function (see Methods for details). Orange lines in a) and b) are linear fits of data with (4.3) and (4.4), respectively.

Sample	v_T (m s ⁻¹)	v_L (m s ⁻¹)	K/G	ω_{BP} (cm ⁻¹)	m^{MYEGA}	$m^{BLS,RS}$	T_g (K)	Ref.
RhA	3604 (13)	5835 (12)	1.29 (.02)	53.2 (.5)	25.3 (.1)	26.2; 25.1	1043.8 (1.1)	(h) ¹¹¹
RhB	3610 (8)	5869 (14)	1.28 (.02)	49.1 (.4)	27.1 (.4)	26.1; 24.6	1093.0 (3.5)	(h) ¹¹¹
RhD	3595 (8)	5810 (20)	1.28 (.02)	51.2 (.5)	27.2 (.3)	24.7; 25.3	1097.4 (2.4)	(h) ¹¹¹
RhE	3550 (14)	5773 (11)	1.31 (.02)	47.8 (.3)	26.9 (.2)	26.1; 24.2	1108.0 (2.5)	(h) ¹¹¹
RhG	-	-	-	48.8 (.4)	27.5 (.2)	24.5	1121.2 (2.0)	(h) ¹¹¹
RhH	3590 (11)	5803 (6)	1.28 (.02)	54.1 (.4)	28.5 (.2)	24.7; 26.6	1071.6 (1.5)	(h) ¹¹¹
RhI	3590 (14)	5820 (9)	1.30 (.02)	54.7 (.5)	24.9 (.1)	25.4; 24.8	1022.0 (1.5)	(h) ¹¹¹
RhJ	3581 (7)	5870 (8)	1.35 (.01)	59.2 (.5)	26.9 (.1)	28.0; 29.0	992.1 (.6)	(h) ¹¹¹
MSA	3608 (12)	6150 (16)	1.57 (.02)	66.5 (.5)	33.0 (.2)	37.4; 33.2	958.2 (.6)	(h)
HO	-	-	-	60.0 (.6)	-	29.3	-	-
Str	3569 (12)	6249 (17)	1.73 (.03)	76.0 (.5)	40.9 (.2)	44.4; 40.9	932.6 (1.0)	(h) ^{14,155}
Etn	-	-	-	78.2 (.6)	-	43.1	914.2 ^{DSC}	(T_g) ²⁰
DGG-1	3451 (13)	5900 (8)	1.49 (.02)	70.6 (.9)	33.3 (.6)	33.9; 36.1	813.0 (3)	(h) ³⁰
An	3753 (15)	6656 (9)	1.81 (.03)	85.0 (.5)	52.3 (.4)	47.8; 51.0	1128.9 (.6)	(h) ^{20,159-161}
Crd	-	-	-	88.0 (1.0)	46.6 (.2)	55.1	1087.3 (.2)	(h) ³²⁰
Di	3741 (15)	6727 (4)	1.90 (.03)	90.0 (.5)	55.5 (.4)	51.6; 58.2	993.7 (.5)	(h) ^{8,20,156-158,162}
SiO ₂	3769 (13)	5972 (20)	1.18 (.03)	48.5 (.5)	24.0 (.4)	20.3; 24.4	1427.5 (7.5)	(v_L, v_T, ω_{BP}) ¹¹² , (h) ¹⁶¹
GeO ₂	2360	3770	1.22	40.5 (.5)	20.0 (.2)	22.1; 22.0	816.6 (.9)	(v_L, v_T, ω_{BP}) ³⁶ , (h) ^{164,165}
And	3700	6240	1.51	-	36.2 (.1)	34.8	1016.4 (.3)	(v_L, v_T) ¹⁶⁸ , (h) ¹⁷
And (0.3)	3730	6250	1.47	-	-	33.2	954.4	(v_L, v_T) ¹⁶⁸ , (T_g) ^{VFT} , (h) ¹⁷
And (1)	3750	6230	1.43	-	-	31.1	869.3	(v_L, v_T) ¹⁶⁸ , (T_g) ^{VFT} , (h) ¹⁷
And (2.7)	3550	6060	1.58	-	-	37.8	756.9	(v_L, v_T) ¹⁶⁸ , (T_g) ^{VFT} , (h) ¹⁷
And (3.5)	3620	6090	1.5	-	-	34.2	734.4	(v_L, v_T) ¹⁶⁸ , (T_g) ^{VFT} , (h) ¹⁷
Bas	3711	6505	1.74	-	44.8 (.1)	44.7	983.3 (.3)	(v_L, v_T) ¹⁶⁹ , (h) ^{150,171}
Bas (3.02) [*]	3586	6230	1.68	-	-	42.2	777	(v_L, v_T) ¹⁶⁹ , (T_g) ¹⁶⁹ , (h) ¹⁷⁰
Phon	3493	5839	1.46	-	28.4 (.2)	32.6	917.7 (.8)	(v_L, v_T) ¹⁶⁹ , (h) ¹¹²
Phon (0.88) [*]	3482	5839	1.48	-	-	33.4	827	(v_L, v_T) ¹⁶⁹ , (T_g) ¹¹² , (h) ¹¹²
Phon (2.15) [*]	3394	5752	1.54	-	-	36	684	(v_L, v_T) ¹⁶⁹ , (T_g) ¹¹² , (h) ¹¹²
Phon (2.83) [*]	3372	5692	1.52	-	-	34	658	(v_L, v_T) ¹⁶⁹ , (T_g) ¹¹² , (h) ¹¹²
Phon (4.72) [*]	3372	5768	1.59	-	-	38.3	596	(v_L, v_T) ¹⁶⁹ , (T_g) ¹¹² , (h) ¹¹²
Trach	3580	5932	1.41	-	31.1 (.1)	30.5	969.8 (.6)	(v_L, v_T) ¹⁶⁹ , (h) ¹¹²
Trach (0.57) [*]	3427	5725	1.46	-	-	32.4	883	(v_L, v_T) ¹⁶⁹ , (T_g) ¹¹² , (h) ¹¹²
Trach (0.83) [*]	3416	5741	1.49	-	-	33.9	838	(v_L, v_T) ¹⁶⁹ , (T_g) ¹¹² , (h) ¹¹²
Trach (1.19) [*]	3394	5708	1.5	-	-	34.1	800	(v_L, v_T) ¹⁶⁹ , (T_g) ¹¹² , (h) ¹¹²
Trach (2.19) [*]	3351	5664	1.52	-	-	35.3	733	(v_L, v_T) ¹⁶⁹ , (T_g) ¹¹² , (h) ¹¹²
Trach (2.90) [*]	3373	5681	1.5	-	-	34.4	698	(v_L, v_T) ¹⁶⁹ , (T_g) ¹¹² , (h) ¹¹²
Trach (4.92) [*]	3329	5654	1.55	-	-	36.5	628	(v_L, v_T) ¹⁶⁹ , (T_g) ¹¹² , (h) ¹¹²
Teph	3558	6232	1.73	-	45.2 (.8)	44.5	932.8	(v_L, v_T) ¹⁶⁹ , (T_g) ^{VFT} , (h) ¹¹²
Teph (0.92) [*]	3580	6260	1.72	-	-	44	842.4	(v_L, v_T) ¹⁶⁹ , (T_g) ^{VFT} , (h) ¹¹²
Teph (1.60) [*]	3591	6282	1.73	-	-	44.1	814.1	(v_L, v_T) ¹⁶⁹ , (T_g) ^{VFT} , (h) ¹¹²
Teph (2.27) [*]	3591	6243	1.69	-	-	42.5	793.8	(v_L, v_T) ¹⁶⁹ , (T_g) ^{VFT} , (h) ¹¹²
Foid	3525	6297	1.86	-	49.5 (.2)	49.8	915.8 (.2)	(v_L, v_T) ¹⁶⁹ , (h) ¹¹⁵
Foid (1.00)	3525	6254	1.81	-	-	47.9	822.1	(v_L, v_T) ¹⁶⁹ , (T_g) ^{VFT} , (h) ¹¹⁵
Foid (1.35)	3558	6308	1.81	-	-	47.7	806.4	(v_L, v_T) ¹⁶⁹ , (T_g) ^{VFT} , (h) ¹¹⁵
Foid (1.88)	3514	6265	1.85	-	-	49.3	769	(v_L, v_T) ¹⁶⁹ , (T_g) ^{VFT} , (h) ¹¹⁵
HPG8_Na05	3560	5790	1.31	-	23.2 (.1)	26.1	854.6 (1.4)	(v_L, v_T) ¹⁶⁶ , (h) ¹⁶⁷
HPG8_K05	3540	5721	1.28	-	22.5 (.1)	24.7	888.8 (1.0)	(v_L, v_T) ¹⁶⁶ , (h) ¹⁶⁷
HPG8_Li05	3690	6030	1.34	-	25.3 (.2)	27.2	773.0 (1.3)	(v_L, v_T) ¹⁶⁶ , (h) ¹⁶⁷

Acoustic wave velocities (v_L and v_T), elastic moduli ratio (K/G , (5.1)), and Boson peak position (ω_{BP}). From sample RhA to sample Di, Brillouin and Raman spectroscopic measurements are from this study. m^{BLS} Calculated using Brillouin data (K/G) and (5.1); m^{RS} Calculated using Raman data (ω_{BP}) and (5.2); m^{MYEGA} and T_g (unless specified in the References column) are derived using (1.18) and viscosity data from the literature (assuming $\eta_{\infty} = 10^{-2.93}$ Pa s); T_g^{VFT} Calculated here using VFT parameters provided by literature; T_g^{DSC} Glass transition temperature derived via DSC in ref.²⁰ for Etn; * H₂O content in wt.%. External samples used for validation (Figure 5.3 and Figure 5.5) are RhB, Teph (dry and hydrous) and Trach (dry and hydrous) for the BLS approach, and RhB, MSA and Str for the RS approach.

Table 4.2 Brillouin and Raman data, as well as MYEGA parameters (m and T_g) from this study and the literature.

5. DISCUSSION

The prospect of estimating the melt viscosity from the spectroscopic analysis of their parental glasses is firstly based on the identification of a relationship between the melt fragility m and the glass transition temperature T_g (1.18) with at least one of the Brillouin- and Raman-derived parameters, namely the ratio of the bulk and shear moduli K/G and ω_{BP} . This can be addressed with anhydrous melts for which the reliable estimation of m and T_g can be achieved by combining high- and low-viscosity data measured by micropenetration, parallel plate and concentric cylinder viscometry. We collected the anhydrous viscosity data ($N = 468$) from the literature (Table 4.2) and use the MYEGA formulation (1.18) assuming $\eta_\infty = 10^{-2.93}$ Pa s (see ref.¹⁷²) to derive m and T_g (Table 4.2) of anhydrous melts. We then compare the derived fitting parameters with Brillouin and Raman data. Importantly, 5 anhydrous melts were excluded from the comparison in Figure 4.3 (RhB, MSA and Str for the boson peak, and RhB, Teph and Trach for the Brillouin approach) as these were isolated to validate externally our approach together with all hydrous data. We find significant correlations between Brillouin (Figure 5.1 a)) and Raman (Figure 5.1 b)) data with the melt fragility m over the entire chemical space explored in our study. A linear correlation (Figure 5.1 a)) describes the relationship between the melt fragility m and the K/G ratio (R-squared = 0.93):

$$m = 43 (K/G) - 31 \quad (5.1)$$

The constants errors are 3 and 4 respectively. When volcanologically relevant (i.e. multicomponent) melts are considered, the SiO₂-rich calcalkaline rhyolites¹¹¹ and haplogranite HPG8 melts¹⁶⁶ exhibit the lowest K/G (~1.30) and m (22.5-28.8), the SiO₂-poor Foid sample¹⁶⁹ shows the highest K/G (1.86) and fragility (49.5), whereas samples with an intermediate SiO₂ content (Phon, And, Str, Bas)^{168,169} are in between. Literature data of simple systems (pure SiO₂ and GeO₂)^{23,173} further extend the correlation to lower values of both K/G and m . The anorthite and diopside samples²⁰ exhibit K/G equal to 1.81 and 1.90, respectively. Overall, our results agree with those of Novikov et al.²³ who showed a linear correlation between m and the K/G for simple glass-forming melts within

a large interval of m ($20 \lesssim m \lesssim 100$). We derived m of the multicomponent systems considered in this study and found that the Novikov et al.²³ model can predict the melt fragility m of strong systems, whereas a deviation is observed when more fragile systems are considered. For instance, we calculated (1.18) $m = 20$ for the strong GeO_2 and derived $m = 22.1$ with (5.1), and the literature²³ prediction is $m = 23.4$. For more fragile systems such as the Foid sample, (1.18) provides $m = 49.5$ and (5.1) $m = 49.7$, whereas the estimation from the literature²³ yields $m = 42$. The deviation can be attributed to:

- I. the substantially different (i.e. multicomponent) and more restricted (i.e. dominantly SiO_2 -bearing) compositional space explored in this study;
- II. the assumed η_∞ that here is $10^{-2.93}$ Pa s while in Novikov et al.²³ appears to be 10^{-4} Pa s.

Although these differences in the estimate of m may be dictated by the chemical domain and the strategy used to fit viscosity data (VFT and MYEGA equations and associated η_∞), our results (Figure 5.1 a), b)) confirm the literature observations^{23,24}.

Similar to BLS results, Figure 5.1 b) shows a simple correlation between the fragility and the BP position ω_{BP} . We find that the correlation between ω_{BP} and m can be empirically described via the following exponential function (R-squared = 0.94):

$$m = 1.7 \exp(\omega_{BP} / 28) + 14.97 \quad (5.2)$$

where 14.97 is the minimum possible m -value^{84,172} within the MYEGA formulation (1.18) here adopted (see Literature data paragraph for details), with the constants error = 4. With decreasing the melt fragility, the boson peak position shifts from about 48 cm^{-1} (pure SiO_2) to 90 cm^{-1} (Di sample). From a fundamental perspective, our BLS (Figure 5.1 a)) and RS (Figure 5.1 b)) results point out the dominant role of acoustic modes in the BP region (e.g. ref.^{69,173}).

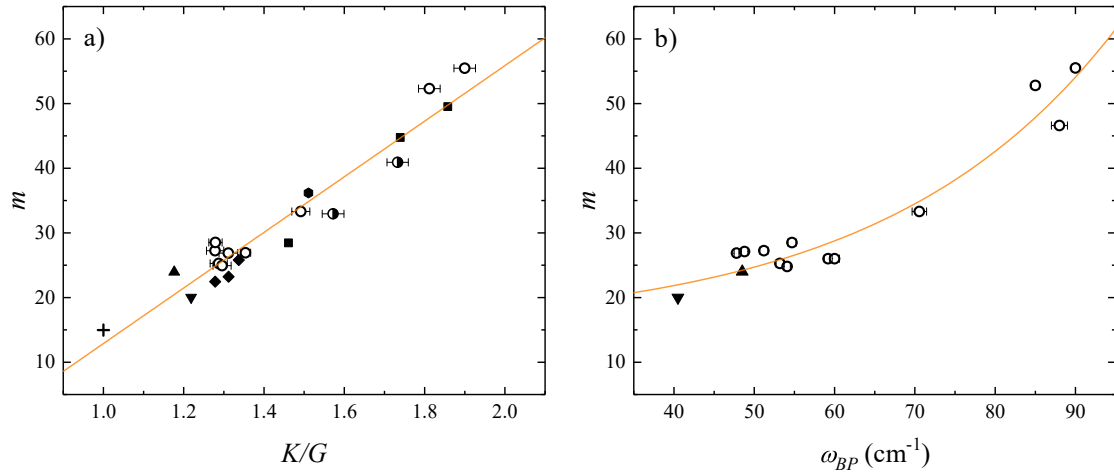


Figure 5.1 a) Relationship between the melt fragility m and the ratio of the bulk and shear moduli K/G of anhydrous samples. The m parameter is derived by fitting anhydrous melt viscosity from the literature with (1.18) assuming $\eta_{\infty} = 10^{-2.93}$ Pa s, whilst the K/G is calculated using (4.2) and Brillouin velocities from this study and the literature. The two half-colored symbols indicate samples (Str and MSA) for which viscosity data¹⁵³, used to derive m , and the Brillouin data from this study used to derive K/G , are derived from different samples (see Literature data paragraph for details). The orange line represents the linear fit of data (5.1). Samples used here are 7 rhyolites (Rh series), MSA, Str, DGG-1, An, Di, SiO₂ GeO₂, And, Bas, Phon, Foid, HPG8_Na05, HPG8_K05, HPG8_Li05 and the synthetic sample (see Literature data paragraph for references). b) Relationship between the melt fragility m and ω_{BP} position of anhydrous samples. The BP position is derived by fitting the low-frequency Raman spectra of glasses using a log-normal equation (see Methods paragraph for details). The orange line represents the exponential fit of data (5.2). Samples used here are 7 rhyolites (Rh series), DGG-1, An, Crd, Di, HO, SiO₂ and GeO₂. Chemical composition and source of data are listed in Table 4.2, respectively. Literature data in a) are: (square) Whittington et al.¹⁶⁹, (hexagon) Richet and Polian¹⁶⁸, (diamond) Hushur et al.¹⁶⁶, (solid upward triangle) Zanatta et al.¹⁷³, (solid downward triangles), Novikov et al.²³. Literature data in b) are: (solid upward triangle) Zanatta et al.¹⁷³, (solid downward triangle) Zanatta et al.⁷⁰.

Brillouin and Raman data suggest that the spectroscopic analysis enables the estimation of the melt fragility and therefore glasses can be used to estimate the viscosity of their parental melts, provided T_g is known. The glass transition temperature T_g , which is the temperature at which the viscosity is 10¹² Pa s, can be derived via DSC measurements using a small amount of glass (~10 mg) when subjected to a specific thermal treatment. Therefore, in order to retrieve the viscosity of melts from spectroscopic measurements of glasses, one needs to estimate m by either Brillouin or Raman

spectroscopy and measure T_g via DSC. The Figure 5.1 a) and b) illustrate the comparison between measured viscosity from the literature and our prediction with the MYEGA equation (1.18), assuming $\eta_\infty = 10^{-2.93}$ Pa s, using T_g listed in and m derived via Brillouin velocities (5.1) (Figure 5.2 a)) and Raman spectroscopy (5.2) (Figure 5.2 b)). The Brillouin and Raman models have a root-mean-square-error (RMSE) of 0.26 and 0.27 log units, respectively.

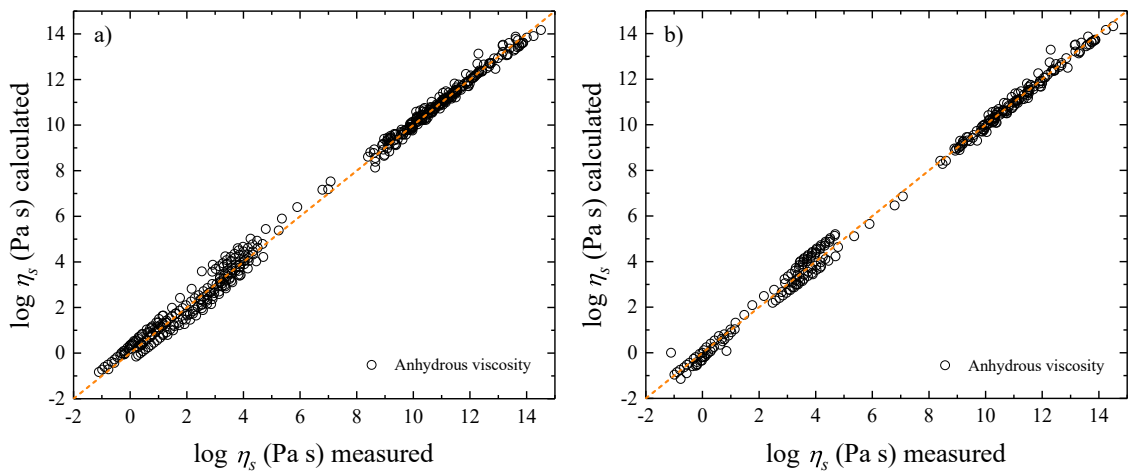


Figure 5.2 a) Comparison between anhydrous viscosity data ($N_{dry}=441$) from literature and MYEGA predictions ((1.18), where $\eta_\infty = 10^{-2.93}$ Pa s) using the melt fragility m derived by Brillouin data (Table 4.2) m via (5.1). b) Comparison between anhydrous viscosity data ($N_{dry}=288$) from literature and the model predictions (1.18) using the melt fragility m derived by ω_{BP} via (5.2).

Finally, we use an external dataset to validate our approach. We explored the largest possible chemical space of volcanologically-relevant glasses for which the viscosity and spectroscopic data are available for the same sample. We collected a set of anhydrous and hydrous melts whose viscosity was independently measured over ~ 14 orders of magnitudes, as well as Brillouin and Raman data of their parental glasses. The estimated viscosity $\eta_s(T)$ was calculated using (1.18) with $\eta_\infty = 10^{-2.93}$ Pa s, T_g from the literature (see Table 4.2), whereas the melt fragility m is Brillouin-derived, i.e. calculated using (5.1) and the K/G ratio obtained from the sound velocities measured by BLS, or Raman-derived, obtained via (5.2) and the BP position ω_{BP} measured from RS.

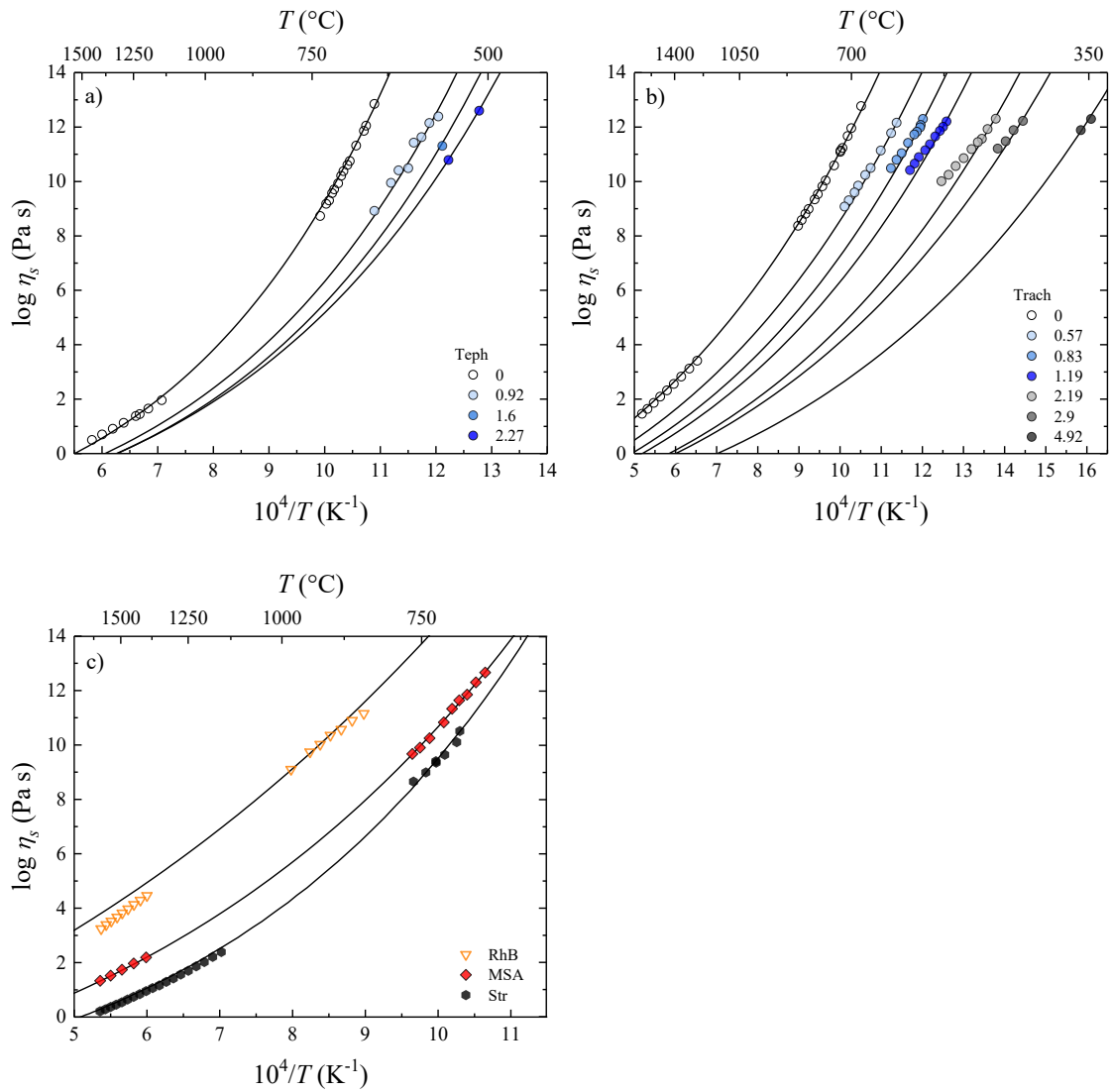


Figure 5.3 a) Measured (symbols) anhydrous and hydrous viscosity data for the tephrite (Teph)¹⁷⁵ and predictions (lines) using Brillouin velocities (Table 4.2). Numbers in the legend indicate the water content of samples in wt.%. b) Measured (symbols) anhydrous and hydrous viscosity data for the trachyte (Trach)¹¹² and predictions (lines) using Brillouin sound velocities (Table 4.2). Numbers in the legend indicate the water content of samples in wt.%. c) Measured (symbols) anhydrous viscosity data for the calcalkaline rhyolite RhB¹¹¹, MSA andesite^{152,153} and Str basalt^{154,155}. Lines are predictions using the boson peak position (Table 4.2) derived by Raman spectroscopy.

Brillouin data (Table 4.2) of anhydrous and hydrous systems (Bas, Teph, Foid, Trach, Phon, And, RhB) were used to validate our approach using viscosity data from the literature ($N_{validation} = 198$)^{17,111,112,170,171,175}. Furthermore, we used the $K/G = 1.16$ ratio for the HPFS[®] 7980 fused silica (SiO_2 , OH^- content between 800 and 1000 ppm) to

calculate the viscosity at 1585 °C, which corresponds¹⁷⁶ to the softening point of the sample ($\eta_s = 10^{6.6}$ Pa s). In Figure 5.2 a) and b) we report two examples for the relatively SiO₂-poor and SiO₂-rich volcanic Teph and Trach samples, respectively. Moreover, Figure 5.2c) shows the comparison between anhydrous measured viscosity ($N_{validation} = 57$) and Raman-based predictions using the BP position of the basalt (Str, viscosity data from ref.^{154,155}), andesite (MSA; viscosity data from ref.¹⁵³) and rhyolite (RhB; viscosity data from ref.¹¹¹) glasses. Notably, the inspection of the results for anhydrous viscosities in Figure 5.3 (a,b,c,) demonstrates that our approach allows the accurate low- and especially the high-temperature projection (lines) of viscosity as demonstrated by the remarkable prediction of the water-free viscosity in the low-viscosity regime ($\eta_s < 10^4$ Pa s). Here we observe that the BLS approach (Figure 5.3 a) and b)) perform slightly better than the RS one (Figure 5.3 c)). Concerning hydrous samples, and based on BLS data from ref.¹⁶⁹, Figure 5.3 a) shows that we can successfully predict the measured viscosity¹⁷⁵ as a function of temperature for the SiO₂-poor tephritic glasses (Teph) characterized by 0.92, 1.6, and 2.27 wt.% of H₂O. We include in our comparison (Figure 5.3 a)) the prediction of $\eta_s(T)$ for those samples whose viscosity did not suggest crystallization and/or water loss during the measurement as discussed in ref.¹⁷⁵. We further validate our Brillouin-based approach with hydrous SiO₂-rich trachyte (Trach) melts for which both viscosity and Brillouin data are known^{112,169}. The Figure 5.3 b) illustrates that our approach accurately predicts the anhydrous viscosity over ~12 orders of magnitudes, similarly to the Teph anhydrous sample (Figure 5.3 a)). However, a careful inspection of the results reveals that a slightly different picture is depicted.

Our approach can indeed accurately predict the measured viscosity of relatively water-poor samples (H₂O \leq 0.83 wt.%) within the interval of $10^9 < \eta_s < 10^{12}$ Pa s. For the water-rich samples (H₂O \geq 1.19 wt.%), the accurate prediction is limited to $\eta_s \sim 10^{11}$ Pa s because at lower viscosities, our approach increasingly underestimates the viscosity with increasing temperature. This is due to the opposite behavior observed for the melt fragility as a function of water content when our m estimates are compared with those provided by the literature¹¹², calculated using viscosity data and the VFT description of $\eta_s(T)$ in ref.¹¹². The Brillouin-derived m increases from 30.9 (H₂O = 0 wt.%) to 36.8 (H₂O = 4.92 wt.%), whereas the literature-derived m decreases with H₂O content from 32.9 to 26.3. A separate study is required to experimentally investigate this aspect through, for

instance, the combination of Raman spectroscopy and TEM imaging^{15,177,178} to investigate glasses before and after viscosity measurements, in ref.²⁷ is also provided a discussion on fragility behavior with H₂O for trachytic melts based on glass structure and thermodynamics concepts like configurational heat capacity.

However, there are no known physically significant evidence of the mechanism regulating the BP behavior in these complex systems. The ω_{BP} shift of chemically modified silicates melts and glasses is often linked to microscopic modifications where the local disorder no longer holds the role of the mean distributing the elastic properties suggesting a medium far from being homogeneous^{179,180}.

The melt fragility is a kinetic property of glass-forming melts that positively correlates with several chemical and thermodynamic properties of glasses^{39,181–186} and as stated before, materials with a well-pronounced BP fall into the category of strong glasses while those with a weak BP are mostly fragile²⁴. However, there is only little evidence in literature linking directly the fragility to the boson peak position¹²³. Even though there are no direct experimental relationship among ω_{BP} , T_g and m , relationships between chemistry, structure and possibly viscosity are often related to a chemically-induced distribution of rotational motion of the silica tetrahedra rotations recorded by ω_{BP} ^{187,188} and eventually influenced by localized vibrations of other cationic species (i.e. alkaline earths) with the NBO¹⁸⁹ or to a different redistribution in the LRO of localized elastic nano-heterogeneity $R(\omega)$ ^{190–192}. An alternative interpretation of the BP suggests a direct correlation with the accumulation of acoustic modes in the proximity of the pseudo-Brillouin zone boundary (see ref.⁶⁹ and literature therein) and this may explain the compatibility of our data. Indeed, sound wave velocities and BP frequency positively correlates with composition (Figure 4.2). However, this conjecture may imply a straightforward relation of the DOS of the glass to that of its equivalent crystal following the Debye model toward the Van Hove singularity of the equivalent crystals. Unfortunately, in our case the description provided by Chumakov et al.⁶⁹ for the BP can only be partially adopted since there is no way to Figure out the properties of the crystalline analog of a magma, but a rescaling procedure derived from this idea can qualitatively explain the BP shift and its relation with the acoustic modes represented by ω_D .

The elastic medium can be represented by the Debye frequency ω_D introduced in section 1.2 and described by equation (1.11) and (1.13). Its evolution can be considered both in terms of external parameters (i.e. pressure or temperature) and internal, which mainly account on chemical changes and density ρ . However, this approach nicely provides a scaling law only in few cases, whereas does not work in many other systems (see ref.¹⁷³ and literature therein). In order to clearly depict where the continuum medium properties can represent the BP evolution in our system, we calculate the ω_D of the calcalkaline series defined in the chemical domain represented by the rhyolite (RhE) and basalt (Str). This magmatic series can be considered as an elastic medium chemically evolving in the chemical interval defined by the above end-members, which also account for chemically-induced densification. All the frequency data (reported in Table 5.3) were normalized to the RhE rhyolitic sample showing the highest T_g and the lowest m of the analyzed magmatic series.

	RhA	RhB	RhD	RhE	RhJ	MSA	Str
ρ (g cm ⁻³)	2.32 (1)	2.28 (1)	2.29 (1)	2.31 (1)	2.40 (1)	2.60 (1)	2.68 (1)
v_T (m s ⁻¹)	3604 (14)	3610 (8)	3549 (8)	3550 (14)	3581 (7)	3608 (12)	3569 (12)
v_L (m s ⁻¹)	5835 (12)	5869 (14)	5772 (20)	5773 (11)	5870 (8)	6150 (16)	6249 (17)
ω_D (THz)	10.1 (1)	10.0 (1)	9.8 (1)	9.8 (1)	10.1 (1)	10.4 (1)	11.1 (1)

Table 5.3 Density (ρ), transversal and longitudinal sound velocities v_T and v_L and Debye frequency (ω_D) obtained as discussed in the text.

In order to check whether the shift of the BP can be totally ascribed to changes in the elastic constants, we can compare the dependence of ω_{BP} and ω_D on the same plot, Figure 5.3. Orange triangles represent the elastic continuum transformation (the Debye frequency ω_D) obtained by BLS and density data, in function of both T_g and m , whilst ω_{BP} is represented by black triangles. The T_g dependence of ω_{BP} and ω_D is exponential decay-like whilst the m dependence, although scattered, suggests a roughly growing trend with one order of magnitude different. This result is in line with study in strong densified glasses (SiO₂¹⁷³ and GeO₂¹⁹³) and polymeric glasses¹⁹⁴.

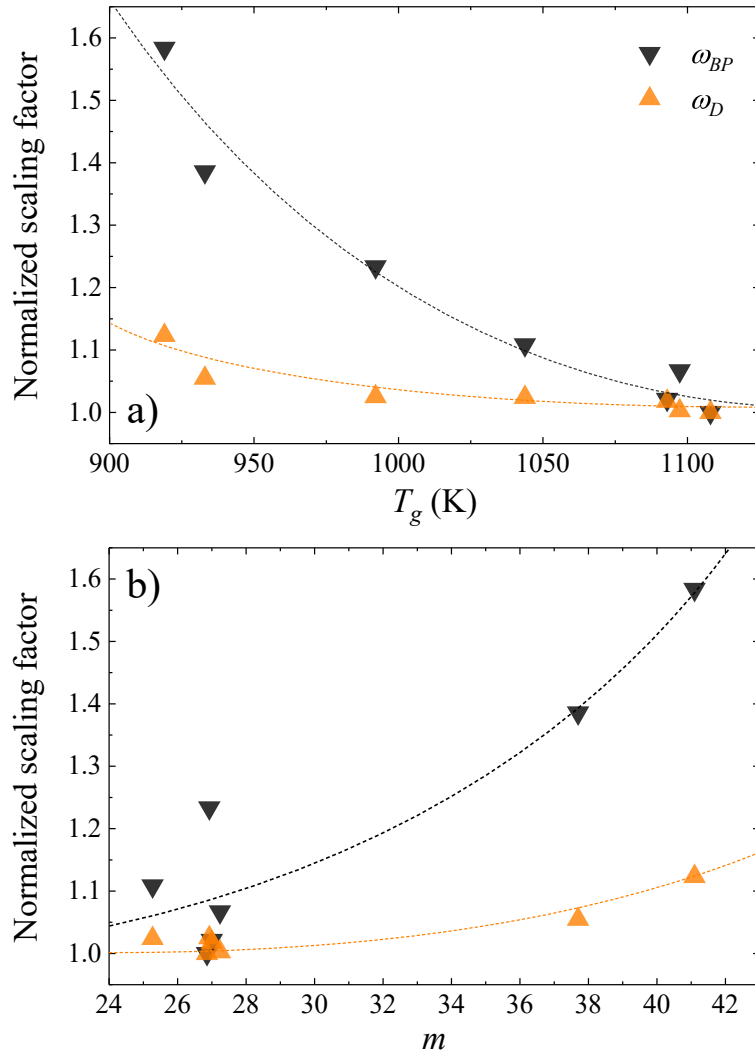


Figure 5.4 Comparison between the ω_{BP} and ω_D black triangles correspond to the Boson Peak frequency obtained from Raman spectra and orange triangles to the Debye frequency calculated using BLS sound velocities from (1.13) in function of a) glass transition temperature T_g , (curve fit R-square $_{BP}$ = 0.874 and R-square $_D$ = 0.947) and b) to fragility m , (curve fit R-square $_{BP}$ = 0.961 and R-square $_D$ = 0.828).

The evolution of the elastic medium (ω_D), although slightly, shows also an indirect relation with the glass structure in terms of polymerization degree, since empirically derived T_g and m are strongly correlated with composition^{195–197}.

This result clearly demonstrates that the elastic medium transformations cannot totally account for the BP shift. Indeed, the boson peak shift is faster than the Debye modifications in function of m , T_g and composition. Thus, we confirm that the scaling of

the BP with the continuum elastic medium properties, represented by the Debye frequency, is not a universal feature of disordered materials¹⁷³. Anyway, our inferences are absolutely speculative, but this hypothesis could, however, justify future studies on behavior of the excess VDOS (represented by the BP) and the role of the chemically-induced disorder of complex multicomponent system on the anomalous behavior of sound waves propagation.

Figure 5.4 sums up the result of the external validation of our Brillouin- and Raman-based approach to derive $\eta_s(T)$ of anhydrous and hydrous melts over ~ 14 decades using 277 viscosity data (RhB, Bas, Str, And, MSA, Teph, Foid, Trach, Phon). Samples are coloured according to water content and the largest deviation between measured and calculated viscosity is observed for the Phon melts with $\text{H}_2\text{O} > 1$ wt.%. For the And, Bas, Foid samples the Brillouin-derived m varied slightly (Table 4.2) with water content. All in all, our BLS and RS-based approaches can predict the viscosity of anhydrous and hydrous volcanologically-relevant melt with a RMSE of 0.24 log units (BLS) and 0.30 log units (RS). Finally, we stress that glasses used and considered here for deriving BLS and RS data were subjected to virtually unknown and diverse cooling rates. Yet, the success of our validation suggests that within the chemical space here explored, the cooling rate typical of laboratories does not significantly affect the relationship between K/G and ω_{BP} of glasses and the melt fragility m of its parental melt. This is in line with observations from 1) Whittington et al.¹⁶⁹ who subjected unrelaxed and relaxed glasses to BLS (see Brillouin spectroscopy paragraph for more details) and 2) McIntosh et al.¹⁹⁸ who studied the ω_{BP} of alkali silicate glasses. Both studies found little difference in the measured vibrational properties between as quenched and annealed glasses. However, a more robust dataset is needed to investigate this carefully and we are confident that our study will stimulate new studies in this direction.

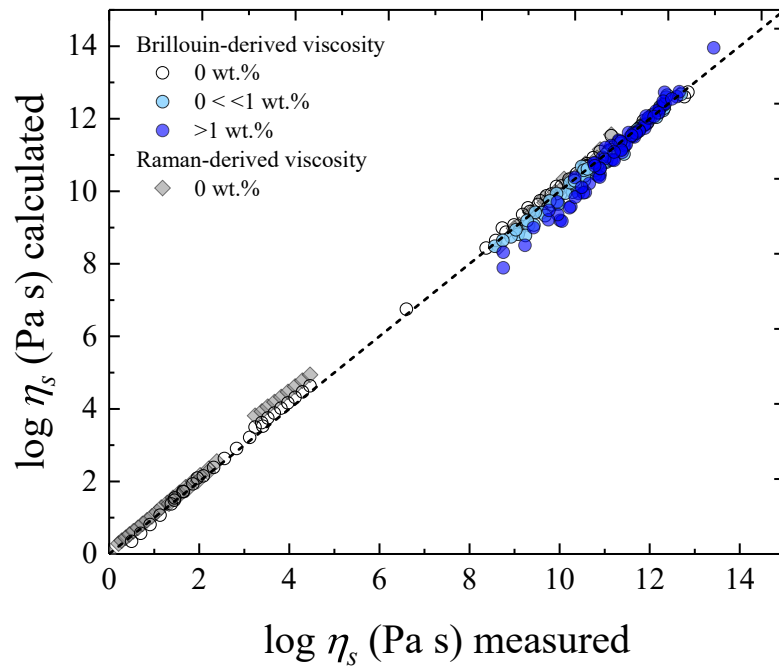


Figure 5.5 Comparison between measured values of viscosity with Brillouin-derived (circles) and Raman-derived (empty diamonds) values. For Brillouin-derived viscosity, both anhydrous (empty circles) and hydrous (coloured circles) data are reported. Hydrous data are grouped according to their water content (< 1 and > 1 wt.%). The largest deviation between measured and calculated values is observed for samples characterized by both the highest water content and the lowest measured viscosity (see text for details). For Raman-derived data only anhydrous viscosity is available.

6. CONCLUSION

Our study shows and underpins the significance of Raman spectroscopy in the understanding of the chemical-induced modifications of both volcanic and technical glasses providing.

Given the well-known correlation of m with the elastic properties of glasses and the remarks on the amplitude of the boson peak^{22,24}, we have introduced an alternative approach to derive the viscosity of volcanic and technical glass-forming melts without the need of viscosity measurements. Our approach is built-up on the basis of the MYEGA formulation and consists in a crossed strategy based on the assumption that ω_{BP} and K/G embed m . These two parameters are obtained by exploiting the complementarity between Raman and Brillouin spectroscopy, whilst DSC measurements allows derivation of T_g .

Our empirical model was trained and validated at volcanologically relevant conditions using two large and non-overlapping anhydrous and hydrous datasets, encompassing virtually the entire magmatism on Earth. Our results extend the possibility of application of our approach with small amount of sample (~10 mg of glass) using standard laboratory equipment and ensures cross-validation of results.

In the frame of the excess VDOS, we have provided additional information that supporting the link between acoustic modes and its excess in the low-frequency domain, which can be insightful about the long-debated nature of the boson peak. The observed peak shift has been also compared to the modification of the elastic medium described by the Debye frequency ω_D showing a strong non-Debye behavior as the glass depolymerizes, at least in a calcalkaline series. This may be also thoughtful in the explanations of the physico-chemical mechanisms behind the BP, at least in its evolution in such complex multicomponent glass-forming systems.

In any case, many aspects of this work require further investigations.

APPENDIX I: Effect of $\text{Fe}^{3+}/\text{Fe}_{(\text{tot})}$ in Pantelleritic glasses

One of the major elements of magmas is iron, which is characterized by a dual role, depending on its valence state: network former (NF) when Fe^{3+} and network modifier (NM) when Fe^{2+} . Strongly affected by particular condition such as melt composition, temperature and oxygen fugacity, the oxidized iron Fe^{3+} could span a range of coordinated structure from 4-fold to 6-fold and deeply influences the melt structure, thermal properties and rheology^{199–208}. Thus, the parametrization of the $\text{Fe}^{3+}/\text{Fe}_{\text{tot}}$ ratio is central in determining the chemical-dependence of the silicate melt properties. To this aim, geoscientists exploit Raman spectroscopy^{206,207,209}, as an indispensable tool for fast and thorough investigations of solids. The structural information are mainly located in specific Raman bands^{209–212}. In this appendix we extend the studies reported in ref.²⁰⁶ and ref.²⁰⁷, showing new results from a low-frequency Raman study on a set of peralkaline iron-rich rhyolites named pantellerites. These volcanic glasses are characterized by an extremely high iron content (~ 9 wt. %) and they are named pantellerite. By varying the $\text{Fe}^{3+}/\text{Fe}_{\text{tot}}$ ratio, we observe a shift of the BP towards higher frequencies as the ferric iron content increases. Conversely, as the heat flow peak (T_g^{peak}) shift towards lower temperatures, the BP maximum results more and more suppressed. Moreover, we show the existence of the scaling law for the BP, at least for $\text{Fe}^{3+}/\text{Fe}_{\text{tot}}$ ratio ~ 0.40 , below this value the scaling does not hold any more and the structure seems undergoes deep modifications.

Starting materials

The starting material consists of anhydrous iron-rich rhyolitic glasses named pantellerites, previously synthesized and characterized in the study²⁰⁶. Since chemistry, Fe^{3+}/Fe_{tot} and T_g^{peak} are crucial parameters for this study they are summarized in Table A.I. 1. The samples consist on 7 glasses with different Fe^{3+}/Fe_{tot} ratios ranging between 0.24 and 0.74, with an agpaite index $[(Na_2O+K_2O)/Al_2O_3 \text{ mol \%}]$ of around 1.3. The SiO_2 content varies between $\sim 72-75 \text{ wt\%}$, $\sim 7-9 \text{ wt\% } FeO_{tot}$ $\sim 9 \text{ wt\% } Al_2O_3$ and the alkalis (Na_2O+K_2O) between ~ 8 and 9 wt\% , whilst the glass transition temperature has been estimated to the T_g^{peak} by DSC measurements, described in study²⁰⁷.

	FSP2	FSP3	FSP4	FSP6	FSP7	FSP8	FSP9
SiO ₂	71.89	72.94	71.93	73.11	73.44	74.62	74.24
TiO ₂	0.43	0.42	0.43	0.43	0.43	0.45	0.44
Al ₂ O ₃	8.78	8.92	8.97	8.97	9.05	9.05	9.01
Fe ₂ O ₃	7.24	5.56	6.13	3.71	3.00	2.05	1.88
FeO	2.26	3.55	3.42	5.00	5.01	5.32	5.35
MnO	0.35	0.37	0.37	0.37	0.35	0.38	0.36
MgO	0.16	0.17	0.17	0.17	0.17	0.18	0.17
CaO	0.43	0.44	0.46	0.47	0.40	0.45	0.47
Na ₂ O	4.37	4.46	4.72	4.55	4.08	4.06	4.19
K ₂ O	4.01	4.10	4.18	4.18	3.99	4.05	4.14
Fe ³⁺ /Fe _{tot}	0.74	0.58	0.62	0.40	0.35	0.26	0.24
T_g^{peak} (K)	952.2	946.2	942.4	933.1	932.4	-	925.6

Table A.I. 1 Chemical composition in wt% and Fe^{3+}/Fe_{tot} index, obtained by wet chemistry titration and the glass transition temperature also reported. See details in ²⁰⁷.

The HH polarized Raman spectra acquired on samples with $\text{Fe}^{3+}/\text{Fe}_{\text{tot}}$ ranging between 0.24 and 0.74 and a SiO_2 content ranging between ~ 71 and 74 wt. % whilst the other component remains almost fixed are shown in Figure A.I. 1. Generally, some features hold the same characteristic, in particular the broad band at 460 cm^{-1} suggesting that the Si-O-Si bond angle is not apparently affected by the subtle chemical changes²¹³. Indeed its related to rocking and symmetric bending motions of bridging oxygen is typical of strongly polymerized silicate glasses^{131,132}. However, some slight differences can be appreciated on the component at $\sim 490\text{ cm}^{-1}$ and the shoulder at 600 cm^{-1} . These features have been associated to the symmetric bending vibrations of bridging oxygen in 4- and 3-membered rings¹³³. In particular, the shoulder at $\sim 600\text{ cm}^{-1}$ decreases as the $\text{Fe}^{3+}/\text{Fe}_{\text{tot}}$ ratio increases. The 800 cm^{-1} band, ascribed to the three-fold degenerate “rigid cage” vibrational mode of SiO_2 units¹³⁵ does not reveal appreciable changes or shift. Since this band seems insensitive to compositional changes, its integrated area has been used to normalize both the HH and HV spectra. By contrast, moving toward the high frequency region ($850\text{-}1250\text{ cm}^{-1}$), the spectra significantly change. In particular, as the $\text{Fe}^{3+}/\text{Fe}_{\text{tot}}$ decreases, the centroid band shifts toward higher frequency (i.e. from $\sim 970\text{ cm}^{-1}$ for the FSP2 with $\text{Fe}^{3+}/\text{Fe}_{\text{tot}} = 0.74$; to $\sim 1100\text{ cm}^{-1}$ for FSP9 with $\text{Fe}^{3+}/\text{Fe}_{\text{tot}} = 0.24$). This spectral region is usually dominated by the stretching vibrations of both tetrahedral SiO_4 and AlO_4 units (i.e. Q^n species), and by the Si-O stretching vibrations in SiO_4 tetrahedra connected to one Al polyhedron originating the 1100 cm^{-1} band²¹³.

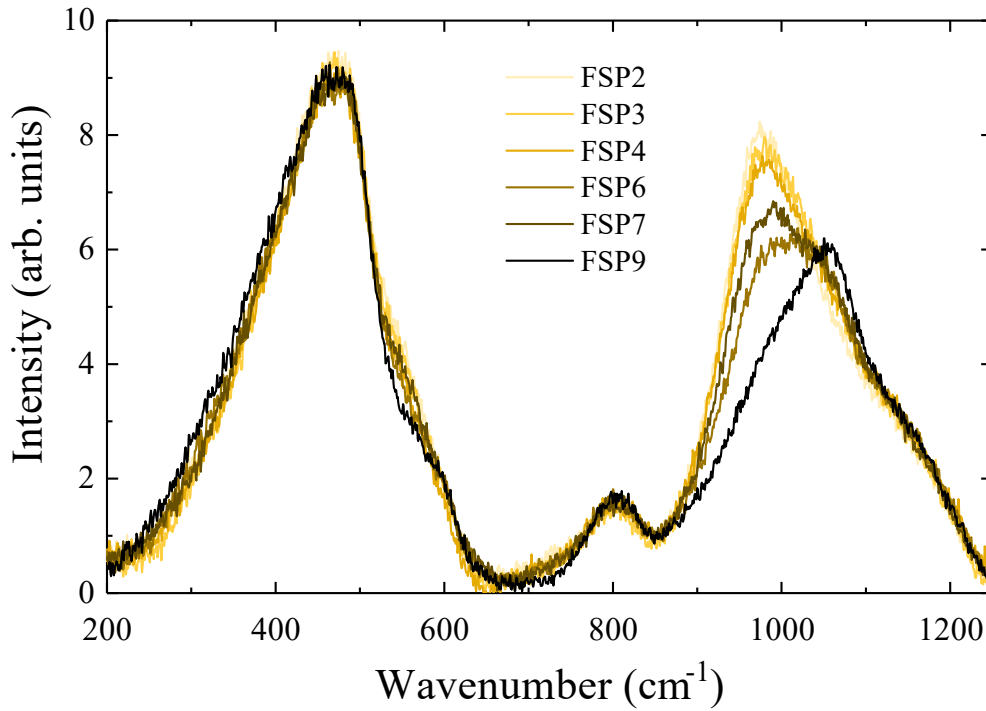


Figure A.I. 1 Raman spectra acquired in HH polarization and corrected after a quadratic baseline. The spectra are normalized to the 800 cm^{-1} peak.

Discussion and conclusions

The low-frequency Raman spectra analysis has been conducted according the previous sections, by considering the intensity I^{obs} , proportional to the density of states $g(\omega)$. Considered a Stokes process the intensity follows the relation (2.10) and dividing by $[n(\omega, T) + 1]$ (here $n(\omega, T)$ is the Bose-Einstein population factor) and frequency (ω), we obtain the reduced Raman intensity¹²⁸ $I^{red}(\omega)$, which is proportional to the reduced density of vibrational states $g(\omega)/\omega^2$ as according to (2.11). The reduced spectra are plotted in Figure A.I. 2 and for a suitable comparison they were normalized to the integrated area of the 800 cm^{-1} band (as shown in the inset in Figure A.I. 2). The BP position has been carefully determined by fitting its asymmetric shape to a log-normal

function¹⁴⁶. The BP position shift from $\sim 48 \text{ cm}^{-1}$ to $\sim 54 \text{ cm}^{-1}$ while its maximum becomes more and more suppressed reducing its intensity (I^{red}) of $\sim 40\%$.

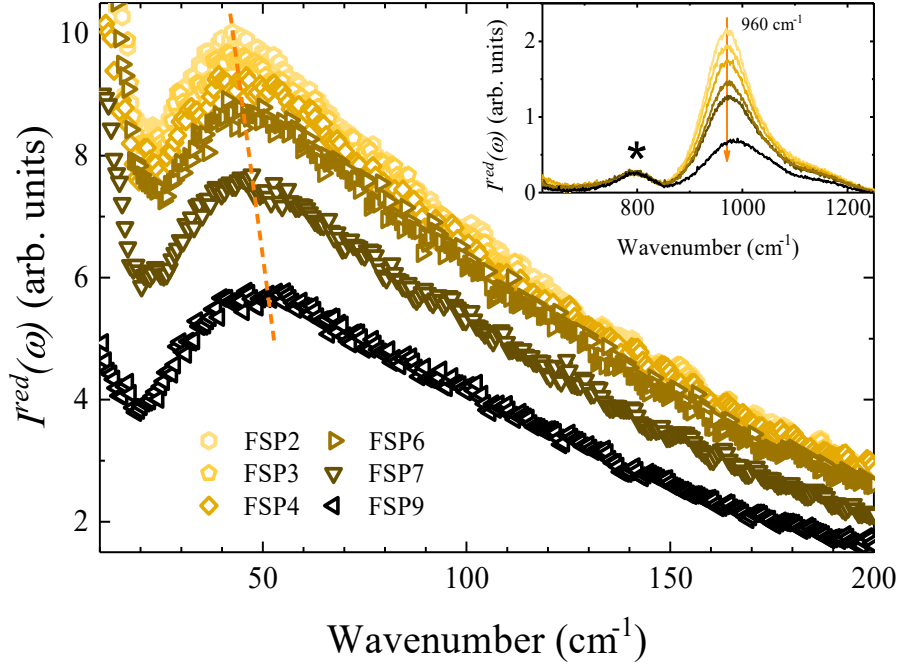


Figure A.I. 2 Crossed (HV) polarization and reduced Raman spectra in the low frequency region of samples with increasing $\text{Fe}^{3+}/\text{Fe}_{\text{tot}}$ ratio. The orange dashed line is an eye-guideline. The spectra normalized to the integrated area of the 800 cm^{-1} band is shown in the inset.

We further analyze the reduced spectra by considering their rescaled frequency $\nu = \omega/\omega_S$, and by performing the variable transformation $g(\nu)d\nu = g(\omega)d\omega$, thereby assuming $C(\omega) \sim \omega$ in the BP region.

The squeezed spectra with varying $\text{Fe}^{3+}/\text{Fe}_{\text{tot}}$ are plotted in Figure A.I. 3 and if we choose ω_S to get the same peak intensity, we obtain different behaviors. In the low frequency region below $\sim 20 \text{ cm}^{-1}$, the QES tail exhibit same contributions discussed previously. Moving forward, the right flank of the squeezed spectra results more and more tilted inward as the $\text{Fe}^{3+}/\text{Fe}_{\text{tot}}$ ratio decreases. Additionally, as the tilting progresses the squeezed maximum results slightly shifted backward. Only samples with $\text{Fe}_{3+}/\text{Fe}_{\text{tot}}$ ranging between 0.74 and 0.40 collapse in the same master curve, while for $\text{Fe}_{3+}/\text{Fe}_{\text{tot}} \leq 0.35$ the scaling gradually drops.

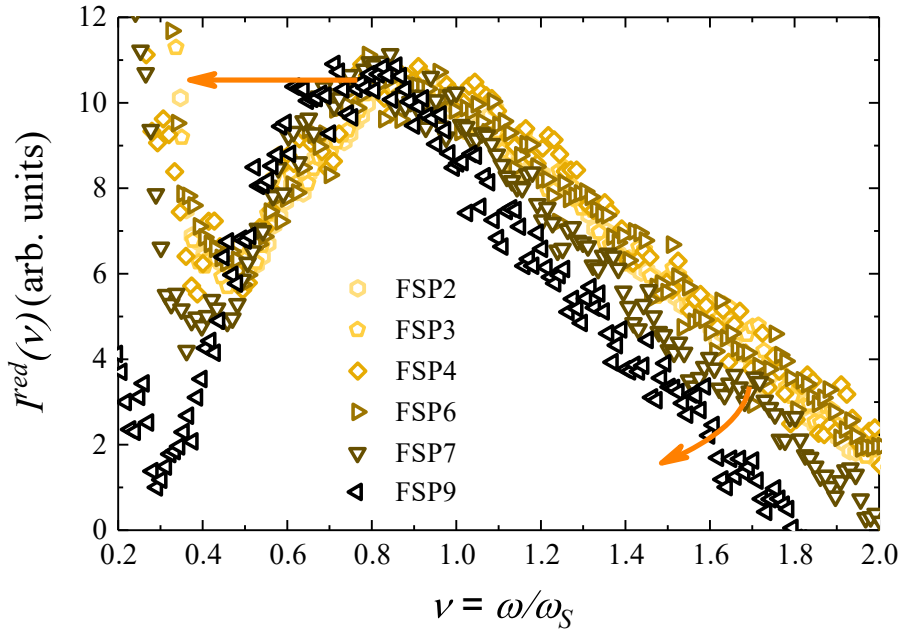


Figure A.I. 3 Master curve of the boson peak, obtained as discussed in the text. The orange arrows emphasize the tilting of the right flank and the backward shift of its maximum.

Among the different models (XANES and EXAFS) data suggest that in those systems Fe^{3+} is four-fold coordinated with a shorter Fe-O bond length with respect to Fe^{2+} (four- five-coordinated). This therefore, results in higher viscosity at more oxidized conditions due to the higher polymerization degree of the system and Fe-O bond strength. For the most reduced condition, the glass transition temperature does not decrease as one would expect by looking at the trend at more oxidized conditions. Thus, the increasing three-dimensional network units follows from the increasing polymerization of the structure by adding Fe^{3+} which may induce a negative shift of the BP as reported in Figure A.I. 4 a). Thus, the ω_{BP} negatively correlates with polymerization of the system. An equivalent trend is observed between the glass transition temperature peak (T_g^{peak}) and ω_{BP} Figure A.I. 4 b). This behavior suggests again a clear relationship between the yet observed polymerization of the glass structure (i.e. retrieved by adopting the band

deconvolution of the high-frequency spectral region of both the same glasses and similar systems^{102,207}) and the ω_{BP} .

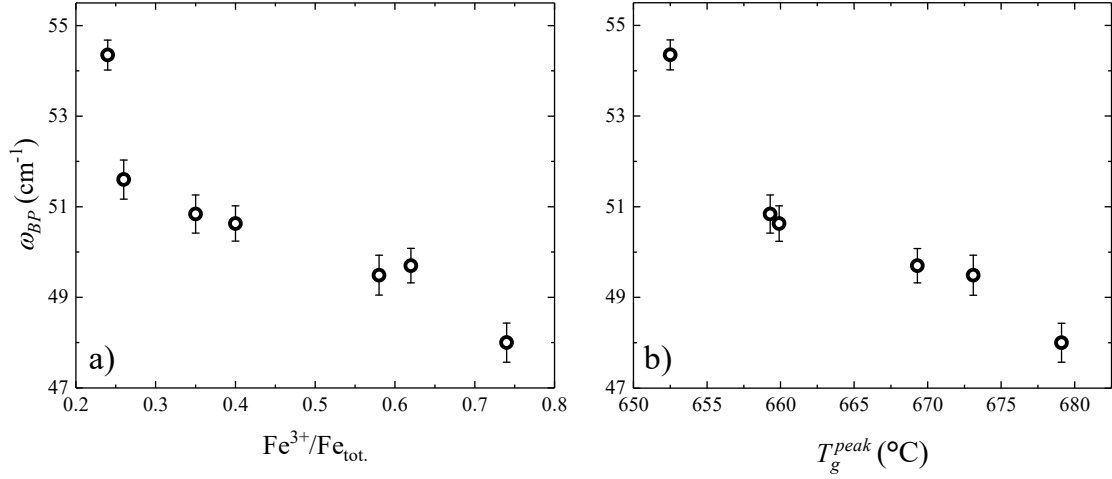


Figure A.I. 4 Relationships between the BP position ω_{BP} and a) the $\text{Fe}^{3+}/\text{Fe}_{\text{tot}}$. b) the glass transition temperature peak.

To conclude, the boson peak of the pantelleritic system shifts to higher frequency as the $\text{Fe}^{3+}/\text{Fe}_{\text{tot}}$ decreases through a depolymerizing structure. The same trend observed in the T_g^{peak} supports the hypothesis formulated in chapter 6 and 7 and represents a more general result. However, the values of the glass transition temperature are largely different to that of the calcalkaline rhyolites compared to their ω_{BP} for instance.

The scaling of the boson peak, which results in an inflexion of the high frequency tail, may provide a different way to analyze the structural transformation of the medium.

APPENDIX II: Effect of Na-K mixing in Basaltic glasses

Glasses are nowadays of pivotal relevance in an ever-growing variety of applications^{2,4,214}, thus understanding the relation between composition, structure, and physico-chemical is a crucial scientific challenge²¹⁵. In nature, glasses are mostly formed during the rapid cooling of magmatic liquids⁵. Magmatism represents the most impressive and spectacular manifestation of Earth's activity, often culminating in volcanic eruptions. The so-obtained igneous rocks represent the quasi-total composition of the Earth crust and about 70% of them consists of basalts resulting from the quenching of fluid melts characterized by low silica ($\text{SiO}_2 \sim 50$ wt.%) and high magnesium and iron oxides.

The abundance of basaltic rocks, as well as their properties, makes them very attractive as raw material for a sustainable economy. In fact, basalts are largely²¹⁶ converted into glasses and glass-ceramics in different technical fields: vitrified ceramics, textile fibers, rebars, geo-grids, and insulators^{217–221}. However, basalts applications are boosted by the possibility of controlling properties such as strength, corrosion, temperature resistance, melt viscosity, surface tension, density, and crystallization tendency. These are typically evaluated through chemical indexes like the acidity (M_a) and viscosity modulus (M_v). For instance, continuous basalt fibers (CBF) are typically manufactured using basalts possessing $3 \leq M_a \leq 6$ and $2 \leq M_v \leq 3$ ²²².

To unravel the structural properties of silicate glasses, both geoscientists and industrial scientists have exploited an extensive variety of spectroscopic techniques^{223–225}. Among them, Raman spectroscopy has emerged as one of the most powerful ones as it allows accurate non-invasive investigations of both structural and chemical modifications in solids^{131,152,226–229}. Generally, the analysis of the Raman spectrum of a given anhydrous glass is performed by probing the scattered light from 100-150 cm^{-1} , mainly due to instrumental limitations. Structural insights are mainly inferred from the deconvolution of the Q^n species where n is the number of bridging oxygen atoms in a tetrahedron (T) whose apical oxygens are coordinated by a network former (NF)^{209,210,212}.

Here we characterize four dry basaltic glasses, showing the effect of Na-K mixing on the glass transition temperature (T_g), the resulting structure and the dynamical

properties such as the BP, which are promising candidates for CBF production. The composition of our samples mimic the overall percentage distribution of the chemical constituents of basalts on Earth²³⁰ exploring an M_a -range ($4.1 \leq M_a \leq 4.8$) which has identified optimal for CBF manufacturing. K_2O - N_2O substitution was achieved by a doping-like process, which is largely exploited also for the production of alumina or rare-earth-doped silica fibers¹⁹¹. As the K_2O replaces the Na_2O , calorimetric data show an increase of the glass transition temperature whereas Raman spectra show a marginal structural rearrangement in terms of the Q^n species and a significant upward shift of the BP that decrease its intensity. Finally, we show the existence of a scaling law for the BP these basaltic glasses. This further shows that the N_2O - K_2O replacement in the explored M_a -range does not cause a strong reorganization of the structure but only and continuous modification of the vibrational properties in the BP range.

Glass synthesis

Four basalt glasses were obtained by melting mixtures of Na_2CO_3 , K_2CO_3 , $CaCO_3$, MgO , Mn_3O_4 , Fe_2O_3 , $(NH_4)H_2PO_4$, Al_2O_3 , TiO_2 , and SiO_2 (powders from Sigma-Aldrich). The powders were mixed in glass bottles and then melted in covered Pt crucibles to avoid contamination. The melts were dwelled for two hours at 1773 K. The samples were quenched in air by casting them onto a copper plate. The glasses were then crushed in an agate mortar and re-melted for further homogenization. Finally, the samples were annealed at temperatures at T_g for 30 min to relax the structure (the T_g was estimated by using the model of Giordano et al.²³¹ and was found ~ 920 K) and cooled down at 2 K min^{-1} . Table A.II. 1 reports the average composition of the four basalts as measured through the electron microprobe analyzer (EMPA) JEOL JXA-8900RL. The measurements were carried out at 15 kV acceleration voltage by probing 10 points of each glass with precision within 4.5% for all the elements. Table A.II. 1 also reports their acidity modulus ($M_a = (SiO_2 + Al_2O_3) / (CaO + MgO)$, where the oxides composition is expressed in wt %), the NBO/T value expressed as $\sum_{i=1}^i (M^{n+}_i)/T$, where M represent the NM cation. Additionally, the molar ratio between K_2O and the total alkali load is also reported, namely $K\#$, which is calculated in mol basis as $K\# = K_2O / (K_2O + Na_2O)$.

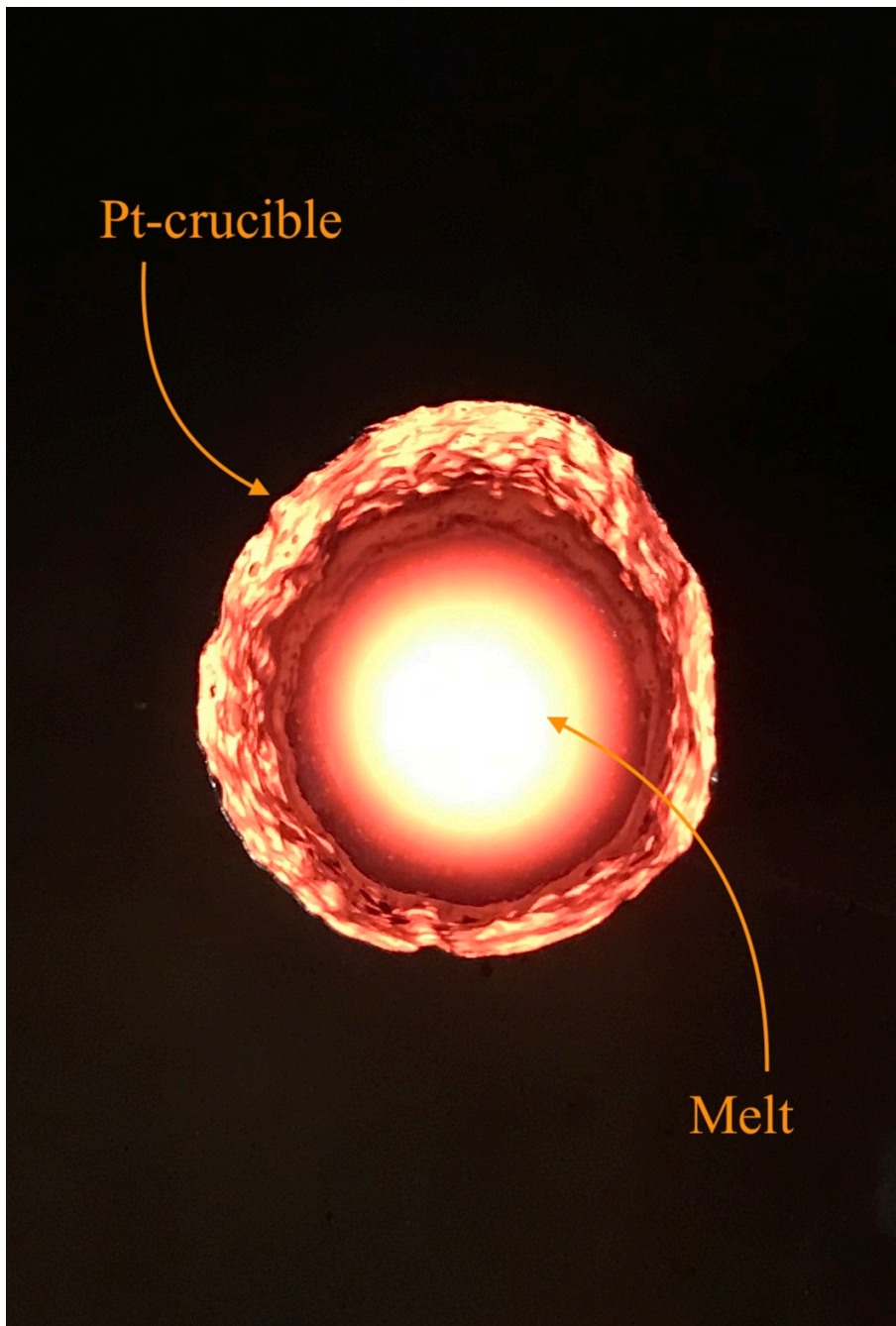


Figure A.II. 1 Photo of BN melt contained in a Pt crucible used for the different fusions. Photo taken on 11/9/2020 at university of Verona.

T_g was evaluated by dilatometric tests employing a Linseis L75 horizontal dilatometer equipped with a fused silica tube/piston on glass fragments 16 – 19 mm long and with a cross-section between 10 and 20 mm². The measurements were carried out at 5 K min⁻¹ in static air atmosphere and the actual sample temperature was measured using an s-thermocouple contacting the sample surface. The load applied by the dilatometer piston onto the sample was 250 mN. The glass transition temperature was evaluated by the tangent method: the tangents to the dilatometric plots (Figure A.II. 2) were identified before and after the glass transition, their intersection defined the T_g . Each measurement was repeated 5 times, the standard deviation was in all the cases below 1.3 K. The different values of T_g are reported in Table A.II. 1. Before dilatometry, the samples were annealed at 923 K for 1 h and cooled at 5 K min⁻¹ to avoid glass relaxation phenomena at temperatures approaching the T_g .

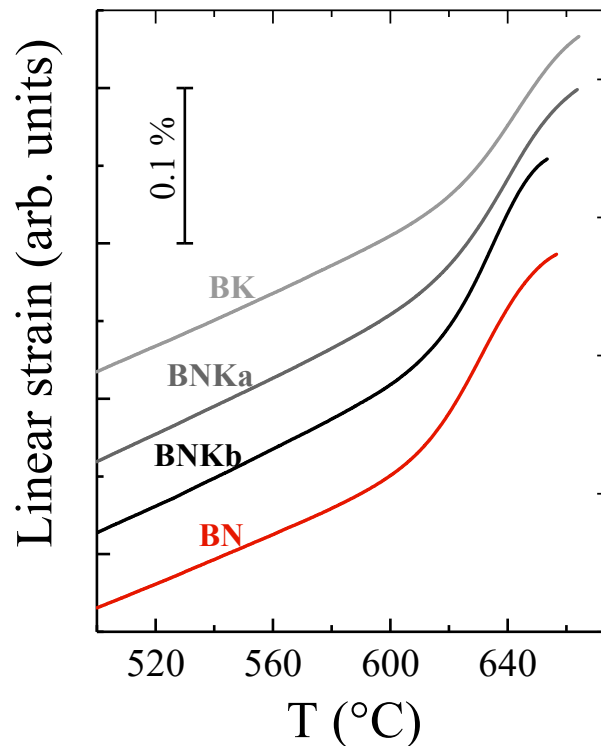


Figure A.II. 2 Dilatometric curves measured as discussed in the text. Measurements were carried out and provided by UniTn.

	SiO ₂	TiO ₂	Al ₂ O ₃	Fe ₂ O ₃	MnO	MgO	CaO	Na ₂ O	K ₂ O	P ₂ O ₅	M_a	NBO/T	K#	T_g (K)
BN	48.9	1.7	16.3	10.8	0.2	6.2	9.8	4.4	0.9	0.5	4.1	0.67	0.1	883
BNKa	49.7	1.6	16.1	11.5	0.2	5.9	7.6	4.0	2.1	0.8	4.6	0.62	0.3	889
BNKb	52.4	1.6	15.0	9.7	0.1	5.7	8.9	3.0	2.6	0.6	4.8	0.59	0.4	888
BK	50.9	1.6	15.7	10.1	0.2	6.0	9.3	1.2	4.0	0.6	4.3	0.60	0.7	893

Table A.II. 1 Chemical composition (wt %), acidity modulus M_a , NBO/T, K# and T_g of the studied glasses, obtained as explained in the text.

Raman measurements

Polarized Raman spectra were collected with the experimental set-up described in chapter 3 and treated as described in chapter 6. Moreover, for the HH spectra, a second-order polynomial was adopted as a baseline in the range between 200 and 1250 cm⁻¹ to account for the weak luminescence background underlying the Raman scattering.

All the glasses have been verified to be crystal-free and homogeneous before and after the T_g measurements by acquiring Raman spectra on 10 points on each sample, i.e. by looking at the spectral band between 680 and 700 cm⁻¹, typical of nano-crystal-bearing volcanic glasses¹⁵¹.

Results, discussion and conclusions

Figure A.II 3 shows the HH polarized Raman spectra acquired in the spectral region between 200 and 1250 cm⁻¹ from samples with K# ranging between 0.1 and 0.7 and M_a between 4.1 and 4.8. Broadly, the spectrum profile of the different samples looks alike, as expected from their similar chemical composition (Table A.II. 1).

The broad band peaked at ~ 460 cm⁻¹, which is peculiar of highly polymerized silicate glasses, is related to rocking and symmetric bending motions of bridging oxygen^{131,132}. Its invariancy suggests that the Si-O-Si bond angle is not significantly affected by the subtle chemical changes of our samples²¹³. The shoulder at about 580 cm⁻¹ is due to breathing oscillation modes of bridging oxygens in 4- and 3-membered rings

of tetrahedra¹³³. This spectral component is, however, influenced by the presence of Al_2O_3 , which causes a progressive broadening of the shoulder until it splits into two distinct contributions: the first one at 570 cm^{-1} and assigned to Al-O-Si 3-membered rings, the second one at 590 cm^{-1} and assigned to Si-O-Si 3-membered rings¹⁸⁷. In our glasses we observe a slight broadening of this shoulder as the composition becomes more sodic: the spectra, even though far from the frame described in¹⁴⁰, follow a similar trend. The weak band at $700\text{--}800\text{ cm}^{-1}$, which arises from the three-fold degenerate “rigid cage” vibrational mode of SiO_4 units¹³⁵, does not show any appreciable spectral change between the different samples.

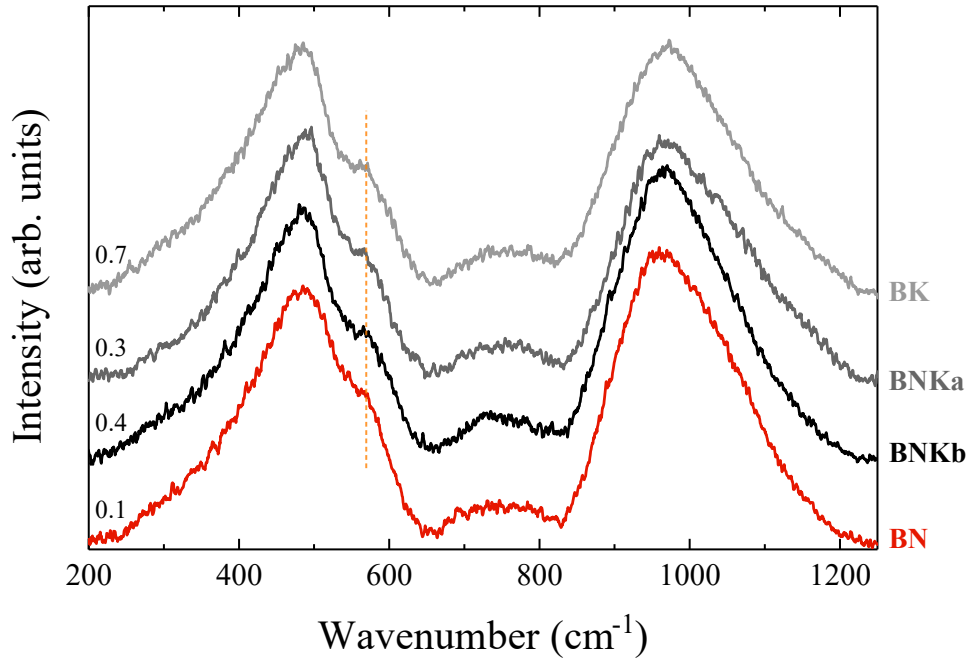


Figure A.II. 3 HH-polarized Raman spectra of samples characterized by $0.1 \leq K\# \leq 0.7$, after the baseline subtraction. Spectra of glasses are ordered in function of their T_g , from the highest (top, BK) to the lowest (bottom, BN).

The high frequency ($850\text{--}1250\text{ cm}^{-1}$) region of Raman spectra of silicate glasses can be fitted with a set of spectral components related to the different silica tetrahedral units (T), namely Q^n species, where n represents the number of bridging oxygens²³². In particular, the very broad spectral feature of the high-frequency region results from the stretching vibrations of T-O bonds between different Q^n species, thereby mirroring the variations of the inter-tetrahedral bond angles, force constants, and T-O distances. The

distribution of these species in glasses and melts is controlled by the chemistry of the sample^{125,131}. So, for a given number of bridging oxygens such as zero, one, two, three, or four; the different Q^n are termed Q^0 , Q^1 , Q^2 , Q^3 , and Q^4 , respectively, and their Gaussian-shaped Raman bands occur at about 800, 950, 990, 1090, and 1150 cm^{-1} , respectively¹³¹. The parameters (frequency shift, area, and width) of these spectral components give information about the polymerization degree of the glass, which is strongly influenced by the action of network modifier (NM) cations and of charge balancing ones.

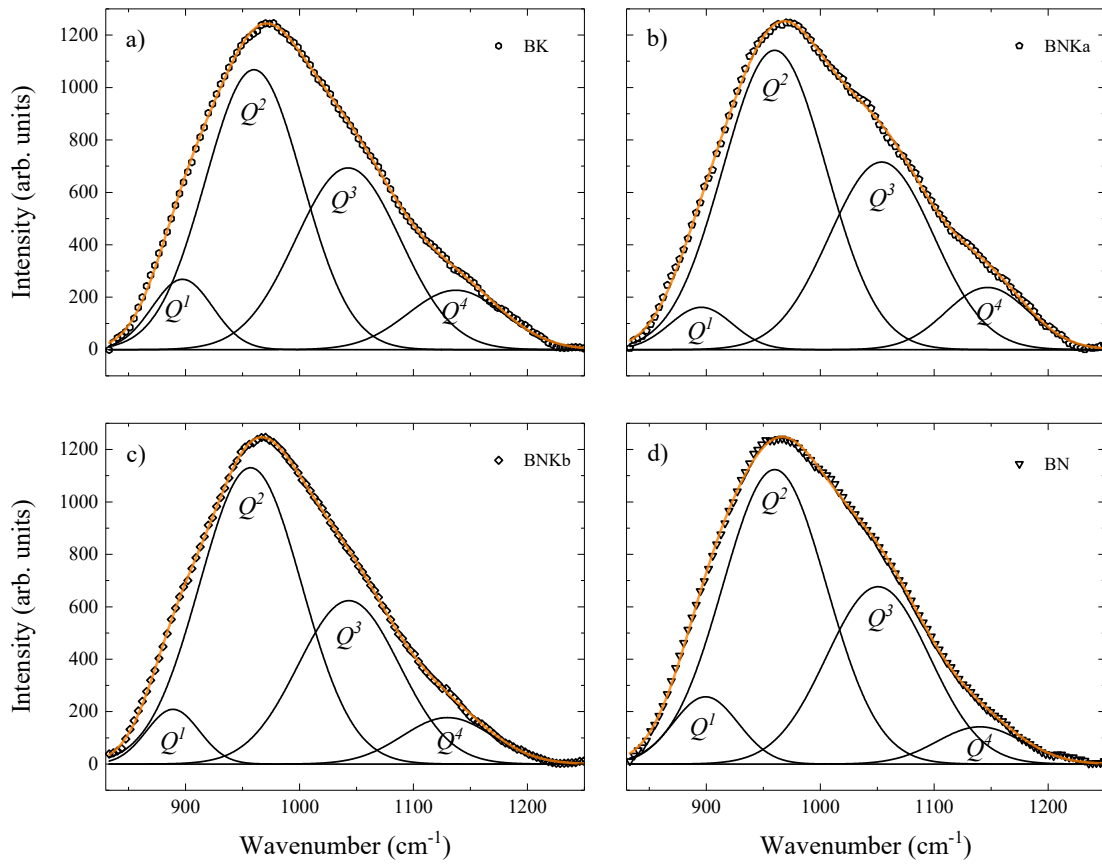


Figure A.II. 4 Deconvolution procedure of the high-frequency band of HH polarized Raman spectra. The orange lines are the cumulative fitting curves and the black lines represent the Gaussian components constrained as discussed in the text and quoted in Table A.II. 2 in terms of peak position, relative area, and FWHM.

When the system becomes more and more chemically complex, the presence of different types of T cations in a given Q^n unit may cause the band to split into two or more separated components. In fact, according to the literature^{102,139} the band splitting of Q^4 band, in the region between 1080 and 1200 cm^{-1} , is suggested to originate from two types of units, Al–O–Si and Si–O–Si, whilst Q^3 may encompass the contribution from the stretching of Fe^{3+} possibly in four-fold coordination state at (about 970 cm^{-1})²³³.

In this section, we overlook these effects due to the strong similarity of the whole high-frequency spectral profiles and focus the deconvolution in the spectral range from 830 to 1250 cm^{-1} , by considering only the Q^1 , Q^2 , Q^3 , and Q^4 species.

We run our analysis by constraining both the width and Raman shift of four Gaussian components to vary respectively within $\pm 5 \text{ cm}^{-1}$ and $\pm 20 \text{ cm}^{-1}$ with respect to the initially assigned values. It is known that Raman bands are not Gaussian in nature, limiting the validity of the fits^{227,234}. However, for a qualitative analysis of the spectra, Gaussian treatment can be a useful tool.

The results of the spectra deconvolution in terms of the 4 Gaussian components and the resulting fitting curve of the high-frequency Raman band are depicted in Figure A.II. 4, whilst Table A.II. 2 reports the values of the peak frequency, the relative area, and the full width at half maximum (FWHM) of each Gaussian with their errors reported in parentheses.

The Q^1 component shows a minimum in both peak position (888 cm^{-1}) and FWHM (54 cm^{-1}) for BNKa glass with $K\# = 0.3$ (slightly enriched in iron), whilst it remains quite constant for the other glasses by varying $\sim 4 \text{ cm}^{-1}$ its frequency without any significant trend, except those of the FWHM that slightly increase as the composition becomes more sodic and a decreasing $K\#$.

The Q^2 component does not vary significantly in its peak position ($\sim 960 \text{ cm}^{-1}$), except for the glass BNKa where it turns out peaked at a slightly lower frequency value ($\sim 957 \text{ cm}^{-1}$). However, both area and FWHM values of this component decrease in all the analyzed glasses as the $K\#$ increases.

The Q^3 peak frequency varies non-linearly between 1053 cm^{-1} and 1042 cm^{-1} , whilst both its area and FWHM slightly increase with $K\#$.

Finally, the Q^4 band frequency, as well, varies non-linearly between 1140 and 1130 cm^{-1} and shows a minimum in BNKa and, similarly to the Q^3 band, its area increases with increasing the K#, whilst its FWHM presents a small minimum for the BNKb glass.

In conclusion, facing the absence of substantial compositional changes among the analyzed glasses, we thereby observe quite small variations on the spectral parameter for the different Q^n species.

	BK	BNKa	BNKb	BN
<u>Position (cm^{-1})</u>				
Q^1	897 (1)	889 (1)	896 (2)	899 (1)
Q^2	960 (3)	957 (2)	960 (2)	960 (2)
Q^3	1043 (8)	1043 (3)	1054 (4)	1051 (3)
Q^4	1137 (4)	1130 (4)	1143 (2)	1140 (5)
<u>Relative area</u>				
Q^1	0.07 (.02)	0.05 (.01)	0.05 (.02)	0.08 (.02)
Q^2	0.48 (.09)	0.54 (.03)	0.55 (.06)	0.54 (.05)
Q^3	0.34 (.09)	0.29 (.03)	0.35 (.05)	0.32 (.04)
Q^4	0.10 (.01)	0.04 (.01)	0.09 (.00)	0.06 (.01)
<u>FWHM (cm^{-1})</u>				
Q^1	62 (4)	55 (2)	65 (7)	68 (5)
Q^2	100 (9)	105 (3)	107 (7)	107 (6)
Q^3	108 (13)	105 (6)	108 (8)	106 (7)
Q^4	99 (4)	94 (3)	86 (2)	88 (4)

Table A.II. 2 Values of the Raman shift, full-width at half maximum height (FWHM), and relative area of the Gaussian components used for the band deconvolution according to the procedure discussed in the text. In parentheses are reported the errors.

To formally account for the experimental data we start from the Shuker and Gammon assumption¹²⁸ (relations (2.10) and (2.11)) as described in section 3.2.

The low-frequency region of the HV is shown in Figure A.II. 5 in terms of reduced intensity and for a suitable comparison, they were normalized to the integrated area of the high-frequency region features (650-1250 cm^{-1}). The BP position was carefully determined by fitting its asymmetric shape to the (2.12). The BP position ω_{BP} shifts from $\sim 63 \text{ cm}^{-1}$ to $\sim 82 \text{ cm}^{-1}$, while its maximum becomes more and more suppressed reducing its intensity $I^{obs}(\omega)$ of $\sim 40\%$. This shift through higher frequencies is associated with a

decrease in Q^2 and an increase in Q^3 and Q^4 areas. We also point out that the higher the K# the lower the ω_{BP} and higher its reduced intensity and vice versa. However, the two intermediate samples BNKa and BNKb show a different relationship between K# and ω_{BP} . Indeed, the sample BNKa with K# = 0.3 has an $\omega_{BP} = 64.7 \text{ cm}^{-1}$, whilst BNKb has a K# = 0.4 with an $\omega_{BP} = 67.8 \text{ cm}^{-1}$.

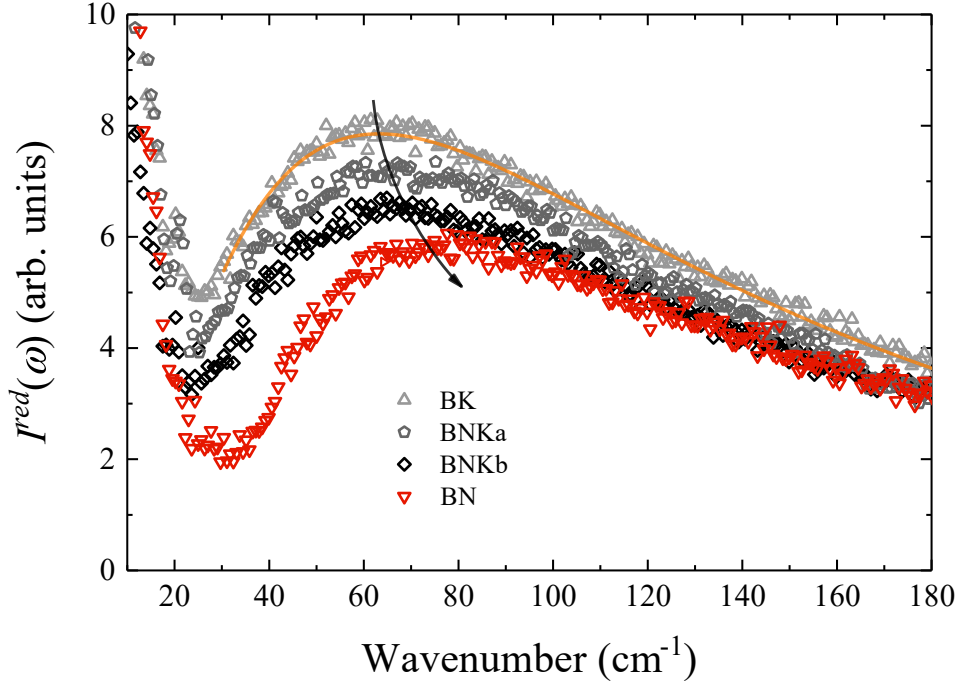


Figure A.II. 5 Reduced low-frequency HV Raman spectra of basalt glasses with different K#, after the subtraction of the rotational modes of air. The orange line provides an example of the log-normal function used for the fitting procedure as discussed in the text.

To better understand the evolution of the BP, we consider the scaled frequency $\nu = \omega/\omega_{BP}$ and we perform the variable transformation $g(\nu)d\nu = g(\omega)d\omega$. Assuming that $C(\omega) \propto \omega$ in the BP region^{143,144}, we can rewrite the rescaled intensity as:

$$I(\nu)^{red} = I(\omega)^{red} \omega_{BP}^2 \quad (\text{A.II. 1})$$

In Figure A.II. 6 a) we report the $I(\nu)^{red}$ spectra which show an excellent scaling by collapsing in the same master curve throughout the low-frequency range, *without any adjustable parameter*, only until the K# does not exceed, at least, 0.3 whilst the sample BN (characterized by the lowest K#) drops the scaling law and show a notably higher $I(\nu)^{red}$. To verify whether the frequency scaling exists, we consider a generic frequency ω_S , namely squeezing frequency. This frequency value is defined as the frequency at which all the spectra turn out with the same peak intensity¹⁷³, in the $\nu = \omega/\omega_S$ range, thus:

$$I(\nu_S)^{red} = I(\omega)^{red} \omega_S^2 \quad (\text{A.II. 2})$$

The squeezed spectra with varying K# are plotted in Figure A.II. 6 b). Similarly to the processing with (A.II. 1), samples with K# ranging between 0.3 and 0.7 perfectly collapse in the same master curve, all along with the low-frequency domain. However, the low-frequency tail $0.5 < \nu < 1.0$ of the squeezed spectra of BN glass, namely the lowest K# endmember, shows a remarkable inflection across the position of its maximum, which is also shifted forward with respect to the lowest K# samples.

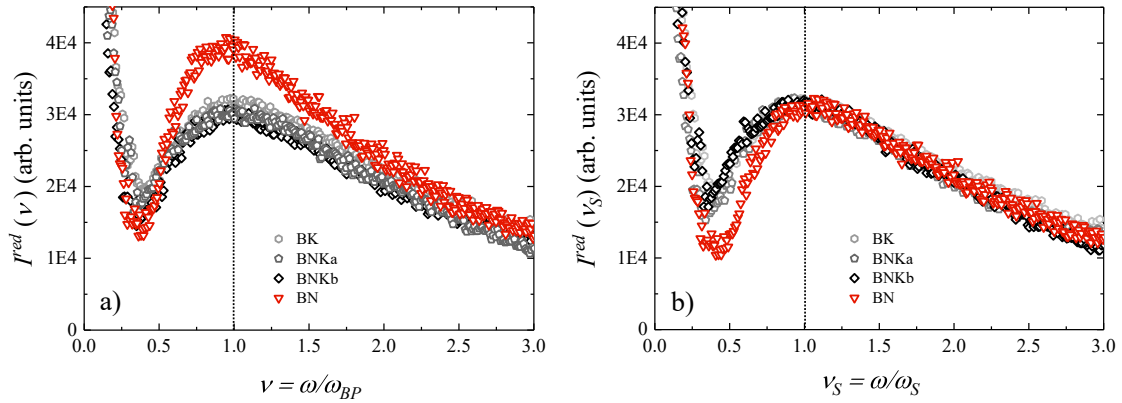


Figure A.II. 6 Squeezing procedure of the reduced spectra a) by applying (A.II. 1) and b) by applying (A.II. 2).

As it has been observed in Orsingher et al.¹⁹³ and Zanatta et al.²³⁵, a drop in the scaling procedure implies a drastic change in the modes rising the BP. This could be the

result of a structural modification of the sample. Indeed, we observe a variation of the ω_S of about $> 10\%$ of the ω_{BP} which can be viewed as a different vibrational behavior of the macroscopic medium within a network dominated by the different chemical species, that collectively contribute to the excess recorded in the BP.

Following this assumption, we can consider the relative abundance of alkalis $X^- K^+$ and $X^- Na^+$ sub-structures (where X can be $-O^-$ or AlO_4^-), as a hierarchical subnetwork, while the general silica network acquires a fixed amount of NMs and charge compensators. On the other hand, the $X^- Ca^{2+} X^-$ and $X^- Mg^{2+} X^-$ sub-structure, are located in overall motions relative to the two adjacent negative charges which drive each network toward a broader and disordered structure. In particular, their effect is to depolymerize the network and reduce the Si-O-Si angles, and changing the tetrahedral ring distribution¹³⁴. This behavior seems quite common in systems where alkaline earths replace alkalis in a general silica network²³⁶.

Figure A.II. 7 a) shows the relationships between the relative integrated areas of the Q^n species and their T_g . As expected in consideration of the relatively small changes in composition, the trend seems quite static. However, a slight increase in the Q^3 and Q^4 areas can be appreciated as the T_g increase. This behavior, although weak in our case, is in line with the experimental observation of pantelleritic glasses in Stabile et al.¹⁰² and the literature therein. Due to the broad shape of the high-frequency region of the spectra, we decided to not apply the splitting method of the Q^4 band as suggested in ref.¹⁴⁰ and neglecting the T^{2s} and the Fe^{3+} band.

On the other hand, the BP (black dots in Figure A.II. 6 b)) shifts to higher frequencies as the T_g decreases from 63.2 cm^{-1} (BK) to 80 cm^{-1} (BN) thereby similarly follows the parameter $K\#$, which increases as the BP shifts to lower frequencies. This result is in line with the behavior of a simple system i.e. the $(x-1)Na_2O-xSiO_2$ system observed in ref.²³⁷ and ref.^{190,238}. In this instance, the T_g decreases as the concentration of Na_2O increases²³⁷, whilst the BP shifts to higher frequencies, thereby decreasing its intensity and mirroring a different behavior of $g(\omega)$ ^{190,238}. Similarly, this behavior has been observed in the aluminosilicate system where the interplay of Al_2O_3 and Na-K mixing drastically influences both the melt viscosity and the BP position¹⁸⁷. In Figure A.II. 6 b) are also reported the values of ω_S which show a constant behavior by following the ω_{BP} at least from 888 to 893 K, where the samples are progressively enriched with

K₂O. As the composition becomes more sodic, the T_g decreases and shows different behavior of the scaling through ω_S , thus pointing out how the structure undergoes strong modifications within a small temperature range.

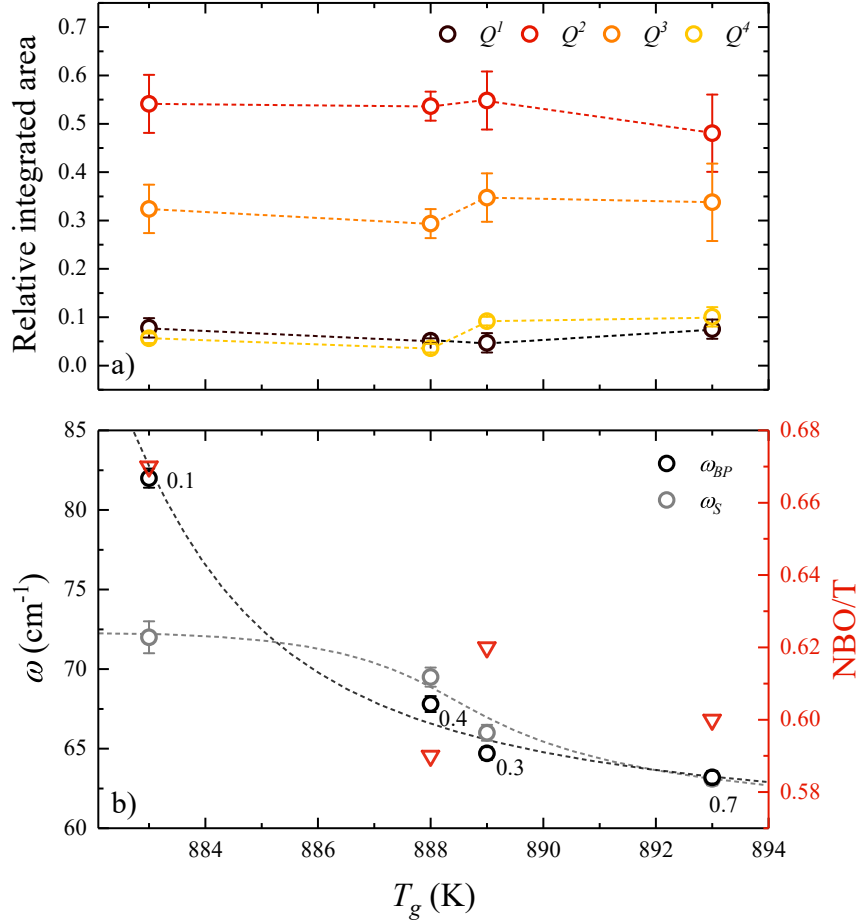


Figure A.II. 7 Relationship between the glass transition temperature T_g and the a) relative integrated areas of the Q^n species obtained by deconvolution procedure and b) relationship between T_g and ω_{BP} and ω_S obtained by fitting the low-frequency region to a log-normal function and by the scaling procedure as per (A.II. 2) respectively. Labels are the different K# corresponding to the different chemical composition as reported in Table A.II. 1. The dashed lines are guides for the eye.

In summary, we showed the effect of Na-K mixing in dry basaltic glasses, characterized in a narrow compositional range and suitable for CBF production. In the light of the above results, we conclude that:

I) The replacement of Na₂O with K₂O (thus increasing K#) broadly results in an increase in the glass transition temperature;

II) The high-wavenumbers Raman bands corresponding to the Q^3 and Q^4 , show only minor correlations with the glass transition temperature thus revealing only slight variations of the polymerization degree of the structure.

III) The position of the boson peak obtained from the low-wavenumber Raman data shows an exponential decay-like correlation with the glass transition temperature.

IV) The existence of a scaling law for the BP is verified in the range of $0.3 \leq K\# \leq 0.7$ and in the NBO/T range of about 0.62 - 0.59. This means that the intensity variation of the BP is only an apparent effect due to its shift. Microscopically, the Na-K replacement induces only a continuous evolution of the vibrational properties.

V) The drop of the scaling procedure, occurring at $K\# \leq 0.1$ and $NBO/T = 0.67$, suggests a deep structural modification with a re-distribution of the collective modes in the VDoS, towards a less polymerized structure.

The present study shows and underpins the significance of Raman spectroscopy in the understanding of the chemical-induced modifications of both volcanic and technical glasses. Finally, the results show how the BP scaling can be a crucial method for the structural analysis, in particular in a so narrow chemical composition.

APPENDIX III: The case of SiO₂ - Na₂O join

In this appendix we consider the sodium-silicate system of the type $(1 - X)\text{SiO}_2 - X\text{Na}_2\text{O}$, where X is the molar fraction of network modifier ranging between 15 and 45 mol % of Na₂O. Although widely different in composition from either natural melts or those of industrial interest, this system represents a simple and useful prototype to investigate the response of the glass structure^{190,239–242}, melt properties^{124,237,243,244} and elasticity^{245–248} resulting from the variation of Na₂O within the SiO₂ network. The goal of this section is to Figure out the connection between these properties, examining different experimental results from the records (see Table A.III. 1).

	SiO ₂	N2	N3	N4
SiO ₂	100	80	70	60
Na ₂ O	0	20	30	40
r (g cm ⁻³)	2.2 ¹⁷³	2.4 ²⁴⁵	2.5 ²⁴⁵	2.5 ²⁴⁵
K/G (GPa)	1.18 [§]	1.40 [§]	1.54 [§]	1.77 [§]
v_L (m s ⁻¹)	5972 ¹⁷³	5466.15 ²⁴⁵	5446.06 ²⁴⁵	5444.65 ²⁴⁵
v_T (m s ⁻¹)	3769 ¹⁷³	3296.26 ²⁴⁵	3182.71 ²⁴⁵	3143.47 ²⁴⁵
ω_D (THz)	10.4 ^{**}	9.39 ^{**}	9.18 ^{**}	9.15 ^{**}
ω_{BP} (cm ⁻¹)	48.5 ¹⁷³	67.3 ¹⁹⁰ - 64 ²³⁸	55 ²³⁸	83.1 ¹⁹⁰ - 59 ²³⁸

[§] Calculated by the relations $v_T = \sqrt{G/\rho}$ and $v_L = \sqrt{[K + (4/3)G]/\rho}$.

* Calculated by fitting the viscosity data obtained by Urbain et. al 1982¹⁶¹ to the MYEGA formulation (1.18).

** Calculated as per (1.13) by using data from Zanatta et al.¹⁷³ and Vaills et al. 1996²⁴⁵.

Table A.III. 1 Density ρ , bulk and shear modulus ratio (K and G respectively), longitudinal sound velocity v_L , transversal sound velocity v_T , of silica are from ref.¹⁷³ and ρ , v_L and v_T of binary sodosilicate glasses from data of Vaills et al.²⁴⁵ and T_g from Knoche et al.²⁴⁵. Debye frequency ω_D were obtained from (1.13) and ω_{BP} is the position of the boson peak maximum in the plot of $I^{red}(\omega)$ versus ω . The BP position from ref.¹⁹⁰ has been obtained by fitting the low-frequency region of the spectra to the log-normal.

Starting from the TCT, we describe the glass-forming ability of this system based on the numbers of constraints of the bond bending (BB), bond stretching (BS), number

of non-bridging oxygens (NBO) and of bridging oxygen (BO)^{58,249}, which is function of the ratio of NF and NM. According to the mean field approximation, the stability of the resultant glass is reached when the glass is free of internal stresses and floppy modes. In this condition the atomic network is named isostatic and it is obtained for $n_c = 3$, which is achieved in the case of the system Na₂O-SiO₂ at $X_{iso} = 0.2$ ²⁵⁰ (20% mol of Na₂O). As such, sodium silicate is stressed-rigid ($n_c > 3$) for $X < 0.2$ and flexible ($n_c < 3$) for $X > 0.2$ (Figure A.III. 1 d)). These predictions are in agreement with experimental results, as sodium silicate exhibits a minimum in enthalpy relaxation DH_{nr} around $X = 0.2$ (Figure A.III. 1 a)). Similarly, for low content of Na₂O ($X < 0.15$) the elastic constants dependencies with x are driven by the silicon density. For higher content ($X > 0.15$) the force constant of Na-O bond plays a major role, giving as a result a non-monotonic behavior of the longitudinal modulus M , which is characterized by the occurrence of a minimum value around $X = 0.15$ as reported in ref.²⁴⁵ and showed in Figure A.III. 1 c).

The boson peak position ω_{BP} generally shift to higher frequencies as the Na₂O increases, in particular ω_{BP} falls quite far from its linear trend once Na₂O reach the 20% of the total mol in the system (ascribed by change in the mean atomic volume)²³⁸, whilst the same trend with different positions has been observed in the range slightly above the isostatic threshold (in this case ascribed to the Elliot-type discontinuities also named correlation lengths)¹⁹⁰ Figure A.III. 1 b). The non-negligible variation of the BP position found in literature for the same compound (i.e. in the sample N2 and N4) could be ascribed, at least, to the fitting procedure (i.e. in ref.¹³⁹ and ref.²⁵¹ the position has been achieved by fitting the low-frequency region of parallel polarized spectra to a Lorentzian function thereby including some spectral components related to the rotational modes of the air). Moreover, in ref.¹⁹⁰ the BP position seems obtained through a visual inspection of the spectrum without applying the air subtraction procedure. However only in ref.²³⁸ the position is determined by fitting the BP to a log-normal function as suggested by ref.¹⁴⁶.

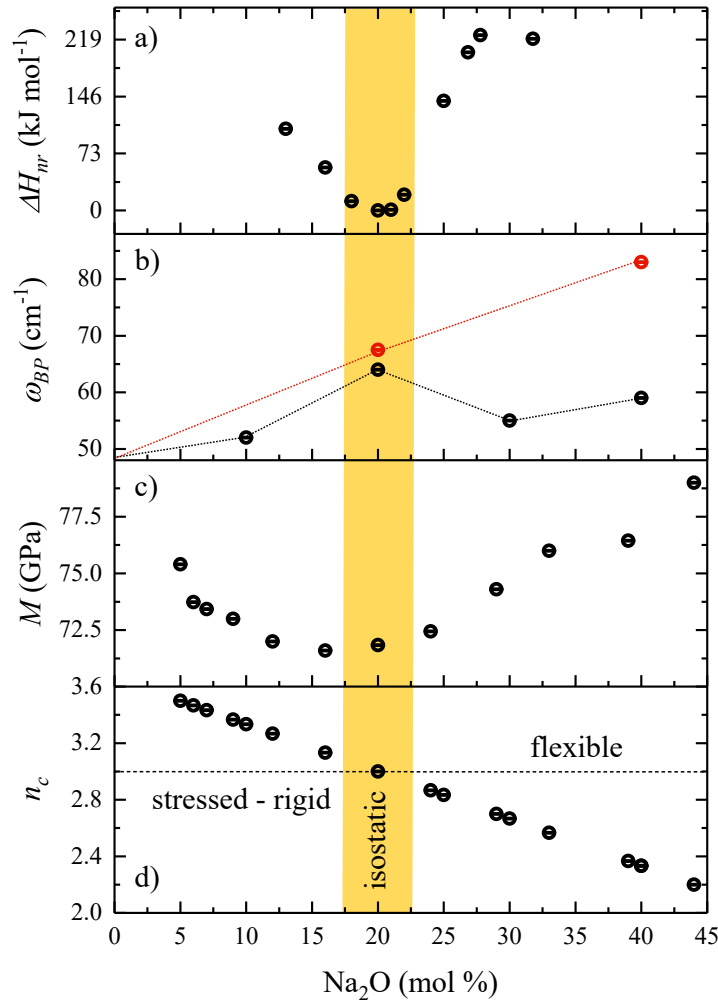


Figure A.III. 1 Vibrational, elastic and topological parameters in $\text{Na}_2\text{O-SiO}_2$ glasses. a) Non-reversible heat flow ΔH_{nr} at the glass transition²⁵⁰, b) boson peak position ω_{BP} comparing two datasets black cut-dots from ref.²³⁸ and red cut-dots (fitted to the log-normal function) from ref.¹⁹⁰, c) longitudinal elastic modulus M^{245} and d) number of constraints per atom (n_c) calculated as $n_c = (11 - 10x)/3$. All these values were experimentally obtained and calculated at 300 K.

The onset of the anomalies, once the system reach $\sim 20\%$ of Na_2O , seems ascribable to the well documented process called phase separation in the LRO structural domain, occurring in the supercooled liquid with 18.56% mol of Na_2O , as reported in ref.²⁵². This process results in a heterogeneous matrix in which different nano-sized regions having different concentration (probably due to segregation^{187,253}), probably originates nano-domains with different elastic constants, which may deeply influences the general behavior of the elastic medium properties. In Figure A.III. 2 is reported the low-

temperature data from micro-penetration measurements (10^9 - 10^{11} Pa s) and the high-temperature ones by concentric cylinder data (10^0 - 10^3 Pa s) from ref.¹⁶¹. The non-Arrhenian trend were fit to the MYEGA equation (1.18) and the extrapolated m and T_g are plotted in function of composition (yellow-cut dots) in Figure A.III. 3 a) and b).

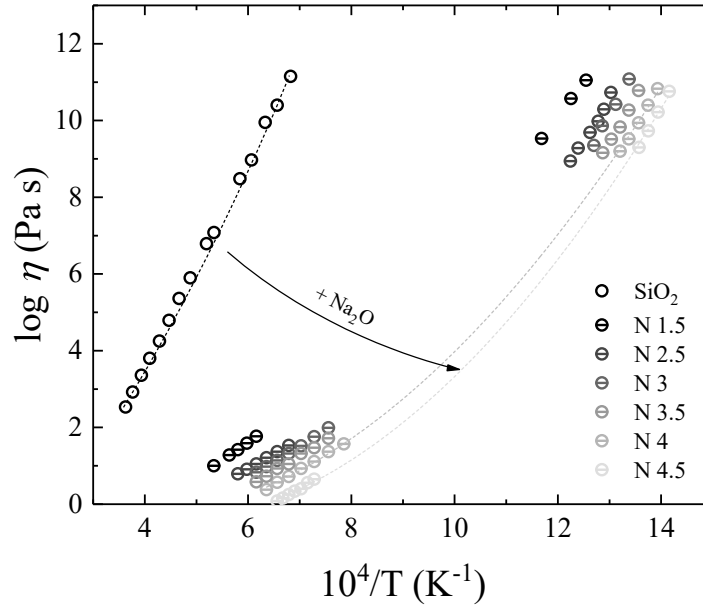


Figure A.III. 2 Plot of the melt viscosities in the Na_2O - SiO_2 system (with $15 < \text{Na}_2\text{O mol.}\% < 45$) obtained by the combination of the concentric cylinder and micropenetration data from ref.²³⁷ (grey-scale cut-dots) compared to the melt viscosity of SiO_2 (black circle) from ref.¹⁶¹.

The sharp reduction of T_g alters the mechanical equilibrium that prevailed²⁴⁹ in the pristine glass (pure silica in this case) and drives mixed glasses to become stressed rigid. This is largely the case because the bond-bending constraint of bridging oxygen atoms that were intrinsically broken²⁵⁴ at ~ 1450 K, becomes restored in the weakly alloyed glass as T_g dramatically drops to ~ 700 K. However, upon continuous addition of Na_2O the mixed glass softens as network connectivity decreases, and one expects an elastic phase transition from a stressed rigid phase to a floppy phase. Is evident how this mechanism is described by the interplay of the shear and bulk modulus values in Figure A.III. 3 c) and d).

The different trend of the shear and bulk modulus G and K shows a quite pronounced match between the flexible and rigid domain. In particular for $X < 0.2$ the

shear deformations are dominant whilst the bulk ones slightly increase from $X \sim 0.15$ (few molar fractions before the isostatic threshold).

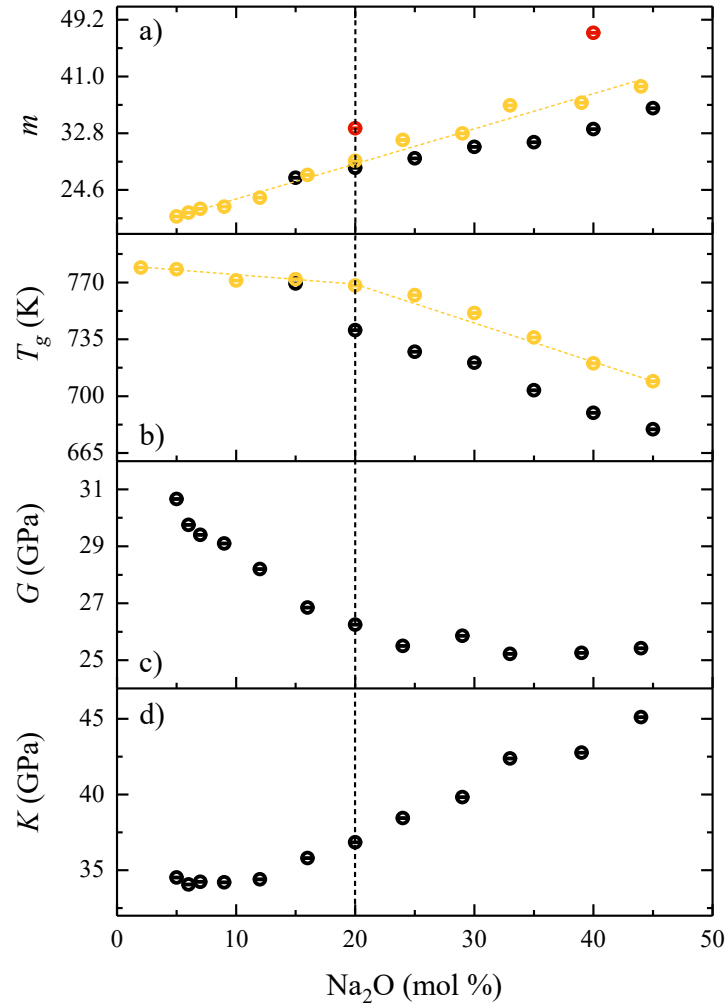


Figure A.III. 3 Correlations among T_g , m and elastic moduli K and G . a) Fragility index calculated by fitting viscosity data²³⁷ to the MYEGA equation (black-cut dots) compared to that obtained through elastic constants via (5.1) from data of ref.²⁴⁵ (yellow-cut dots), and those obtained via (5.2) from data of ref.¹⁹⁰ (red-cut dots). b) Glass transition temperatures calculated by MYEGA (black-cut dots) compared to the dilatometric one (yellow-cut dots)²³⁷. Note that only the viscosity data measured at both high and low temperature have been selected from ref.²³⁷ c) shear elastic modulus G ²⁴⁵, d) bulk modulus K obtained via $M = K + (4/3)G$. The black dashed line represents the isostatic threshold which is obtained as discussed in the text.

The T_g obtained by MYEGA and the dilatometric one, match at about 15% Na₂O mol concentration and then differing of about 30 K along the join, Figure A.III. 3 b). However, no comparable values for m are available in the literature and we thus obtain new fragility values by using the expression relating the elastic constant K and G (Table A.III.3) of glasses to its glass forming liquid properties and that of the boson peak, equations (5.1) and (5.2) respectively.

The results are shown in Figure A.III. 3 a) yellow-cut dots are obtained by relation (5.1) whilst red-cut dots represent m obtained by relation (5.2), together with those obtained by means of the MYEGA equation (black dashed dots). Their positive and linear correlation slightly differs only in terms of slope with those obtained by viscosity data. In particular m results slightly underestimated by adopting the Novikov approach, immediately after the value of 20% of Na₂O, preserving however the benefit of the doubt for $X < 0.15$, since no data below this composition are available. Unlike the K/G -derived fragility, the only two m values retrieved from the ω_{BP} relation, are quite overestimated.

These observations again suggest that fragility of this glass forming liquid may be embedded into the glassy elastic properties^{22,23}. Although the boson peak data seem conflictual to each other^{190,238}, they show an overall linear trend for the few represented compositions. Moreover, if the BP shift is compared to the elastic medium evolution (represented by ω_D) we can observe a positive shift of the ω_{BP} and a negative one of the ω_D (see Table A.III. 1). As a matter of fact, this trend seems in contradiction with that discussed in section 5, (as well as studies dealing with the Debye scaling of the BP²⁸) thereby showing an opposite behavior. However, based on the evolution of the medium, the different elastic moduli M , G and K may play a role in connection to the internal stress described by the TCT and the isostatic threshold^{255,256}. The correlation between BP and glass-chemistry is poorly investigated, therefore evidence and data needed to generate new models are still missing and the above discussion remains highly speculative. Thus, further investigations are mandatory in order to properly validate future study in this field.

REFERENCES

1. Pliny The Elder, N. *Naturalis Historia*. (Translated by John Bostock, Henry Thomas Riley). *The natural history of Pliny*. (1857). doi:10.5962/bhl.title.56616.
2. Main, D. Humankind's Most Important Material. *Atl.* (2018).
3. Zachariasen, W. H. The atomic arrangement in glass. *J. Am. Chem. Soc.* **54**, 3841–3851 (1932).
4. Zanutto, E. D. & Mauro, J. C. The glassy state of matter: Its definition and ultimate fate. *J. Non. Cryst. Solids* **471**, 490–495 (2017).
5. Mysen, B. O. & Richet, P. *Silicate glasses and melts - Properties and structure. Developments in Geochemistry*. (Elsevier, 2005).
6. Musgraves, D. J., Hu, J. & Calvez, L. *Springer Handbook of Glass. Springer Handbooks* (Springer, 2019).
7. Mauro, J. C., Yue, Y. Z., Ellison, A. J., Gupta, P. K. & Allan, D. C. Viscosity of glass-forming liquids. *Proc. Natl. Acad. Sci. U. S. A.* **106**, 19780–4 (2009).
8. Gupta, P. K. & Mauro, J. C. Composition dependence of glass transition temperature and fragility. I. A topological model incorporating temperature-dependent constraints. *J. Chem. Phys.* **130**, (2009).
9. Reinsch, S., Nascimento, M. L. F., Müller, R. & Zanutto, E. D. Crystal growth kinetics in cordierite and diopside glasses in wide temperature ranges. *J. Non. Cryst. Solids* **354**, 5386–5394 (2008).
10. Angell, C. A., Ngai, K. L., McKenna, G. B., McMillan, P. F. & Martin, S. W. Relaxation in glassforming liquids and amorphous solids. *J. Appl. Phys.* **88**, 3113–3157 (2000).
11. Mysen, B. O. Relationships between silicate melt structure and petrologic processes. *Earth Sci. Rev.* **27**, 281–365 (1990).
12. Dingwell, D. B. Volcanic dilemma: Flow or blow? *Science* vol. 273 1054–1055 (1996).
13. Gonnermann, H. M. & Manga, M. Dynamics of magma ascent in the volcanic conduit. in *Modeling Volcanic Processes: The Physics and Mathematics of Volcanism* (eds. Fagents, S. A., Gregg, T. K. P. & Lopes, R. M. C. E.) 55–84 (Cambridge University Press, 2013). doi:10.1017/CBO9781139021562.004.

-
14. Zhang, Y. A criterion for the fragmentation of bubbly magma based on brittle failure theory. *Nature* **402**, 648–650 (1999).
 15. Di Genova, D. *et al.* In situ observation of nanolite growth in volcanic melt: A driving force for explosive eruptions. *Sci. Adv.* **6**, (2020).
 16. Taddeucci, J. *et al.* Fracturing and healing of basaltic magmas during explosive volcanic eruptions. *Nat. Geosci.* **14**, 248–254 (2021).
 17. Richet, P., Lejeune, A. M., Holtz, F. & Roux, J. Water and the viscosity of andesite melts. *Chem. Geol.* **128**, 185–197 (1996).
 18. Di Genova, D., Caracciolo, A. & Kolzenburg, S. Measuring the degree of “nanotilization” of volcanic glasses: Understanding syn-eruptive processes recorded in melt inclusions. *Lithos* **318–319**, 209–218 (2018).
 19. Liebske, C., Behrens, H., Holtz, F. & Lange, R. A. The influence of pressure and composition on the viscosity of andesitic melts. *Geochim. Cosmochim. Acta* **67**, 473–485 (2003).
 20. Di Genova, D., Zandona, A. & Deubener, J. Unravelling the effect of nano-heterogeneity on the viscosity of silicate melts: Implications for glass manufacturing and volcanic eruptions. *J. Non. Cryst. Solids* **545**, 120248 (2020).
 21. Bouhifd, M. A., Richet, P., Besson, P., Roskosz, M. & Ingrin, J. Redox state, microstructure and viscosity of a partially crystallized basalt melt. *Earth Planet. Sci. Lett.* **218**, 31–44 (2004).
 22. Scopigno, T., Ruocco, G., Sette, F. & Monaco, G. Is the Fragility of a Liquid Embedded in the Properties of Its Glass? *Science* **302**, 849–852 (2003).
 23. Novikov, V. N., Ding, Y. & Sokolov, A. P. Correlation of fragility of supercooled liquids with elastic properties of glasses. *Phys. Rev. E - Stat. Nonlinear, Soft Matter Phys.* **71**, 1–12 (2005).
 24. Novikov, V. N. & Sokolov, A. P. Poisson’s ratio and the fragility of glass-forming liquids. *Nature* **431**, 961–963 (2004).
 25. Yannopoulos, S. N. & Johari, G. P. Glass behaviour: Poisson’s ratio and liquid’s fragility. *Nature* **442**, 961–963 (2006).
 26. Sokolov, A. P., Novikov, V. N. & Kisliuk, A. Fragility and mechanical moduli: Do they really correlate? *Philos. Mag.* **87**, 613–621 (2007).
 27. Cassetta, M. *et al.* Estimating the viscosity of volcanic melts from the vibrational

-
- properties of their parental glasses. *Sci. Rep.* **8**, 1–14 (2021).
28. Baldi, G., Fontana, A. & Monaco, G. Vibrational dynamics of non-crystalline solids. *arXiv* **2011**, 10415 (2020).
 29. Zanutto, E. D. & Mauro, J. C. The glassy state of matter: Its definition and ultimate fate. *J. Non. Cryst. Solids* **471**, 490–495 (2017).
 30. Cavagna, A. Supercooled liquids for pedestrians. *Phys. Rep.* **476**, 51–124 (2009).
 31. Angell, C. A., Scamehorn, C. A., List, D. J. & Kieffer, J. Glass forming liquid oxides at the fragile limit of the viscosity-temperature relationship. *From Proceedings XV Int. Congr. Glas. Leningrad.* 204–209 (1989).
 32. Angell, C. A., Poole, P. H. & Shao, J. Glass-forming liquids, anomalous liquids, and polyamorphism in liquids and biopolymers. *Nuovo Cim. D* **16**, 993–1025 (1994).
 33. Caponi, S. *et al.* Ergodicity breaking in strong and network-forming glassy systems. *Phys. Rev. B - Condens. Matter Mater. Phys.* **79**, 1–4 (2009).
 34. Shaw, H. R. Viscosities of magmatic silicate liquids; an empirical method of prediction. *American Journal of Science* vol. 272 870–893 (1972).
 35. Bottinga, Y. W. The viscosity of magmatic silicate: a model for calculation. *American Journal of Science* 438–475 (1972).
 36. Hess, K. U. & Dingwell, D. B. Viscosities of hydrous leucogranitic melts: a non-Arrhenian model. *Am. Mineral.* **81**, 1297–1300 (1996).
 37. Toplis, M. J., Dingwell, D. B., Hess, K. U. & Lenci, T. Viscosity, fragility, and configurational entropy of melts along the join $\text{SiO}_2\text{-NaAlSiO}_4$. *Am. Mineral.* **82**, 979–990 (1997).
 38. Richet, P. Viscosity and configurational entropy of silicate melts. *Geochim. Cosmochim. Acta* **48**, 471–483 (1984).
 39. Adam, G. & Gibbs, J. H. On the Temperature Dependence of Cooperative Relaxation Properties in Glass-Forming Liquids. *J. Chem. Phys.* **43**, 139–146 (1965).
 40. Kauzmann, W. The Nature of the Glassy State and the Behavior of Liquids at Low Temperatures. *Chem. Rev.* **43**, 219–256 (1948).
 41. Gibbs, J. & Di Marzio, E. Nature of the Glass Transition and the Glassy State. *J. Chem. Phys.* **28**, 373–383 (1958).
-

-
42. Stebbins, J. F., Carmichael, I. S. E. & Moret, L. K. Heat capacities and entropies of silicate liquids and glasses. *Contrib. to Mineral. Petrol.* **86**, 131–148 (1984).
 43. Stillinger, F. H. Supercooled liquids, glass transitions, and the Kauzmann paradox. *J. Chem. Phys.* **88**, 7818–7825 (1988).
 44. Debenedetti, P. G. & Stillinger, F. H. Supercooled liquids and the glass transition. *Nature* vol. 410 259–267 (2001).
 45. Zanutto, E. D. & Cassar, D. R. The race within supercooled liquids - Relaxation versus crystallization. *J. Chem. Phys.* **149**, (2018).
 46. Cavagna, A., Attanasi, A. & Lorenzana, J. Viscoelasticity and metastability limit in supercooled liquids. *Phys. Rev. Lett.* **95**, 1–4 (2005).
 47. Zanutto, E. D. & Gupta, P. K. Do cathedral glasses flow?—Additional remarks. *Am. J. Phys.* **67**, 260–262 (1999).
 48. Moulton, B. J. A., Rodrigues, A. M., Pizani, P. S., Sampaio, D. V. & Zanutto, E. D. A Raman investigation of the structural evolution of supercooled liquid barium disilicate during crystallization. *Int. J. Appl. Glas. Sci.* **9**, 510–517 (2018).
 49. Dingwell, D. B. & Webb, S. L. Structural relaxation in silicate melts and non-Newtonian melt rheology in geologic processes. *Phys. Chem. Miner.* **16**, 508–516 (1989).
 50. Maxwell, J. C. On the Dynamical Theory of Gases. *Phil. Trans. Roy. Soc. Lon.* **157**, 49–88 (1867).
 51. Frenkel, J. *Kinetic Theory Of Liquids*. vol. 0 (Clarendon Press, 1946).
 52. Dingwell, D. B. & Webb, S. L. Structural relaxation in silicate melts and non-Newtonian melt rheology in geologic processes. *Phys. Chem. Miner.* **16**, 508–516 (1989).
 53. Glasstone, S., Laidler, K. J. & Eyring, H. The Theory of Rate Processes. *J. Chem. Educ.* **19**, 249 (1942).
 54. Schubert, U. Introduction to glass science and technology. Von J. E. Shelby. Royal Society of Chemistry, Cambridge, 1997. 244 S., Broschur, 18.95 £.— ISBN 0-85404-533-3. *Angew. Chemie* (1997) doi:10.1002/ange.19971092243.
 55. Phillips, W. A. Topology of covalent non-crystalline solids: Short-range order in chalcogenide alloys. *J. Non. Cryst. Solids* **34**, 153–181 (1979).
 56. Phillips, J. C. & Thorpe, M. F. ScienceDirect.com - Solid State Communications

-
- Constraint theory, vector percolation and glass formation. *Solid State Commun.* **53**, 699–702 (1985).
57. Trachenko, K. & Dove, M. T. Floppy modes in silica glass under pressure. *J. Phys. Condens. Matter* **14**, 1143–1152 (2002).
58. Bauchy, M. Deciphering the atomic genome of glasses by topological constraint theory and molecular dynamics : A review. *Comput. Mater. Sci.* **159**, 95–102 (2019).
59. Denisov, V. N., Mavrin, B. N., Podobedov, V. B., Sterin, K. E. & Varshal, B. G. Law of conservation of momentum and rule of mutual exclusion for vibrational excitations in hyper-Raman and Raman spectra of glasses. *J. Non. Cryst. Solids* **64**, 195–210 (1984).
60. Zanatta, M. Vibrational Dynamics In Strong Glasses: The Case Of Densified v-SiO₂ And SiSe₂. (2011).
61. Ashcroft, N. *Solid state physics*. (Holt Rinehart and Winston, 1976).
62. Berman, R. Thermal Conductivity of Glasses at Low Temperature. *Phys. Rev. Lett.* **76**, 315 (1942).
63. Dianoux, A. J., Buchenau, U., Prager, M. & Nücker, N. Low frequency excitations in vitreous silica. *Phys. B+C* **138**, 264–268 (1986).
64. Schirmacher, W. Thermal conductivity of glassy materials and the ‘boson peak’. *Europhys. Lett.* **73**, 892–898 (2006).
65. Sokolov, A. P. *et al.* Low-temperature anomalies in strong and fragile glass formers. *Phys. Rev. Lett.* **78**, 2405–2408 (1997).
66. Buchenau, U. *et al.* Low-frequency modes in vitreous silica. *Phys. Rev. B* **34**, 5665–5673 (1986).
67. Ruta, B. *et al.* Acoustic excitations in glassy sorbitol and their relation with the fragility and the boson peak. *J. Chem. Phys.* **137**, (2012).
68. Rufflé, B., Guimbretiére, G., Courtens, E., Vacher, R. & Monaco, G. Glass-specific behavior in the damping of acousticlike vibrations. *Phys. Rev. Lett.* **96**, 045502 (2006).
69. Chumakov, A. I. *et al.* Role of disorder in the thermodynamics and atomic dynamics of glasses. *Phys. Rev. Lett.* **112**, 1–6 (2014).
70. Zanatta, M. *et al.* Debye to non-Debye scaling of the Boson peak dynamics:
-

-
- Critical behavior and local disorder in vitreous germania. *J. Chem. Phys.* **135**, 3–8 (2011).
71. Taraskin, S. N., Loh, Y. L., Natarajan, G. & Elliott, S. R. Origin of the boson peak in systems with lattice disorder. *Phys. Rev. Lett.* **86**, 1255–1258 (2001).
 72. Schirmacher, W., Ruocco, G. & Scopigno, T. Acoustic attenuation in glasses and its relation with the boson peak. *Phys. Rev. Lett.* **98**, 1–4 (2007).
 73. Schirmacher, W. Some comments on fluctuating-elasticity and local oscillator models for anomalous vibrational excitations in glasses. in *Journal of Non-Crystalline Solids* vol. 357 518–523 (2011).
 74. Schmid, B. & Schirmacher, W. Raman scattering and the low-frequency vibrational spectrum of glasses. *Phys. Rev. Lett.* **100**, 1–4 (2008).
 75. Grigera, T. S., Martín-Mayor, V., Parisi, G. & Verrocchio, P. Phonon interpretation of the ‘boson peak’ in supercooled liquids. *Nature* **422**, 289–292 (2003).
 76. Rufflé, B., Parshin, D. A., Courtens, E. & Vacher, R. Boson peak and its relation to acoustic attenuation in glasses. *Phys. Rev. Lett.* **100**, 015501 (2008).
 77. Parshin, D. A., Schober, H. R. & Gurevich, V. L. Vibrational instability, two-level systems, and the boson peak in glasses. *Phys. Rev. B - Condens. Matter Mater. Phys.* **76**, 064206 (2007).
 78. Gurevich, V. L., Parshin, D. A. & Schober, H. R. Anharmonicity, vibrational instability, and the Boson peak in glasses. *Phys. Rev. B - Condens. Matter Mater. Phys.* **67**, 094203 (2003).
 79. Duval, E., Mermet, A. & Saviot, L. Boson peak and hybridization of acoustic modes with vibrations of nanometric heterogeneities in glasses. *Phys. Rev. B - Condens. Matter Mater. Phys.* **75**, 024201 (2007).
 80. Berthier, L. & Biroli, G. Theoretical perspective on the glass transition and amorphous materials. *Rev. Mod. Phys.* **83**, 587–645 (2011).
 81. Sokolov, A. P., Kisliuk, A., Soltwisch, M. & Quitmann, D. Medium-range order in glasses: Comparison of Raman and diffraction measurements. *Phys. Rev. Lett.* **69**, 1540–1543 (1992).
 82. Börjesson, L., Hassan, A. K., Swenson, J., Torell, L. M. & Fontana, A. Is there a correlation between the first sharp diffraction peak and the low frequency
-

-
- vibrational behavior of glasses? *Phys. Rev. Lett.* **70**, 1275–1278 (1993).
83. Angell, C. A. Formation of glasses from liquids and biopolymers. *Science* **267**, 1924–1935 (1995).
84. Mauro, J. C., Yue, Y., Ellison, A. J., Gupta, P. K. & Allan, D. C. Viscosity of glass-forming liquids. *Proc. Natl. Acad. Sci. U. S. A.* **106**, 19780–19784 (2009).
85. Angell, C. A. Spectroscopy simulation and scattering, and the medium range order problem in glass. *J. Non. Cryst. Solids* **73**, 1–17 (1985).
86. Angell, C. A. Perspective on the glass transition. *J. Phys. Chem. Solids* **49**, 863–871 (1988).
87. Böhmer, R., Ngai, K. L., Angell, C. A. & Plazek, D. J. Nonexponential relaxations in strong and fragile glass formers. *J. Chem. Phys.* **99**, 4201–4209 (1993).
88. Rössler, E., Hess, K. U. & Novikov, V. N. Universal representation of viscosity in glass forming liquids. *J. Non. Cryst. Solids* **223**, 207–222 (1998).
89. Novikov, V. Vibration anharmonicity and fast relaxation in the region of the glass transition. *Phys. Rev. B - Condens. Matter Mater. Phys.* **58**, 8367–8378 (1998).
90. Nemilov, S. The relation between the free energy of activation for viscous flow and the energy of the chemical bonds in glasses. *Sov. Physics-Solid State* **6**, 1075–1078 (1964).
91. Di Genova, D. *et al.* A compositional tipping point governing the mobilization and eruption style of rhyolitic magma. *Nature* **552**, 235–238 (2017).
92. Angell, C. A. Glass-formers and viscous liquid slowdown since David turnbull: Enduring puzzles and new twists. *MRS Bull.* **33**, 544–555 (2008).
93. Yue, Y. Anomalous enthalpy relaxation in vitreous silica. *Front. Mater.* **2**, (2015).
94. Zheng, Q. *et al.* Understanding Glass through Differential Scanning Calorimetry. *Chem. Rev.* **119**, 7848–7939 (2019).
95. Vogel & H. Das Temperaturabhängigkeitsgesetz der Viskosität von Flüssigkeiten. *Phys. Z.* **22**, 645–646 (1921).
96. Fulcher, G. S. Analysis of recent measurements of the Viscosity of Glasses. *J. Am. Ceram. Soc.* **8**, 789–794 (1925).
-

-
97. Tammann, G. & Hesse, W. Die Abhängigkeit der Viscosität von der Temperatur bei unterkühlten Flüssigkeiten. *Zeitschrift für Anorg. und Allg. Chemie* **156**, 245–257 (1926).
 98. Adam, G. & Gibbs, J. H. On the temperature dependence of cooperative relaxation properties in glass-forming liquids. *J. Chem. Phys.* **43**, 139–146 (1965).
 99. Avramov, I. & Milchev, A. Effect of disorder on diffusion and viscosity in condensed systems. *J. Non. Cryst. Solids* **104**, 253–260 (1988).
 100. Cohen, M. H. & Grest, G. S. Liquid-glass transition, a free-volume approach. *Phys. Rev. B* **20**, 1077–1098 (1979).
 101. Zheng, Q. & Mauro, J. C. Viscosity of glass-forming systems. *J. Am. Ceram. Soc.* **100**, 6–25 (2017).
 102. Stabile, P. *et al.* The effect of iron and alkali on the nanocrystal-free viscosity of volcanic melts: A combined Raman spectroscopy and DSC study. *Chem. Geol.* **559**, 119991 (2021).
 103. Rougier, J., Sparks, S. & Hill, L. J. *Risk and uncertainty assessment for natural hazards. Risk and Uncertainty Assessment for Natural Hazards* vol. 9781107006195 (Cambridge University Press, 2011).
 104. Newhall, C. G. & Punongbayan, R. S. The Narrow Margin of Successful Volcanic-Risk Mitigation. in *Monitoring and Mitigation of Volcano Hazards* 807–839 (Springer Berlin Heidelberg, 1996).
 105. Cassidy, M., Manga, M., Cashman, K. & Bachmann, O. Controls on explosive-effusive volcanic eruption styles. *Nat. Commun.* **9**, (2018).
 106. Dingwell, D. B. Volcanic dilemma: Flow or blow? *Science* vol. 273 1054 (1996).
 107. Kleest, C., Webb, S. L. & Fanara, S. Rheology of melts from the colli albani volcanic district (Italy): a case study. *Contrib. to Mineral. Petrol.* **175**, (2020).
 108. Blundy, J. D. & Cashman, K. Ascent-driven crystallisation of dacite magmas at Mount St Helens, 1980-1986. *Contrib. to Mineral. Petrol.* **140**, 631–650 (2001).
 109. Toramaru, A. Numerical study of nucleation and growth of bubbles in viscous magmas. *J. Geophys. Res.* **100**, 1913–1931 (1995).
 110. Gonnermann, H. M. & Manga, M. The Fluid Mechanics Inside a Volcano. *Annu. Rev. Fluid Mech.* **39**, 321–356 (2007).
-

-
111. Di Genova, D. *et al.* A compositional tipping point governing the mobilization and eruption style of rhyolitic magma. *Nature* **552**, 235–238 (2017).
 112. Whittington, A., Richet, P., Linard, Y. & Holtz, F. The viscosity of hydrous phonolites and trachytes. *Chem. Geol.* **174**, 209–223 (2001).
 113. Dingwell, D. B., Hess, K.-U. & Romano, C. Extremely fluid behavior of hydrous peralkaline rhyolites. *Earth Planet. Sci. Lett.* **158**, 31–38 (1998).
 114. Hess, K.-U., Dingwell, D. B. & Webb, S. L. The influence of alkaline-earth oxides (BeO, MgO, CaO, SrO, BaO) on the viscosity of a haplogranitic melt: systematics of non-Arrhenian behaviour. *Eur. J. Mineral.* **8**, 371–381 (1996).
 115. Hess, K.-U., Dingwell, D. B., Gennaro, C. & Mincione, V. Viscosity – temperature behaviour of dry melts in the Qz – Ab – Or system. *Chem. Geol.* **174**, 133–142 (2001).
 116. Robert, G., Smith, R. A. & Whittington, A. G. Viscosity of melts in the NaAlSiO₄-KAlSiO₄-SiO₂ system: Configurational entropy modelling. *J. Non. Cryst. Solids* **524**, (2019).
 117. Di Genova, D. *et al.* The rheology of peralkaline rhyolites from Pantelleria Island. *J. Volcanol. Geotherm. Res.* **249**, 201–216 (2013).
 118. Papale, P. Strain-induced magma fragmentation in explosive eruptions. *Nature* **397**, 425–428 (1999).
 119. Gonnermann, H. M. & Manga, M. The Fluid Mechanics Inside a Volcano. *Annu. Rev. Fluid Mech.* **39**, 321–356 (2007).
 120. de' Michieli Vitturi, M. & Aravena, Á. Chapter 6 - Numerical modeling of magma ascent dynamics. in *Forecasting and Planning for Volcanic Hazards, Risks, and Disasters* 239–284 (2021).
 121. Dingwell, D. B. & Virgo, D. Viscosities of melts in the Na₂O-FeO-Fe₂O₃-SiO₂ system and factors controlling relative viscosities of fully polymerized silicate melts. *Geochim. Cosmochim. Acta* **52**, 395–403 (1988).
 122. Mysen, B. O., Virgo, D. & Seifert, F. A. The structure of silicate melts: Implications for chemical and physical properties of natural magma. *Reviews of Geophysics* (1982).
 123. Chakraborty, S., Sivasubramanian, V., Singh, L. H., Krishnan, R. V. & Sinha, A. K. Anomalous variation of Boson peak and fragility and their correlations with

-
- intermediate-range structure in PbO-B₂O₃ glasses. *J. Alloys Compd.* **713**, 95–107 (2017).
124. Bockris, J. O. & Lowe, D. C. Viscosity and the structure of molten silicates. *Proc. R. Soc.* **226**, 423–435 (1954).
 125. McMillan, P. Structural studies of silicate glasses and melts-applications and limitations of Raman spectroscopy. *Am. Mineral.* **69**, 622–644 (1984).
 126. Ferraro, J. R., Nakamoto, K. & Brown, C. W. *Introductory Raman Spectroscopy*. Elsevier (2003). doi:10.1016/c2009-0-21238-4.
 127. Bertie, J. E. & Whalley, E. Optical spectra of orientationally disordered crystals. II. Infrared spectrum of ice Ih and ice Ic from 360 to 50 cm⁻¹. *J. Chem. Phys.* **46**, 1271–1284 (1967).
 128. Shuker, R. & Gammon, R. W. Raman-scattering selection-rule breaking and the density of states in amorphous materials. *Phys. Rev. Lett.* **25**, 222–225 (1970).
 129. Duval, E., Boukenter, A. & Achibat, T. Vibrational dynamics and the structure of glasses. *J. Phys. Condens. Matter* **2**, 10227–10234 (1990).
 130. Elliott, S. R. A unified model for the low-energy vibrational behaviour of amorphous solids. *Europhys. Lett.* **19**, 201–206 (1992).
 131. Mysen, B. O., Finger, L. W., Virgo, D. & Seifert, F. A. Curve-fitting of Raman spectra of silicate glasses. *Am. Mineral.* **67**, 686–695 (1982).
 132. Zotov, N., Yanev, Y., Epelbaum, M. & Konstantinov, L. Effect of water on the structure of rhyolite glasses - X-ray diffraction and Raman spectroscopy studies. *J. Non. Cryst. Solids* **142**, 234–246 (1992).
 133. Galeener, F. L. Band limits and the vibrational spectra of tetrahedral glasses. *Phys. Rev. B* **19**, 4292–4297 (1979).
 134. Hehlen, B. & Neuville, D. R. Raman response of network modifier cations in alumino-silicate glasses. *J. Phys. Chem. B* **119**, 4093–4098 (2015).
 135. Sen, P. N. & Thorpe, M. F. Phonons in AX₂ glasses: From molecular to band-like modes. *Phys. Rev. B* **15**, 4030–4038 (1977).
 136. McMillan, P. & Piriou, B. Raman spectroscopic studies of silicate and related glass structure: a review. *Bull. Mineral.* **106**, 57–75 (1983).
 137. Pasquarello, A., Sarnthein, J. & Car, R. Dynamic structure factor of vitreous silica from first principles: Comparison to neutron-inelastic-scattering
-

-
- experiments. *Phys. Rev. B - Condens. Matter Mater. Phys.* **57**, 14133–14140 (1998).
138. Sarnthein, J., Pasquarello, A. & Car, R. Origin of the high-frequency doublet in the vibrational spectrum of vitreous SiO₂. *Science* **275**, 1925–1927 (1997).
139. Le Losq, C., Neuville, D. R., Florian, P., Henderson, G. S. & Massiot, D. The role of Al³⁺ on rheology and structural changes in sodium silicate and aluminosilicate glasses and melts. *Geochim. Cosmochim. Acta* **126**, 495–517 (2014).
140. Le Losq, C. & Neuville, D. R. Effect of the Na/K mixing on the structure and the rheology of tectosilicate silica-rich melts. *Chem. Geol.* **346**, 57–71 (2013).
141. Wang, Z., Cooney, T. F. & Sharma, S. K. High temperature structural investigation of Na₂O·0.5Fe₂O₃·3SiO₂ and Na₂O·FeO·3SiO₂ melts and glasses. *Contrib. to Mineral. Petrol.* **115**, 112–122 (1993).
142. Hehlen, B. & Simon, G. The vibrations of vitreous silica observed in hyper-Raman scattering. *J. Raman Spectrosc.* **43**, 1941–1950 (2012).
143. Fontana, A. *et al.* The Raman coupling function in amorphous silica and the nature of the long-wavelength excitations in disordered systems. *Europhys. Lett.* **47**, 56–62 (1999).
144. Fontana, A. *et al.* The Raman coupling function in disordered solids: A light and neutron scattering study on glasses of different fragility. *J. Phys. Condens. Matter* **19**, 205145 (2007).
145. Surovtsev, N. V. & Sokolov, A. P. Frequency behavior of raman coupling coefficient in glasses. *Phys. Rev. B - Condens. Matter Mater. Phys.* **66**, 1–6 (2002).
146. Malinovsky, V. K., Novikov, V. N. & Sokolov, A. P. Log-normal spectrum of low-energy vibrational excitations in glasses. *Phys. Lett. A* **153**, 63–66 (1991).
147. Adar, F., Delhayé, M. & Da Silva, E. Evolution of instrumentation for detection of the Raman effect as driven by available technologies and by developing applications. in *Waters Symposium, Pittcon* (2003).
148. Lindsay, S. M., Anderson, M. W. & Sandercock, J. R. Construction and alignment of a high performance multipass vernier tandem Fabry–Perot interferometer. *Rev. Sci. Instrum.* **52**, 1478–1486 (1981).
-

-
149. Whitfield, C. H., Brody, E. M. & Bassett, W. Elastic moduli of NaCl by Brillouin scattering at high pressure in a diamond anvil cell. *Rev. Sci. Instrum.* **47**, 942–947 (1976).
 150. Speziale, S., Marquardt, H. & Duffy, T. S. Brillouin scattering and its application in geosciences. *Rev. Mineral. Geochemistry* **78**, 543–603 (2014).
 151. Di Genova, D. *et al.* Effect of iron and nanolites on Raman spectra of volcanic glasses: A reassessment of existing strategies to estimate the water content. *Chem. Geol.* **475**, 76–86 (2017).
 152. Di Genova, D. *et al.* Approximate chemical analysis of volcanic glasses using Raman spectroscopy. *J. Raman Spectrosc.* **46**, 1235–1244 (2015).
 153. Neuville, D. R., Courtial, P., Dingwell, D. B. & Richet, P. Thermodynamic and rheological properties of rhyolite and andesite melts. *Contrib. to Mineral. Petrol.* **113**, 572–581 (1993).
 154. Giordano, D. *et al.* An expanded non-Arrhenian model for silicate melt viscosity: A treatment for metaluminous, peraluminous and peralkaline liquids. *Chem. Geol.* **229**, 42–56 (2006).
 155. Misiti, V. *et al.* Viscosity of high-K basalt from the 5th April 2003 Stromboli paroxysmal explosion. *Chem. Geol.* **260**, 278–285 (2009).
 156. Al-Mukadam, R., Di Genova, D., Bornhöft, H. & Deubener, J. High rate calorimetry derived viscosity of oxide melts prone to crystallization. *J. Non. Cryst. Solids* **536**, (2020).
 157. Kirkpatrick, R. J. Kinetics of crystal growth in the system $\text{CaMgSi}_2\text{O}_6$ - $\text{CaAl}_2\text{SiO}_6$. *American Journal of Science* vol. 274 215–242 (1974).
 158. Licko, T. & Danek, V. Viscosity and structure of melts in the system CaO-MgO-SiO₂. *Phys. Chem. Glas.* **27**, 22–29 (1986).
 159. Sipp, A., Bottinga, Y. & Richet, P. New high viscosity data for 3D network liquids and new correlations between old parameters. *J. Non. Cryst. Solids* **288**, 166–174 (2001).
 160. Taniguchi, H. Entropy dependence of viscosity and the glass-transition temperature of melts in the system diopside-anorthite. *Contrib. to Mineral. Petrol.* **109**, 295–303 (1992).
 161. Urbain, G., Bottinga, Y. & Richet, P. Viscosity of liquid silica, silicates and

-
- alumino-silicates. *Geochim. Cosmochim. Acta* **46**, 1061–1072 (1982).
162. Taniguchi, H. Universal viscosity-equation for silicate melts over wide temperature and pressure ranges. *J. Volcanol. Geotherm. Res.* **66**, 1–8 (1995).
163. Bucaro, J. A. & Dardy, H. D. High-temperature strain relaxation in silica by optical correlation spectroscopy. *J. Non. Cryst. Solids* **24**, 121–129 (1977).
164. Napolitano, A. & Macedo, P. B. Spectrum of relaxation times in GeO₂ glass. *J. Res. Natl. Bur. Stand. Sect. A Phys. Chem.* **72A**, 425 (1968).
165. Sharma, S. K., Virgo, D. & Kushiro, I. Relationship between density, viscosity and structure of GeO₂ melts at low and high pressures. *J. Non. Cryst. Solids* **33**, 235–248 (1979).
166. Hushur, A., Manghnani, M. H., William S, Q. & Dingwell, D. B. A high-temperature Brillouin scattering study on four compositions of haplogranitic glasses and melts: High-frequency elastic behavior through the glass transition. *Am. Mineral.* **98**, 367–375 (2013).
167. Hess, K. U., Dingwell, D. B. & Webb, S. L. The influence of excess alkalis on the viscosity of a haplogranitic melt. *Am. Mineral.* **80**, 297–304 (1995).
168. Richet, P. & Polian, A. Water as a dense icelike component in silicate glasses. *Science* **281**, 396–398 (1998).
169. Whittington, A. G., Richet, P. & Polian, A. Amorphous materials: Properties, structure, and durability: Water and the compressibility of silicate glasses: A Brillouin spectroscopic study. *Am. Mineral.* **97**, 455–467 (2012).
170. Robert, G. *et al.* Heat capacity and viscosity of basaltic melts with H₂O ± F ± CO₂. *Chem. Geol.* **418**, 51–65 (2015).
171. Robert, G. The Effect of Volatiles on the Viscosity and Heat Capacity of Calc-Alkaline Basaltic and Basaltic Andesite Liquids. (University of Missouri, 2014).
172. Zheng, Q., Mauro, J. C., Ellison, A. J., Potuzak, M. & Yue, Y. Universality of the high-temperature viscosity limit of silicate liquids. *Phys. Rev. B - Condens. Matter Mater. Phys.* **83**, 13–15 (2011).
173. Zanatta, M. *et al.* Elastic properties of permanently densified silica: A Raman, Brillouin light, and x-ray scattering study. *Phys. Rev. B - Condens. Matter Mater. Phys.* **81**, 4–7 (2010).
174. Doremus, R. H. Viscosity of silica. *J. Appl. Phys.* **92**, 7619–7629 (2002).
-

-
175. Whittington, A. G., Richet, P. & Holtz, F. Water and the viscosity of depolymerized aluminosilicate melts. *Geochim. Cosmochim. Acta* **64**, 3725–3736 (2000).
 176. Corning Inc. Corning HPFS 7979, 7980, 8652, 8655 Fused Silica Optical Materials Product Information. 1–8 (2014).
 177. Di Genova, D., Zandona, A. & Deubener, J. Unravelling the effect of nano-heterogeneity on the viscosity of silicate melts: implications for glass manufacturing and volcanic eruptions. *J. Non. Cryst. Solids* **545**, 120248 (2020).
 178. Zandona, A., Patzig, C., Rüdinger, B., Hochrein, O. & Deubener, J. TiO₂(B) nanocrystals in Ti-doped lithium aluminosilicate glasses. *J. Non-Crystalline Solids X* **2**, 100025 (2019).
 179. Wang, Z., Kolesnikov, A. I., Ito, K., Podlesnyak, A. & Chen, S. H. Pressure Effect on the Boson Peak in Deeply Cooled Confined Water: Evidence of a Liquid-Liquid Transition. *Phys. Rev. Lett.* **115**, 3–8 (2015).
 180. Chuvaeva, T. I. *et al.* Low-frequency Raman scattering of magnesium aluminosilicate glasses and glass-ceramics. *J. Non. Cryst. Solids* **282**, 306–316 (2001).
 181. Bouhifd, M. A., Whittington, A. G., Roux, J. & Richet, P. Effect of water on the heat capacity of polymerized aluminosilicate glasses and melts. *Geochim. Cosmochim. Acta* **70**, 711–722 (2006).
 182. Giordano, D. *et al.* Heat capacity of hydrous trachybasalt from Mt Etna: comparison with CaAl₂Si₂O₈ (An)–CaMgSi₂O₆ (Di) as basaltic proxy compositions. *Contrib. to Mineral. Petrol.* **170**, 48 (2015).
 183. Martinez, L. M. & Angell, C. A. A thermodynamic connection to the fragility of glass-forming liquids. *Nature* **410**, 663–667 (2001).
 184. Mauro, J. C. & Loucks, R. J. Impact of fragility on enthalpy relaxation in glass. *Phys. Rev. E - Stat. Nonlinear, Soft Matter Phys.* **78**, 1–8 (2008).
 185. Robert, G., Whittington, A. G., Stechern, A. & Behrens, H. Heat capacity of hydrous basaltic glasses and liquids. *J. Non. Cryst. Solids* **390**, 19–30 (2014).
 186. Wang, L. M., Velikov, V. & Angell, C. A. Direct determination of kinetic fragility indices of glassforming liquids by differential scanning calorimetry: Kinetic versus thermodynamic fragilities. *J. Chem. Phys.* **117**, 10184–10192

-
- (2002).
187. Le Losq, C. *et al.* Percolation channels: A universal idea to describe the atomic structure and dynamics of glasses and melts. *Sci. Rep.* **7**, 16490 (2017).
 188. Neuville, D. R. Structure and properties in (Sr, Na) silicate glasses and melts. *Phys. Chem. Glas.* **46**, 112–118 (2005).
 189. Richet, N. F. Boson peak of alkali and alkaline earth silicate glasses: Influence of the nature and size of the network-modifying cation. *J. Chem. Phys.* (2012)
 190. Chemarin, C. & Champagnon, B. Medium range order in sodium silicate glasses: Role of the network modifier. *J. Non. Cryst. Solids* **243**, 281–284 (1999).
 191. Ando, M. F. *et al.* Boson peak, heterogeneity and intermediate-range order in binary SiO₂-Al₂O₃ glasses. *Sci. Rep.* **8**, 5394 (2018).
 192. Ando, M. F. *et al.* Boson peak and structural heterogeneity in ternary SiO₂-Al₂O₃-B₂O₃ glasses. *J. Am. Ceram. Soc.* 1–10 (2021).
 193. Orsingher, L. *et al.* Vibrational dynamics of permanently densified GeO₂ glasses: Densification-induced changes in the boson peak. *J. Chem. Phys.* **132**, 124508 (2010).
 194. Niss, K. *et al.* Influence of pressure on the boson peak: Stronger than elastic medium transformation. *Phys. Rev. Lett.* **99**, 3–6 (2007).
 195. Giordano, D., Russell, J. K. & Dingwell, D. B. Viscosity of magmatic liquids: A model. *Earth Planet. Sci. Lett.* **271**, 123–134 (2008).
 196. Gan, L., Xin, J. & Zhou, Y. Accurate viscosity calculation for melts in SiO₂-Al₂O₃-CaO-MgO systems. *ISIJ Int.* **57**, 1303–1312 (2017).
 197. Chen, C. *et al.* A novel viscosity-temperature model of glass-forming liquids by modifying the eyring viscosity equation. *Appl. Sci.* **10**, (2020).
 198. McIntosh, C., Toulouse, J. & Tick, P. The Boson peak in alkali silicate glasses. *J. Non. Cryst. Solids* **222**, 335–341 (1997).
 199. Mysen, B. O., Virgo, D. & Seifert, F. A. Redox equilibria of iron in alkaline earth silicate melts: relationships between melt structure, oxygen fugacity, temperature and properties of iron-bearing silicate liquids. *Am. Mineral.* **69**, 834–847 (1984).
 200. Jackson, W. E. *et al.* High-temperature XAS study of Fe₂SiO₄ liquid: Reduced coordination of ferrous iron. *Science* **262**, 229–233 (1993).
 201. Wilke, M. Fe in magma - An overview. *Ann. Geophys.* **48**, 609–617 (2005).
-

-
202. Borisov, A., Behrens, H. & Holtz, F. Effects of strong network modifiers on $\text{Fe}^{3+}/\text{Fe}^{2+}$ in silicate melts: an experimental study. *Contrib. to Mineral. Petrol.* **172**, 0 (2017).
 203. Farges, F. *et al.* The effect of redox state on the local structural environment of iron in silicate glasses: A combined XAFS spectroscopy, molecular dynamics, and bond valence study. *J. Non. Cryst. Solids* **344**, 176–188 (2004).
 204. Dingwell, D. B. & Virgo, D. The effect of oxidation state on the viscosity of melts in the system $\text{Na}_2\text{O}-\text{FeO}-\text{Fe}_2\text{O}_3-\text{SiO}_2$. *Geochim. Cosmochim. Acta* **51**, 195–205 (1987).
 205. Liebske, C., Behrens, H., Holtz, F. & Lange, R. A. The influence of pressure and composition on the viscosity of andesitic melts. *Geochim. Cosmochim. Acta* **67**, 473–485 (2003).
 206. Di Genova, D., Hess, K. U., Chevrel, M. O. & Dingwell, D. B. Models for the estimation of $\text{Fe}^{3+}/\text{Fe}_{\text{tot}}$ ratio in terrestrial and extraterrestrial alkali- and iron-rich silicate glasses using Raman spectroscopy. *Am. Mineral.* **101**, 943–952 (2016).
 207. Di Genova, D., Vasseur, J., Hess, K. U., Neuville, D. R. & Dingwell, D. B. Effect of oxygen fugacity on the glass transition, viscosity and structure of silica- and iron-rich magmatic melts. *J. Non. Cryst. Solids* **470**, 78–85 (2017).
 208. Kremers, S. *et al.* Shallow magma-mingling-driven Strombolian eruptions at Mt. Yasur volcano, Vanuatu. *Geophys. Res. Lett.* **39**, 1–6 (2012).
 209. Di Muro, A. *et al.* Micro-Raman determination of iron redox state in dry natural glasses: Application to peralkaline rhyolites and basalts. *Chem. Geol.* **259**, 78–88 (2009).
 210. Mercier, M. *et al.* Influence of glass polymerisation and oxidation on micro-Raman water analysis in aluminosilicate glasses. *Geochim. Cosmochim. Acta* **73**, 197–217 (2009).
 211. Giordano, D. & Russell, J. K. Towards a structural model for the viscosity of geological melts. *Earth Planet. Sci. Lett.* **501**, 202–212 (2018).
 212. Giordano, D. *et al.* A calibrated database of Raman spectra for natural silicate glasses: implications for modelling melt physical properties. *J. Raman Spectrosc.* (2019).
 213. Okuno, M., Zotov, N., Schmücker, M. & Schneider, H. Structure of $\text{SiO}_2-\text{Al}_2\text{O}_3$

-
- glasses: Combined X-ray diffraction, IR and Raman studies. *J. Non. Cryst. Solids* **351**, 1032–1038 (2005).
214. Mauro, J. C., Philip, C. S., Vaughn, D. J. & Pambianchi, M. S. Glass science in the United States: Current status and future directions. *Int. J. Appl. Glas. Sci.* **5**, 2–15 (2014).
215. Morse, D. L. & Evenson, J. W. Welcome to the Glass Age. *Int. J. Appl. Glas. Sci.* **7**, 409–412 (2016).
216. Dhé, P. Tipping crucible for basalt furnaces. *United States Patents Office* vol. US1462446A (1923).
217. Pisciotta, A., Perevozchikov, B. V., Osovetsky, B. M., Menshikova, E. A. & Kazymov, K. P. Quality Assessment of Melanocratic Basalt for Mineral Fiber Product, Southern Urals, Russia. *Nat. Resour. Res.* **24**, 329–337 (2015).
218. Gutnikov, S. I., Manylov, M. S. & Lazoryak, B. I. Crystallization and thermal stability of the p-doped basaltic glass fibers. *Minerals* **9**, 615 (2019).
219. Pareek, K. & Saha, P. Basalt Fiber and Its Composites : An Overview. *Proc. Natl. Conf. Adv. Struct. Technol.* 53–62 (2019).
220. de Lima, L. F., Zorzi, J. E. & Cruz, R. C. D. Basaltic glass-ceramic: A short review. *Bol. la Soc. Esp. Ceram. y Vidr.* 1–11 (2020)
doi:10.1016/j.bsecv.2020.07.005.
221. Liu, J. *et al.* Exploration of Basalt Glasses as High-Temperature Sensible Heat Storage Materials. *ACS Omega* **5**, 19236–19246 (2020).
222. Johannesson, B. *et al.* GREENBAS: Sustainable Fibres from Basalt Mining. *TemaNord* **1**, 2024 (2017).
223. Berry, A. J., O'Neill, H. S. C., Jayasuriya, K. D., Campbell, S. J. & Foran, G. J. XANES calibrations for the oxidation state of iron in a silicate glass. *Am. Mineral.* **88**, 967–977 (2003).
224. Magnien, V. *et al.* Kinetics of iron oxidation in silicate melts: A preliminary XANES study. *Chem. Geol.* **213**, 253–263 (2004).
225. Bonnin-Mosbah, M. *et al.* Micro X-ray absorption near edge structure at the sulfur and iron K-edges in natural silicate glasses. *Spectrochim. Acta - Part B At. Spectrosc.* **57**, 711–725 (2002).
226. McMillan, P. F. Raman spectroscopy in mineralogy and geochemistry. *Annu.*
-

-
- Rev. Earth Planet. Sci.* **17**, 255–279 (1989).
227. Malfait, W. J., Zakaznova-Herzog, V. P. & Halter, W. E. Quantitative Raman spectroscopy: Speciation of Na-silicate glasses and melts. *Am. Mineral.* **93**, 1505–1518 (2008).
228. Colomban, P., Tournie, A. & Bellot-Gurlet, L. Raman identification of glassy silicates used in ceramics, glass and jewellery: A tentative differentiation guide. *J. Raman Spectrosc.* **37**, 841–852 (2006).
229. Chen, T. *et al.* Synthesis and characterization of polycrystalline KAlSi₃O₈ hollandite [liebermannite]: Sound velocities vs. pressure to 13 GPa at room temperature. *Comptes Rendus - Geosci.* **351**, 113–120 (2019).
230. Best, M. G. *Igneous and Metamorphic Petrology*. (Blackwell Publishing Inc., 2003).
231. Giordano, D., Russell, J. K. & Dingwell, D. B. Viscosity of magmatic liquids: A model. *Earth Planet. Sci. Lett.* **271**, 123–134 (2008).
232. Quaranta, A. *et al.* Spectroscopic investigation of structural rearrangements in silver ion-exchanged silicate glasses. *J. Phys. Chem. C* **116**, 3757–3764 (2012).
233. Wang, Z., Cooney, T. F. & Sharma, S. K. In situ structural investigation of iron-containing silicate liquids and glasses. *Geochim. Cosmochim. Acta* **59**, 1571–1577 (1995).
234. Zotov, N., Ebbsjö, I., Timpel, D. & Keppeler, H. Calculation of Raman spectra and vibrational properties of silicate glasses: Comparison between Na₂Si₄O₉ and SiO₂ glasses. *Phys. Rev. B - Condens. Matter Mater. Phys.* **60**, 6383–6397 (1999).
235. Zanatta, M., Fontana, A., Rossi, F. & Gilioli, E. Effects of permanent densification on the vibrational density of states of vitreous silica. *J. Non. Cryst. Solids* **357**, 1892–1894 (2011).
236. Neuville, D. R. Viscosity, structure and mixing in (Ca, Na) silicate melts. *Chem. Geol.* **229**, 28–41 (2006).
237. Knoche, R., Dingwell, D. B., Seifert, F. A. & Webb, S. L. Non-linear properties of supercooled liquids in the system Na₂O-SiO₂. *Chem. Geol.* **116**, 1–16 (1994).
238. Nakamura, K., Takahashi, Y., Osada, M. & Fujiwara, T. Low-frequency Raman scattering in binary silicate glass: Boson peak frequency and its general

-
- expression. *J. Ceram. Soc. Japan* **121**, 1012–1014 (2013).
239. Furukawa, T., Fox, K. E. & White, W. B. Raman spectroscopic investigation of the structure of silicate glasses. III. Raman intensities and structural units in sodium silicate glasses. *J. Chem. Phys.* **75**, 3226–3237 (1981).
240. Brawer, S. A. & White, W. B. Raman spectroscopic investigation of the structure of silicate glasses. I. The binary alkali silicates. *J. Chem. Phys.* **63**, 2421–2432 (1975).
241. Hehlen, B., Neuville, D. R., Kilymis, D. & Ispas, S. Bimodal distribution of Si–O–Si angles in sodo-silicate glasses. *J. Non. Cryst. Solids* **469**, 39–44 (2017).
242. Maekawa, H., Maekawa, T., Kawamura, K. & Yokokawa, T. The structural groups of alkali silicate glasses determined from ²⁹Si MAS-NMR. *J. Non. Cryst. Solids* **127**, 53–64 (1991).
243. Le Losq, C. & Neuville, D. R. Molecular structure, configurational entropy and viscosity of silicate melts: Link through the Adam and Gibbs theory of viscous flow. *J. Non. Cryst. Solids* **463**, 175–188 (2017).
244. Poole, J. P. Low-Temperature Viscosity of Alkali Silicate Glasses. *J. Am. Ceram. Soc.* **32**, 230–233 (1949).
245. Vaills, Y., Luspain, Y. & Hauret, G. Two opposite effects of sodium on elastic constants of silicate binary glasses. *Mater. Sci. Eng. B* **40**, 199–202 (1996).
246. Greaves, G. N., Vaills, Y., Sen, S. & Winter, R. Density fluctuations, phase separation and microsegregation in silicate glasses. *J. Optoelectron. Adv. Mater.* **2**, 299–316 (2000).
247. Taylor, N. W. & Dear, P. S. Elastic and Viscous Properties of Several Soda-Silica Glasses in the Annealing Range of Temperature. *J. Am. Ceram. Soc.* **20**, 296–304 (1937).
248. Zhao, Q., Guerette, M. & Huang, L. Nanoindentation and Brillouin light scattering studies of elastic moduli of sodium silicate glasses. *J. Non. Cryst. Solids* **358**, 652–657 (2012).
249. Bauchy, M. Topological Constraint Theory and Rigidity of Glasses. *arXiv* 1–28 (2020) doi:10.1201/9780367333003-13.
250. Micoulaut, M. Constrained interactions, rigidity, adaptative networks, and their role for the description of silicates. *Am. Mineral.* **93**, 1732–1748 (2008).
-

-
251. Neuville, D. R. Viscosity, structure and mixing in (Ca, Na) silicate melts. *Chem. Geol.* **229**, 28–41 (2006).
 252. Weinberg, M. C. & Neilson, G. F. Phase separation behaviour of a metal-organic derived sodium silicate glass. *J. Mater. Sci.* **13**, 1206–1216 (1978).
 253. Chen, P. *et al.* Intermediate phase, network demixing, boson and floppy modes, and compositional trends in glass transition temperatures of binary As_xS_{1-x} system. *Phys. Rev. B - Condens. Matter Mater. Phys.* **78**, (2008).
 254. Bauchy, M. & Micoulaut, M. Atomic scale foundation of temperature-dependent bonding constraints in network glasses and liquids. in *Journal of Non-Crystalline Solids* (2011).
 255. Angell, C. A. Boson peaks and floppy modes: Some relations between constraint and excitation phenomenology, and interpretation, of glasses and the glass transition. *J. Phys. Condens. Matter* **16**, (2004).
 256. Naumis, G. G. Low-frequency vibrational modes anomalies and rigidity: A key to understanding the glass and the electronic properties of flexible materials from a topological perspective. *Front. Mater.* **2**, 1–9 (2015).